

Seismic-interferometric applications for near-surface and mineral exploration

Balestrini, F.I.

DOI

[10.4233/uuid:bf83b94a-4438-47c7-bfca-7a93334d79e4](https://doi.org/10.4233/uuid:bf83b94a-4438-47c7-bfca-7a93334d79e4)

Publication date

2023

Document Version

Final published version

Citation (APA)

Balestrini, F. I. (2023). *Seismic-interferometric applications for near-surface and mineral exploration*. [Dissertation (TU Delft), Delft University of Technology]. <https://doi.org/10.4233/uuid:bf83b94a-4438-47c7-bfca-7a93334d79e4>

Important note

To cite this publication, please use the final published version (if applicable). Please check the document version above.

Copyright

Other than for strictly personal use, it is not permitted to download, forward or distribute the text or part of it, without the consent of the author(s) and/or copyright holder(s), unless the work is under an open content license such as Creative Commons.

Takedown policy

Please contact us and provide details if you believe this document breaches copyrights. We will remove access to the work immediately and investigate your claim.

**SEISMIC-INTERFEROMETRIC APPLICATIONS FOR
NEAR-SURFACE AND MINERAL EXPLORATION**

SEISMIC-INTERFEROMETRIC APPLICATIONS FOR NEAR-SURFACE AND MINERAL EXPLORATION

Dissertation

for the purpose of obtaining the degree of doctor
at Delft University of Technology,
by the authority of the Rector Magnificus, Prof. dr. ir. T.H.J.J. van der Hagen,
chair of the Board of Doctorates,
to be defended publicly on Tuesday, 14 March 2023 at 15:00 o'clock

by

Florencia Ibel BALESTRINI

Master of Science in Geophysics,
National University of La Plata, Buenos Aires, Argentina
born in Florencio Varela, Argentina.

This dissertation has been approved by

promotor: Dr. ir. D.S. Draganov

promotor: Dr. R. Ghose

Composition of the doctoral committee:

Rector Magnificus,
Dr. ir. D.S. Draganov,
Dr. R. Ghose,

Chairman
Delft University of Technology
Delft University of Technology

Independent members:

Prof. dr. ir. V. Socco,
Prof. dr. ir. E.C. Slob,
Dr. ir. D.J. Verschuur,
Dr. M.W.N. Buxton,

Politecnico di Torino, Italy
Delft University of Technology
Delft University of Technology
Delft University of Technology

Other members:

Dr. ir. D.J.M. Ngan-Tillard,

Delft University of Technology

Reserve members:

Prof. dr. ir. C.P.A. Wapenaar,

Delft University of Technology

This study was carried out within the Smart Exploration project. Smart Exploration has received funding from the European Union's Horizon 2020 research and innovation programme under grant agreement number 775971.



SMARTEXPLORATION
new ways to explore the subsurface

Keywords: Seismic interferometry, seismic data processing, data reconstruction

Printed by: Gildeprint

Copyright © 2023 by E.I. Balestrini

ISBN 978-94-6366-671-8

An electronic version of this dissertation is available at

<http://repository.tudelft.nl/>.

*A Humberto,
Pedro y Lili*

CONTENTS

| | |
|---|-------------|
| Summary | ix |
| Samenvatting | xiii |
| 1 Introduction | 1 |
| 1.1 Thesis objectives | 3 |
| 1.2 Seismic interferometry | 3 |
| 1.3 Outline | 6 |
| References | 8 |
| 2 Improved target illumination at Ludvika mines of Sweden through seismic-interferometric surface-wave suppression | 11 |
| 2.1 Introduction | 12 |
| 2.2 Blötberget iron-oxide deposit | 14 |
| 2.3 Seismic data acquisition | 14 |
| 2.4 Seismic interferometry with active sources for surface-wave retrieval | 15 |
| 2.5 Adaptive subtraction | 17 |
| 2.6 Results | 17 |
| 2.7 Conclusions | 24 |
| 2.8 Acknowledgements | 26 |
| References | 26 |
| 3 Surface-wave suppression through seismic interferometry: a case study at the Siilinjärvi phosphate mine in Finland | 29 |
| 3.1 Introduction | 30 |
| 3.2 Siilinjärvi phosphate mine | 31 |
| 3.3 Adaptive subtraction of surface waves through seismic interferometry | 32 |
| 3.4 Data acquisition and processing | 33 |
| 3.5 Results | 35 |
| 3.6 Conclusions | 42 |
| 3.7 Acknowledgements | 43 |
| References | 44 |
| 4 Electromagnetic-interferometric direct-wave suppression for detection of shallow buried targets with GPR | 47 |
| 4.1 Introduction | 48 |
| 4.2 Electromagnetic interferometry and adaptive subtraction | 49 |
| 4.3 Data acquisition and processing | 51 |
| 4.4 Results | 52 |

| | | |
|----------|--|------------|
| 4.5 | Conclusions. | 58 |
| 4.6 | Acknowledgments | 59 |
| | References | 59 |
| 5 | Data reconstruction using seismic interferometry applied to active-source data from the Ludvika Mines of Sweden | 63 |
| 5.1 | Introduction | 64 |
| 5.2 | Methodology | 64 |
| 5.3 | Simple 2D numerically modelled data example | 65 |
| 5.4 | Blötberget iron-oxide deposit data | 69 |
| 5.5 | Conclusions. | 74 |
| 5.6 | Acknowledgements | 75 |
| | References | 75 |
| 6 | Interferometric data reconstruction inside relatively large gaps utilising hyperbolic Radon transforms | 77 |
| 6.1 | Introduction | 78 |
| 6.2 | Methodology | 80 |
| | 6.2.1 Seismic interferometry. | 80 |
| | 6.2.2 Hyperbolic Radon transform. | 80 |
| | 6.2.3 Merging of active- and virtual-source data. | 82 |
| 6.3 | Numerically modelled data example | 82 |
| 6.4 | Field data example | 88 |
| 6.5 | Conclusions. | 99 |
| | References | 100 |
| 7 | Conclusions and recommendations | 105 |
| 7.1 | Conclusions. | 105 |
| 7.2 | Recommendations | 108 |
| | References | 109 |
| | Acknowledgements | 111 |
| | Curriculum Vitæ | 113 |
| | List of Publications | 115 |

SUMMARY

Seismic methods are widely used for the exploration of the Earth's subsurface. While they allow higher resolution compared to other geophysical methods, their performance depends on site and geological characteristics, and the volume and type of recorded information. Additionally, data processing plays a critical role in the efficacy of the application of seismic methods.

A common challenge when utilising seismic methods arises as a result of field restrictions and cost constraints. As a consequence, seismic data often suffer from irregular or sparse spatial sampling, which can affect the application of advanced processing and imaging algorithms, for instance, surface-related multiple elimination and wave-equation migration. These algorithms require dense and regular sampling to provide reliable results. Thus, seismic-data regularisation and interpolation are commonly utilised processing steps. Nevertheless, the interpolation of data for relatively large gaps is not trivial, in particular for land data acquired in complex geological settings where the seismic events exhibit pronounced curvature and lack of continuity.

In addition, seismic data acquired in land contain surface waves. Surface waves constitute a strong source of noise that decreases the signal-to-noise ratio and overall quality of the reflection data, and can obscure events of interest. The performance of the subsequent processing steps can also be affected when surface waves are not properly suppressed. However, surface waves can be arduous to remove with conventional processing methods (e.g., frequency-wavenumber or bandpass filters) since they can occupy the same regions in the frequency domain and have similar moveout velocities as the reflected waves that we wish to preserve. These filters can also strongly influence the frequency content, resulting in amplitude distortions and the appearance of artefacts in the data.

Usually referred to as seismic interferometry (SI), the cross-correlation of seismic observations at different receiver locations, and possible consecutive summation over the available sources, allows the retrieval of new seismic responses from virtual sources located at the position of the receivers. In addition to providing extra information that can help the interpretation of the data, the SI responses can be utilised for different processing steps.

The interferometric surface-wave suppression method consists of retrieving surface-wave estimates between two receivers by cross-correlating the recorded traces at these receivers and then stacking them over multiple active sources. For a line survey, sources at points in-line with the receivers contribute to the retrieval of direct body- or surface-wave arrivals since they all fall in the so-called stationary-phase region. Because all in-line sources would contribute to the retrieval of surface waves, while only a few contribute to the retrieval of reflections, the result retrieved by SI will be dominated by surface waves. Subsequently, these retrieved responses are subtracted from the field recordings, obtaining data with suppressed surface waves.

In this study, we show the efficacy of the interferometric surface-wave suppression method in hard-rock, near-mine environments. We apply this technique to seismic reflection data acquired for imaging the iron-oxide mineralisation in the Ludvika mining area, in central Sweden. After applying SI, we retrieve dominant surface waves that represent the surface waves in the field data. Following, the retrieved surface waves are adaptively subtracted from the data, and several reflections from the mineralisation zone are enhanced and better visualised. These results illustrate how new methods for seismic processing can successfully be utilised in such a highly noisy environment. Next, to further consolidate the application of SI surface-wave suppression for these types of data, we apply the methodology to an active-source reflection seismic dataset acquired at the Siilinjärvi mines, eastern Finland. We find that after this step, a successful surface-wave suppression is obtained which helps improve the imaging. Our results show clearer reflections, sharper boundaries of the mineralisation with the surrounding rocks and, overall, an enhanced final image of the subsurface.

In order to extend the application of the interferometric wave-suppression method to electromagnetic wavefields and near-surface data, we apply electromagnetic interferometry for suppression of the direct-wave arrival to data acquired with ground-penetrating radar in the Jewish Cemetery in Naaldwijk, The Netherlands. The objective of the survey is to identify locations of possible old, buried tombstones. Such tombstones are expected not deeper than a few tens of centimetres. Thus, the earlier times of the data are of great importance for the detection of events that could indicate possible locations of buried tombstones. However, the direct wave propagating along the surface can completely cover the shallowest targets. After applying electromagnetic interferometry, we obtain a direct-wave estimate that we subsequently adaptively subtract from the field data. This allows us to obtain cleaner time sections for the earliest times and unveil diffraction events that were covered by the direct arrival, permitting the identification of the shallowest anomalies in the subsurface.

Next, to address the seismic-processing challenges related to the lack of densely sampled data, we propose to utilise SI to retrieve new reflection events in order to provide the missing traces in data with relatively large gaps. The retrieved SI responses also contain spurious events, such as virtual refractions and non-physical reflections. Additionally, the presence of a gap and other noises in the data adds extra artefacts to the SI result. In order to suppress these noises and spurious events, and combine both the original data with the gap and the SI data in a more suitable way, we evaluate the implementation of different algorithms. These algorithms are then applied to data acquired for hard-rock mineral exploration and near-surface applications.

Firstly, we utilise a projection-onto-convex-set image-restoration algorithm for data reconstruction. This is a simple iterative method that consists of a) the 2D Fourier transformation of the data, the application of a threshold to the transformed data leaving only the highest amplitudes, b) an inverse 2D Fourier transformation of the results of the data with the threshold applied, and c) the reinsertion of the values of the original samples that do not need to be interpolated. The threshold value is then varied from a large value during the first iteration to a small value during the last iteration. We observe that the projection-onto-convex-set method on its own fails to properly reconstruct events when the data presents a relatively large gap. However, the algorithm performs better when we

incorporate virtual-source data to supply the missing traces.

Secondly, we present a simple and practical methodology that utilises the hyperbolic Radon transform to suppress the spurious events present in the SI responses. The hyperbolic Radon transform has the ability to focus and separate hyperbolic events with different curvatures (i.e., reflection events with different velocities) and is commonly used for processing and interpolation. We transform the active-source data with a large gap and virtual-source data to the Radon domain. Subsequently, we utilise the active-source data to create a mask to filter the SI responses in the Radon domain. This helps suppress artefacts and spurious events to obtain a more suitable result for merging. Then, we transform the virtual-source data back to the time-offset domain and combine this filtered result with the active-source data. We tested this method utilising near-surface field data acquired in the western part of the Netherlands. Our results show that this method allows obtaining an enhanced image of the subsurface when compared to the results from the data with the large gaps.

The methodologies illustrated and developed in this work have successfully shown that the utilization of SI helps achieve enhanced seismic imaging results. The responses retrieved by SI provide thus additional information that can also be utilised as a tool for seismic processing.

SAMENVATTING

Seismische methoden worden veel gebruikt om de ondergrond van de aarde te verkennen. Hoewel ze hogere resoluties bereiken in vergelijking met andere geofysische methoden, zijn hun resultaten erg afhankelijk van locatie specifieke en geologische kenmerken, en ook van het volume en type van de opgenomen informatie. Bovendien wordt de werkzaamheid van toegepaste seismische methoden grotendeels bepaald door de verwerking van de data.

Een veelvoorkomende uitdaging in het gebruik van seismische methoden komt voort uit praktische veld restricties en kosten beperkingen. Ten gevolge hiervan hebben seismische methoden vaak last van irreguliere of verspreide ruimtelijke meetpunten, dit kan effect hebben de applicatie van geavanceerde bewerkings- en beeldalgoritmes, bijvoorbeeld eliminatie van meervoudige, oppervlakte-gerelateerde reflecties en golfvergelijking migraties. Deze algoritmes hebben een dichte en reguliere spreiding van metingen nodig om fatsoenlijke resultaten te bereiken. Hierom zijn regularisatie en interpolatie veelgebruikte bewerking stappen voor seismische data. De interpolatie van data voor relatieve grote gaten is echter niet triviaal, in het bijzonder voor land data die verkregen zijn boven complexe geologische structuren, waar de seismische golfvelden uitgesproken krommingen en gebrek aan continuïteit tonen.

Daarbovenop bevat seismische data, verkregen op land, oppervlaktegolven. Oppervlaktegolven vormen een sterke bron van ruis, wat de signaal-ruis verhouding en algehele kwaliteit van de reflectie data verlaagt, en kunnen andere belangrijke kenmerken verhullen. De prestaties van de vervolg stappen voor de data verwerking kunnen ook beïnvloed worden als oppervlaktegolven niet naar behoren onderdrukt zijn. Oppervlaktegolven zijn echter moeilijk te verwijderen met conventionele bewerkingsmethoden (bijv. frequentie-golfgetal of band filters), omdat ze zich in dezelfde delen van het frequentie domein kunnen bevinden en vergelijkbare uitloop snelheden hebben als de, te behouden, gereflecteerde golven. Deze filters kunnen ook de frequentie inhoud sterk beïnvloeden, wat resulteert in amplitude vervormingen en het verschijnen van artefacten in de data.

Meestal aangeduid als seismische interferometrie (SI), de kruis-correlatie van seismische observaties op verschillende ontvanger locaties en mogelijk de opvolgende som over de beschikbare bronnen, maakt het mogelijk om nieuwe seismische waarnemingen van virtuele bronnen op de plek van de ontvangers te creëren. Naast het verstrekken van extra informatie die kan helpen met de interpretatie van de data, kunnen de SI waarnemingen ook gebruikt worden voor verschillende bewerkingsstappen. De interferometrische oppervlaktegolf onderdrukkingsmethode bestaat uit het verkrijgen van oppervlaktegolf schattingen tussen twee ontvangers door de opgenomen meting van deze ontvangers te kruis-correleren en ze dan op te tellen over meerdere actieve bronnen. Voor een lijn meting, bronnen op punten parallel aan de ontvangers dragen bij aan het herwinnen van directe ruimte- of oppervlakte-golf aankomsten, doordat ze in de zogeheten stationaire-fase regio vallen. Omdat alle parallellen bronnen zouden bijdragen

aan de winning van oppervlaktegolven, terwijl slechts enkele bijdragen aan de winning van reflecties, zal het resultaat dat door SI wordt behaald gedomineerd worden door oppervlaktegolven. Vervolgens, worden deze behaalde resultaten van de veld opnamen afgetrokken en wordt data met onderdrukte oppervlaktegolven verkregen.

In dit onderzoek, tonen we de doeltreffendheid van de interferometrische oppervlaktegolf onderdrukkingmethode in harde rots ondergronden dichtbij mijnen. We passen deze techniek toe op seismische reflectie data verkregen voor het in kaart brengen van ijzeroxide mineralisatie onder het Ludvika mijngebied in centraal Zweden. Na het toepassen van SI, leiden we de dominante oppervlaktegolven af die de oppervlaktegolven in de velddata vertegenwoordigen. Vervolgens worden deze oppervlaktegolven adaptief afgetrokken van de data, en verschillende reflecties van de mineralisatie zone zijn versterkt en beter gevisualiseerd. Deze resultaten laten zien hoe nieuwe methoden voor seismische bewerking succesvol gebruikt kunnen worden in een omgeving met veel ruis. Om de toepassing van de SI oppervlaktegolf onderdrukking voor dit type data te onderstrepen, wordt de methode nu toegepast op een actieve-bron reflectie dataset verkregen bij de Siilinjärvi mijnen in oost Finland. We bevinden dat na deze stap, een succesvolle oppervlaktegolf onderdrukking is verkregen, welke helpt met het in kaart brengen van de ondergrond. Onze resultaten tonen schonere reflecties, scherpere grenzen van de mineralisatie met de omringende stenen en een beter beeld van de ondergrond in het algemeen.

Om de toepassing van de interferometrische oppervlaktegolf onderdrukkingmethode uit te breiden tot elektromagnetische golfvelden en dicht-aan-de-oppervlakte data, passen we elektromagnetische interferometrie voor onderdrukking van de directeveld aankomst toe op data verkregen met bodemradar (GPR) in de Joodse begraafplaats te Naaldwijk, Nederland. Het doel van het onderzoek is het identificeren van mogelijke locaties van oude, begraven grafstenen. Zulke grafstenen zijn niet dieper dan een paar tienden centimeters verwacht. Daarom zijn de eerdere tijden van de data van groot belang voor de detectie van signalen die de mogelijke locaties van de grafstenen kunnen aangeven. De directe golf, die langs de oppervlakte propageert, kan de ondiepe doelwitten echter compleet bedekken. Na het toepassen van elektromagnetische interferometrie, verkrijgen we een directe golf schatting, die we vervolgens adaptief af kunnen trekken van de velddata. Dit stelt ons in staat om schonere tijdsecties voor de eerste tijden te verkrijgen en om diffracties, die beschut waren door de directe aankomst, te onthullen, dit laat de identificatie toe van de ondiepste afwijkingen in de ondergrond.

Vervolgens, om de seismische bewerkingssuitdaging gerelateerd aan gebrek van dichte metingen te adresseren, stellen we SI voor om nieuwe reflecties te winnen om missende datapunten te herstellen in data met relatief grote gaten. De verkregen SI metingen bevatten ook onechte signalen, zoals virtuele refracties en niet fysische reflecties. Bovendien, de aanwezigheid van een gat en andere ruis in de data voegt meer artefacten toe aan het SI resultaat. Om deze ruis en onechte signalen te onderdrukken en zowel de originele data met het gat en de SI data te combineren op een meer toepasselijke manier, evalueren we de implementatie van verschillende algoritmes. Deze algoritmes zijn dan toegepast op data verkregen voor hard-gesteente mineraal exploratie en toepassingen vlakbij het oppervlakte.

Ten eerste, gebruiken we een projectie-op-convexe-set beeld-herstel algoritme voor

data reconstructie. Dit is een simpele, iteratieve methode, die bestaat uit a) 2D Fourier transformatie van de data, de toepassing van een drempelwaarde op de getransformeerde data, waarna alleen de hoogste amplitudes overblijven, b) een inverse 2D Fourier transformatie van de resultaten van de data met de toegepaste drempelwaarde en c) het herstellen van de originele data die niet geïnterpoleerd hoefde te worden. De drempelwaarde wordt dan gevarieerd van een hoge waarde in de eerste iteratie naar een lage waarde in de laatste iteratie. We zien dat de projectie-op-convexe-set method op zichzelf faalt om de signalen naar behoren te reconstrueren, wanneer er een relatief groot gat in de data zit. Het algoritme presteert echter beter wanneer we de virtuele bron data inbrengen om de missende datapunten te verschaffen.

Ten tweede, presenteren we een simpele en praktische methode, die de hyperbolische Radon transformatie gebruikt om het onechte signaal in de SI data te onderdrukken. De hyperbolische Radon transformatie heeft de mogelijkheid om te focussen en om hyperbolisch signaal met verschillende krommingen te scheiden (zoals reflectie signaal met verschillende snelheden) en wordt veelal gebruikt voor verwerking en interpolatie. We transformeren de actieve-bron data met een groot gat en virtuele bron data naar het Radon domein. Vervolgens, gebruiken de actieve-bron data om een masker te creëren om het SI signaal te filteren in het Radon domein. Dit helpt met het onderdrukken van artefacten en onechte signalen om een meer geschikt resultaat te verkrijgen voor het samenvoegen van de data. Daarna transformeren we de virtuele-bron data terug naar het tijd-afstand domein en combineren we dit gefilterde resultaat met de actieve-bron data. We testten deze methode op data dichtbij de oppervlakte verkregen in het westen van Nederland. Onze resultaten laten zien dat deze methode een beter beeld van de ondergrond verkrijgt vergeleken met de resultaten van de data met het grote gat.

De methodologieën die in dit werk zijn geïllustreerd en ontwikkeld hebben met succes aangetoond dat het gebruik van SI helpt met het verkrijgen van betere seismische beelden. De resultaten verkregen met SI verstrekken dus aanvullende informatie die ook gebruikt kan worden als een hulpmiddel voor seismische bewerking.

1

INTRODUCTION

Seismic methods have been used for exploration and characterisation of the Earth's subsurface and its resources at least since the beginning of the 20th century [1, 2]. The use of seismic methods has its origin in the exploration for oil and gas [1, 2]. Nevertheless, they are also widely used in near-surface applications, for instance, for geotechnical and civil engineering [1]. In the past years, the utilisation of seismic methods for the exploration of minerals beyond fossil fuels has also increased considerably. This is due to the ability of the seismic methods to gather data with higher resolution, and to achieve greater penetration at depth, making them convenient for imaging deeper mining targets [3–5]. However, the data acquired in mining environments will often suffer from low signal-to-noise ratio and exhibit strong heterogeneities, including faults and fractures at different scales.

The performance of the seismic methods strongly depends on site and geologic characteristics [3, 6]. One of the main challenges comprises the processing of seismic data, especially in complex and noisy mining areas [3]. Careful processing is needed in order to improve the signal-to-noise ratio and obtain higher-resolution images of the subsurface. This can allow, for instance, the accurate delineation of the ore deposits at depth. However, advanced seismic processing algorithms require dense and regularly sampled data to produce optimal imaging results [7, 8]. Conversely, seismic data occasionally suffers from irregular or sparse spatial sampling, for example, as a result of cost constraints or field-acquisition restrictions, which is often observed in near-surface and hard-rock mineral exploration. Thus, different algorithms for the reconstruction of seismic data have been proposed and are commonly utilised for seismic processing.

These algorithms for data reconstruction include, for instance, prediction-error-filter-based methods [9–11], wave-equation-based methods [12, 13], and transform-based methods. The latter make use of transformations in order to exploit the properties of the data in an auxiliary domain, such as Fourier [14, 15], curvelet [16–18], and Radon domains [19, 20]. Some disadvantages of these methods are that they often require knowledge of the velocity in the subsurface. Additionally, although effective for interpolation of regularly sampled sparse data or randomly missing traces, they tend to fail and produce poor results in cases when there are relatively large gaps, in particular in complex geological settings where the seismic events exhibit pronounced curvature and lack of continuity.

In such cases, seismic interferometry (SI) could be utilised for data reconstruction.

SI refers to the principle of retrieving new seismic responses from virtual sources at the position of receivers. For controlled- or active-source data, it is most commonly applied by cross-correlating seismic observations at different receiver locations, and then stacking over the available sources [21, 22]. Hence, seismic responses between two receivers could be retrieved by cross-correlating recorded traces at these receivers. Several studies have used SI for estimating missing traces and to partially mitigate artefacts present in these estimates [23–27]. These methods are mostly developed and utilised for marine-data applications to supply the near-offset missing traces. However, when applied to land data, reflections present in the active-source data become harder to retrieve through SI due to stronger wave attenuation and lower signal-to-noise ratio. Moreover, land seismic data contain surface waves, which constitute a strong source of noise in reflection seismic [22, 28, 29]. Surface waves can obscure the reflected waves, which are the waves of interest. Furthermore, the responses retrieved by SI contain additional undesired events from the direct and surface waves. That is why, to be able to apply novel and advanced processing methodologies, surface waves need to be properly suppressed. However, this noise can be difficult and laborious to remove, particularly when the surface waves are scattered due to a complex geological setting and near-surface heterogeneities [22, 30].

Conventionally, surface waves are suppressed during data processing using frequency-offset (f - x) or frequency-wavenumber (f - k) filters [31]. However, these methods can be ineffective when the surface waves are scattered and occupy the same regions in the f - x or f - k domains as the reflected body waves that we wish to preserve [22, 28, 30]. The use of f - k filters could also lead to the appearance of artefacts, which affect the quality of the seismic images. Other methods that focus on the removal of surface waves are based on prediction-removal suppression schemes [32], which estimate and then subtract surface waves using, for instance, a modelling-based inversion.

More recently, the utilisation of SI for surface-wave suppression has been developed and presented by a number of authors in the context of hydrocarbon exploration [22, 28, 30] and for near-surface applications [33, 34]. Surface waves between two receivers can be retrieved by cross-correlating or cross-convolving recorded traces at these receivers [35]. These retrieved responses could then be used for surface-wave suppression. The interferometric surface-wave suppression method thus predicts the surface waves in shot gathers and subsequently suppresses the surface waves through the use of least-square matching filters. However, the number of applications of this technique to noisy field seismic data is rather limited, and so far, there are no reported applications in hard-rock mining environments.

In the next section, we describe the objectives of this thesis, which address the seismic-processing challenges previously reported. Following, we provide a brief explanation of SI by cross-correlation for the retrieval of new seismic responses. This will serve as a theoretical base of SI and will be referred to throughout the subsequent chapters. It will also serve as the base for the latter introduction of electromagnetic interferometry. Finally, this chapter is concluded with a description of the outline of this thesis.

1.1. THESIS OBJECTIVES

In order to assess the aforementioned seismic-processing challenges, one of the goals of this thesis is to illustrate the processing scheme for SI surface-wave suppression when applied to hard-rock near-mine environments. Applying SI, estimates of surface waves are obtained. Subsequently, these estimated surface waves are adaptively subtracted from the original shot gathers. This allows obtaining cleaner datasets, in a purely data-driven way, that provide better results after seismic processing and imaging.

After a successful suppression of the surface waves, other processing steps to improve the quality of the final image could be undertaken, for example, filling-in of missing traces. The second goal of this thesis is to show the retrieval of SI responses in order to provide missing traces, focusing on hard-rock and near-surface applications, specifically for cases when there are relatively large spatial gaps in the acquired data. These scenarios pose extra challenges since the SI responses contain spurious events and noises. The latter are more pronounced due to the presence of large gaps and other noises in the data.

In near-surface investigations of the shallowest structures, the utilisation of ground penetrating radar (GPR) is very popular. An analogue of the surface-wave noise in GPR surveys are the direct air and ground waves. Thus, as another goal of this thesis, we also extend the concept of interferometric suppression of surface waves to suppression of electromagnetic direct waves in GPR recordings.

This thesis strives to further consolidate the application of SI for the processing of seismic data. Additionally, it illustrates the potential of seismic methods and novel processing methodologies in the exploration of the deeper mining targets and the near-surface region. This study contributes to the development of cost-effective and environmentally friendly tools and methods for geophysical exploration since, by utilising SI, the processing is carried out in an entirely data-driven manner, without the use of any a priori velocity model or previous knowledge of the subsurface.

1.2. SEISMIC INTERFEROMETRY

When seismic methods are utilised for exploration, an energy source (controlled or active source) is excited, generating seismic waves. These seismic waves propagate through the Earth and along its surface. When they encounter a boundary between two interfaces with different elastic properties, a part of the seismic-wave energy is reflected or scattered, and another part is transmitted further (in case of a scatterer). The returning waves (in case of propagation along the surface) from the underground are then recorded by geophones located, for instance, at the surface. These seismic recordings contain information of the reflectivity of the Earth and are used to obtain reflection seismic images of the actual geological structures.

The cross-correlation of the seismic responses recorded at two different receiver locations can retrieve the Green's function between these two receivers. The Green's function describes the propagation path from a point source location to a receiver location. Therefore, the retrieval of new seismic responses by cross-correlation of the data is often called Green's function retrieval by cross-correlation, also known as SI.

The basis for SI by cross-correlation is derived from the reciprocity equation of cor-

relation type and from source-receiver reciprocity, and is given in the frequency domain by [21, 36]

$$A, B \in \mathbb{D}; \hat{G}(\mathbf{x}_B, \mathbf{x}_A, \omega) + \hat{G}^*(\mathbf{x}_B, \mathbf{x}_A, \omega) = \oint_{\partial\mathbb{D}} \frac{-1}{j\omega\rho(\mathbf{x})} \left[\hat{G}(\mathbf{x}_B, \mathbf{x}, \omega) \partial_i \hat{G}^*(\mathbf{x}_A, \mathbf{x}, \omega) - \hat{G}^*(\mathbf{x}_A, \mathbf{x}, \omega) \partial_i \hat{G}(\mathbf{x}_B, \mathbf{x}, \omega) \right] n_i d^2\mathbf{x}, \quad (1.1)$$

or

$$A, B \in \mathbb{D}; 2\Re[\hat{G}(\mathbf{x}_B, \mathbf{x}_A, \omega)] = \oint_{\partial\mathbb{D}} \frac{-1}{j\omega\rho(\mathbf{x})} \left[\hat{G}(\mathbf{x}_B, \mathbf{x}, \omega) \partial_i \hat{G}^*(\mathbf{x}_A, \mathbf{x}, \omega) - \hat{G}^*(\mathbf{x}_A, \mathbf{x}, \omega) \partial_i \hat{G}(\mathbf{x}_B, \mathbf{x}, \omega) \right] n_i d^2\mathbf{x}, \quad (1.2)$$

since

$$2\Re[\hat{G}(\mathbf{x}_B, \mathbf{x}_A, \omega)] = \hat{G}(\mathbf{x}_B, \mathbf{x}_A, \omega) + \hat{G}^*(\mathbf{x}_B, \mathbf{x}_A, \omega). \quad (1.3)$$

The hat ($\hat{\cdot}$) stands for frequency domain, and ω is the angular frequency. $\hat{G}(\mathbf{x}_A, \mathbf{x}, \omega)$ is the Fourier transform of the Green's function, which represents an impulse response observed at \mathbf{x}_A due to a source excited at \mathbf{x} , and respectively for $\hat{G}(\mathbf{x}_B, \mathbf{x}, \omega)$, with both \mathbf{x}_A and \mathbf{x}_B inside an arbitrary volume \mathbb{D} . $\partial\mathbb{D} = \partial\mathbb{D}_0 + \partial\mathbb{D}_1$ is the boundary enclosing the volume \mathbb{D} (Figure 1.1). $\partial_i \hat{G}^*(\mathbf{x}_A, \mathbf{x}, \omega) n_i$ represents the response of a dipole source at \mathbf{x} on $\partial\mathbb{D}$, while n_i the outward-pointing unit vector normal to the boundary $\partial\mathbb{D}$. The asterisk ($*$) denotes complex conjugation, which corresponds to a time-reversed version of a quantity in the time domain (i.e., $G(\mathbf{x}_A, \mathbf{x}, -t)$ where t denotes time). Thus, the integrals in the right-hand side of Equation 1.2 become correlations in time after an inverse Fourier transform. $j = \sqrt{-1}$, and $\rho(\mathbf{x})$ the density at \mathbf{x} .

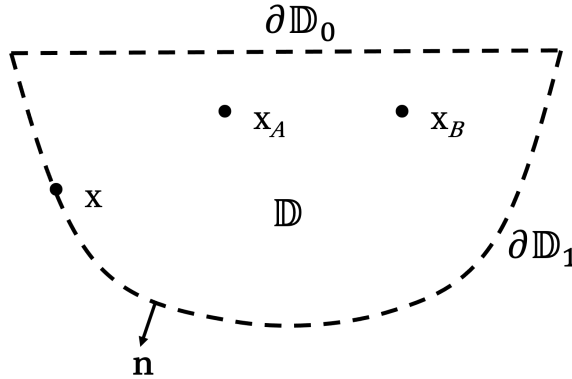


Figure 1.1: Arbitrary volume \mathbb{D} with enclosing boundary $\partial\mathbb{D} = \partial\mathbb{D}_0 + \partial\mathbb{D}_1$. \mathbf{x} is the integration point along the boundary. \mathbf{x}_A and \mathbf{x}_B are the observation points. \mathbf{n} is the outward-pointing unit vector normal to the boundary.

Assuming a far-field approximation [21] (i.e., all sources lie in the far-field, such that the distance from the source to the receivers is large compared to the wavelength) and

that rays are normal to the boundary $\partial\mathbb{D}$, the medium at and outside the boundary $\partial\mathbb{D}$ is homogeneous (with propagation velocity of acoustic waves V_P and density ρ , so that the energy going outwards from the surface is not scattered back inside \mathbb{D}), and the medium around the source points is locally smooth, the dipole terms in Equation 1.2 can be approximated by monopole terms, obtaining

$$A, B \in \mathbb{D}; \ 2\Re[G(\mathbf{x}_B, \mathbf{x}_A, \omega)] \approx \frac{2}{V_P \rho} \int_{\partial\mathbb{D}} \left[G(\mathbf{x}_B, \mathbf{x}, \omega) G^*(\mathbf{x}_A, \mathbf{x}, \omega) \right] d^2x. \quad (1.4)$$

In the time domain, Equation 1.4 indicates that the sum of the causal and acausal part of a virtual trace can be obtained by cross-correlating seismic records at two different receiver locations \mathbf{x}_A and \mathbf{x}_B for each source location, and then summing the cross-correlated traces over the sources. The seismic events recorded at \mathbf{x}_B for a virtual source at \mathbf{x}_A are then retrieved by cancelling overlapping paths. The latter comes from the summation of the correlated traces, which removes the propagation effects inside the medium. The summation will be constructive (dominant contribution to the integral) for the retrieval of physical events for sources located in the Fresnel zone around stationary points [36] – this is the so-called stationary-phase region (since the rays from such source positions are nearly parallel and interfere constructively in the summation). Therefore, the higher number of sources available, the better the SI result. Then, virtual sources can be retrieved at the position of the receivers, and, because of reciprocity, virtual receivers can be retrieved at the position of the sources. This can also be interpreted as redatuming of the data (Figure 1.2).

The retrieved physical events include direct body waves, reflections, and refractions, but possibly also surface waves, if the receivers are at an interface or at the surface. Additionally, from the cross-correlation of two orders of free-surface multiples, multiples are kinematically transformed into primaries or lower-order multiples (Figure 1.2).

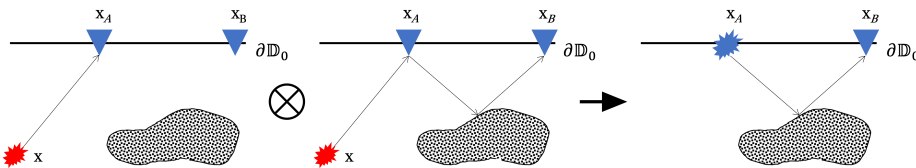


Figure 1.2: Correlation of a surface-related multiple recorded at receiver \mathbf{x}_B with a primary reflection recorded at receiver \mathbf{x}_A (blue triangles), followed by summation over sources at points \mathbf{x} (red explosions) along the boundary, yields the virtual primary. In this case, the source is redatumed from \mathbf{x} in the subsurface to a virtual source in \mathbf{x}_A (blue explosion).

The theory of SI requires that the sources effectively surround the receivers and illuminate them homogeneously [21]. When receivers are at the surface ($\partial\mathbb{D}_0$), sources are only required in the subsurface ($\partial\mathbb{D}_1$) [21]. However, for the usual seismic exploration survey, the active sources are present at the surface, where they are not required. Still, using stationary-phase arguments [36], it can be shown that also sources at the surface can be used for retrieval of reflection arrivals by, e.g., correlating a primary reflection with its free-surface multiple (Figure 1.3). Still, because having sources at the surface does not

comply with the theoretical requirements, the retrieved reflection events will have only the kinematics of reflections, while their amplitude and wavelet phases would be different from those that would be recorded from an active source at the position of the virtual source. Thus, these retrieved reflection events are referred to as pseudo-physical reflections [37]. A further consequence of having sources at the free surface (where they are not needed) is that the retrieved result would contain not only pseudo-physical arrivals, but also spurious contributions to the interferometric estimate like virtual refractions and non-physical reflections [38–44].

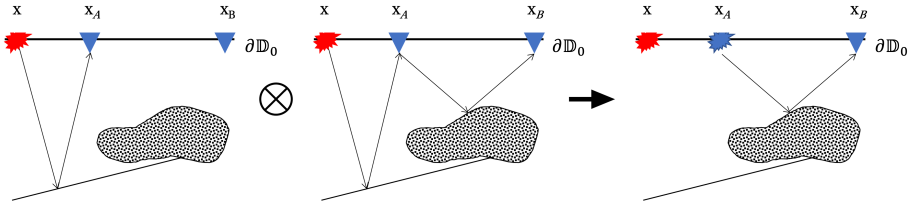


Figure 1.3: Correlation of a surface-related multiple recorded at receiver x_B with a primary reflection recorded at receiver x_A (blue triangles), followed by summation over surface sources (red explosions), retrieves a virtual pseudo-physical primary reflection. In this case, the source is redatumed from x in the surface to a virtual source in x_A (blue explosion).

In this thesis, we look at applications of SI to seismic and electromagnetic reflection surveys with active sources positioned at the surface. We also investigate the consequences of such source positioning to our advantage, especially in the context of mining and near-surface applications.

1.3. OUTLINE

This thesis is composed of the following chapters:

- Chapter 2: *Improved target illumination at Ludvika mines of Sweden through seismic-interferometric surface-wave suppression.*
In this chapter, we showcase the efficacy of applying SI surface-wave suppression to an active-source reflection seismic dataset acquired in the Ludvika mining area of Sweden. By applying SI, we retrieve dominant surface-wave estimates that represent the surface waves present in the field data. We then suppress the surface waves in the active-source data by adaptively subtracting the retrieved surface waves from the active-source data. The results are encouraging, as they open up new possibilities for denoising hard-rock seismic data for imaging mineral deposits using seismic reflections.
- Chapter 3: *Surface-wave suppression through seismic interferometry: a case study from the Siilinjärvi phosphate mine in Finland.*
In this chapter, we further consolidate the application of SI surface-wave suppression in hard-rock mining environments and we show how seismic methods and novel processing methodologies can be effectively utilised for mineral exploration.

Here, we apply the interferometric-suppression technique to an active-source reflection seismic dataset acquired at the Siilinjärvi mines in eastern Finland. The technique helps improve the subsequent processing steps, achieving results that show clearer reflections, sharper boundaries of the mineralisation with the surrounding rocks and, overall, an enhanced final image of the subsurface.

- Chapter 4: *Electromagnetic-interferometric direct-wave suppression for detection of shallow buried targets with GPR.*

In this chapter, we extend the approach of interferometric wave suppression from seismic wavefields to electromagnetic wavefields and near-surface data. Here, we show that an electromagnetic direct-wave estimate can be obtained after utilising electromagnetic interferometry. Subsequently, this estimate can be adaptively subtracted from the active-source data to effectively eliminate the direct wave. We apply this methodology to a ground-penetrating-radar dataset acquired at the Jewish Cemetery in Naaldwijk, The Netherlands. The earliest diffraction events that were covered by the direct arrival are visible after this processing, showing the effectiveness of the method for this application.

- Chapter 5: *Data reconstruction using seismic interferometry applied to active-source data from the Ludvika mines of Sweden.*

In this chapter, we utilise SI to retrieve reflection data to provide additional information to supply missing traces inside relatively large source gaps. We utilise a data-reconstruction algorithm based on a projection-onto-convex-sets image-restoration algorithm to merge active-source and virtual-source data. Here, we show that the utilisation of virtual-source data helps the interpolation algorithm better reconstruct the missing events. We apply the methodology to the active-source dataset acquired at the Ludvika Mines of Sweden. These data are very challenging to precisely recover active-source pseudo-physical reflections, increasing the difficulty for the interpolator to reconstruct the missing data. Nevertheless, the results utilising virtual-source data still exhibit improvements when comparing them to the results obtained directly from the data with the source gap.

- Chapter 6: *Interferometric data reconstruction in relatively large gaps utilising hyperbolic Radon transforms.*

In this chapter, we present a new, simple, and practical methodology to combine field active-source data with virtual-source data in a suitable way, focusing on land seismic data for near-surface applications. For this new approach of data reconstruction, we utilise the ability of Radon transforms to focus and separate hyperbolic events with different curvatures. In order to suppress the spurious events present in the SI responses, we perform filtering in the Radon domain, obtaining a more optimal SI result for merging. Despite not being at the quality of well-sampled field data, we show that a superior result can be provided after applying the proposed methodology, producing higher-resolution images of the subsurface compared to the original active-source data with the data gap present in it.

- Chapter 7: *Conclusions.*

This chapter summarises the main conclusions based on the results obtained

in the previous chapters. Additionally, recommendations for future research are made, which can help further develop the ideas and the methodologies proposed in this thesis.

REFERENCES

- [1] R. E. S. W. M. Telford, *Applied Geophysics* (Cambridge University Press, 2003).
- [2] R. F. Mamdouh R. Gadallah, *Exploration Geophysics* (Springer-Verlag GmbH, 2008).
- [3] A. Malehmir, R. Durrheim, G. Bellefleur, M. Urosevic, C. Juhlin, D. J. White, B. Milkereit, and G. Campbell, *Seismic methods in mineral exploration and mine planning: A general overview of past and present case histories and a look into the future*, *Geophysics* **77**, WC173 (2012).
- [4] S. Buske, G. Bellefleur, and A. Malehmir, *Introduction to special issue on "hard rock seismic imaging"*, *Geophysical Prospecting* **63**, 751 (2015).
- [5] A. Malehmir, M. Manzi, D. Draganov, U. Weckmann, and E. Auken, *Introduction to the special issue on "Cost-effective and innovative mineral exploration solutions"*, *Geophysical Prospecting* **68**, 3 (2019).
- [6] C. C. Pretorius, M. R. Muller, M. Larroque, and C. Wilkins, *16. a review of 16 years of hardrock seismics on the Kaapvaal Craton*, in *Hardrock Seismic Exploration* (Society of Exploration Geophysicists, 2003) pp. 247–268.
- [7] D. J. Verschuur, A. J. Berkhout, and C. P. A. Wapenaar, *Adaptive surface-related multiple elimination*, *Geophysics* **57**, 1166 (1992).
- [8] W. H. Dragoset and Ž. Jeričević, *Some remarks on surface multiple attenuation*, *Geophysics* **63**, 772 (1998).
- [9] S. Spitz, *Seismic trace interpolation in the F-X domain*, *Geophysics* **56**, 785 (1991).
- [10] M. Naghizadeh and M. D. Sacchi, *Multistep autoregressive reconstruction of seismic records*, *Geophysics* **72**, V111 (2007).
- [11] M. Naghizadeh and M. Sacchi, *Seismic data reconstruction using multidimensional prediction filters*, *Geophysical Prospecting* **58**, 157 (2010).
- [12] S. Fomel, *Seismic reflection data interpolation with differential offset and shot continuation*, *Geophysics* **68**, 733 (2003).
- [13] S. T. Kaplan, M. Naghizadeh, and M. D. Sacchi, *Data reconstruction with shot-profile least-squares migration*, *Geophysics* **75**, WB121 (2010).
- [14] S. Xu, Y. Zhang, D. Pham, and G. Lambaré, *Antileakage fourier transform for seismic data regularization*, *Geophysics* **70**, V87 (2005).
- [15] R. Abma and N. Kabir, *3D interpolation of irregular data with a POCS algorithm*, *Geophysics* **71**, E91 (2006).

- [16] F. J. Herrmann and G. Hennenfent, *Non-parametric seismic data recovery with curvelet frames*, *Geophysical Journal International* **173**, 233 (2008).
- [17] G. Hennenfent, L. Fenelon, and F. J. Herrmann, *Nonequispaced curvelet transform for seismic data reconstruction: A sparsity-promoting approach*, *Geophysics* **75**, WB203 (2010).
- [18] M. Naghizadeh and M. D. Sacchi, *Beyond alias hierarchical scale curvelet interpolation of regularly and irregularly sampled seismic data*, *Geophysics* **75**, WB189 (2010).
- [19] D. O. Trad, T. J. Ulrych, and M. D. Sacchi, *Accurate interpolation with high-resolution time-variant Radon transforms*, *Geophysics* **67**, 644 (2002).
- [20] A. Ibrahim, P. Terenghi, and M. D. Sacchi, *Simultaneous reconstruction of seismic reflections and diffractions using a global hyperbolic Radon dictionary*, *Geophysics* **83**, V315 (2018).
- [21] K. Wapenaar and J. Fokkema, *Green's function representations for seismic interferometry*, *Geophysics* **71**, SI33 (2006).
- [22] D. F. Halliday, A. Curtis, J. O. A. Robertsson, and D.-J. van Manen, *Interferometric surface-wave isolation and removal*, *Geophysics* **72**, A69 (2007).
- [23] A. J. Berkhout and D. J. Verschuur, *Imaging of multiple reflections*, *Geophysics* **71**, SI209 (2006).
- [24] Y. Wang, Y. Luo, and G. T. Schuster, *Interferometric interpolation of missing seismic data*, *Geophysics* **74**, SI37 (2009).
- [25] W. Curry and G. Shan, *Interpolation of near offsets using multiples and prediction-error filters*, *Geophysics* **75**, WB153 (2010).
- [26] Y. Wang, S. Dong, and Y. Luo, *Model-based interferometric interpolation method*, *Geophysics* **75**, WB211 (2010).
- [27] S. M. Hanafy and G. T. Schuster, *Interferometric interpolation of sparse marine data*, *Geophysical Prospecting* **62**, 1 (2013).
- [28] S. Dong, R. He, and G. T. Schuster, *Interferometric prediction and least squares subtraction of surface waves*, in *SEG Technical Program Expanded Abstracts 2006* (Society of Exploration Geophysicists, 2006).
- [29] D. Halliday and A. Curtis, *Seismic interferometry, surface waves and source distribution*, *Geophysical Journal International* **175**, 1067 (2008).
- [30] D. F. Halliday, A. Curtis, P. Vermeer, C. Strobba, A. Glushchenko, D.-J. van Manen, and J. O. Robertsson, *Interferometric ground-roll removal: Attenuation of scattered surface waves in single-sensor data*, *Geophysics* **75**, SA15 (2010).
- [31] O. Yilmaz, *Seismic data analysis: Processing, inversion, and interpretation of seismic data*, Society of Exploration Geophysics **Volume 1** (2001).

- [32] F. E. Ernst, G. C. Herman, and A. Ditzel, *Removal of scattered guided waves from seismic data*, *Geophysics* **67**, 1240 (2002).
- [33] L. Konstantaki, D. Draganov, R. Ghose, and T. Heimovaara, *Seismic interferometry as a tool for improved imaging of the heterogeneities in the body of a landfill*, *Journal of Applied Geophysics* **122**, 28 (2015).
- [34] J. Liu, D. Draganov, and R. Ghose, *Seismic interferometry facilitating the imaging of shallow shear-wave reflections hidden beneath surface waves*, *Near Surface Geophysics* **16**, 372 (2018).
- [35] D. Halliday and A. Curtis, *Seismic interferometry of scattered surface waves in attenuative media*, *Geophysical Journal International* **178**, 419 (2009).
- [36] G. Schuster, *Seismic interferometry* (Cambridge University Press, Cambridge, 2009).
- [37] K. L er, G. A. Meles, A. Curtis, and I. Vasconcelos, *Diffracted and pseudo-physical waves from spatially limited arrays using source–receiver interferometry (SRI)*, *Geophysical Journal International* **196**, 1043 (2013).
- [38] D. Mikesell, K. van Wijk, A. Calvert, and M. Haney, *The virtual refraction: Useful spurious energy in seismic interferometry*, *Geophysics* **74**, A13 (2009).
- [39] D. Draganov, R. Ghose, E. Ruigrok, J. Thorbecke, and K. Wapenaar, *Seismic interferometry, intrinsic losses and Q-estimation*, *Geophysical Prospecting* **58**, 361 (2010).
- [40] D. Draganov, R. Ghose, K. Heller, and E. Ruigrok, *Monitoring changes in velocity and q using non-physical arrivals in seismic interferometry*, *Geophysical Journal International* **192**, 699 (2012).
- [41] D. Draganov, K. Heller, and R. Ghose, *Monitoring CO2 storage using ghost reflections retrieved from seismic interferometry*, *International Journal of Greenhouse Gas Control* **11**, S35 (2012).
- [42] S. King and A. Curtis, *Suppressing nonphysical reflections in green's function estimates using source-receiver interferometry*, *Geophysics* **77**, Q15 (2012).
- [43] B. Boullenger and D. Draganov, *Interferometric identification of surface-related multiples*, *Geophysics* **81**, Q41 (2016).
- [44] J. Place and A. Malehmir, *Using supervirtual first arrivals in controlled-source hardrock seismic imaging—well worth the effort*, *Geophysical Journal International* **206**, 716 (2016).

2

IMPROVED TARGET ILLUMINATION AT LUDVIKA MINES OF SWEDEN THROUGH SEISMIC-INTERFEROMETRIC SURFACE-WAVE SUPPRESSION

In mineral exploration, new methods to improve the delineation of ore deposits at depth are in demand. For this purpose, increasing the signal-to-noise ratio through suitable data processing is an important requirement. Seismic reflection methods have proven to be useful to image mineral deposits. However, in most hard-rock environments, surface waves constitute the most undesirable source-generated or ambient noise in the data that, especially given their typical broadband nature, often mask the events of interest like body-wave reflections and diffractions. In this study, we show the efficacy of a two-step procedure to suppress surface waves in an active-source reflection seismic dataset acquired in the Ludvika mining area of Sweden. First, we use seismic interferometry to estimate the surface-wave energy between receivers, given that surface waves are the most energetic arrivals in the dataset. Second, we adaptively subtract the retrieved surface waves from the original shot gathers, checking the quality of the unveiled reflections. We see that several reflections, judged to be from the mineralisation zone, are enhanced and better visualised after this two-step procedure. Our comparison with results from frequency-wavenumber filtering verifies the effectiveness of our scheme, since the presence of linear artefacts is reduced. The results are encouraging, as they open up new possibilities for denoising hard-rock seismic data and, in particular, for imaging deep mineral deposits using seismic reflections. This approach is purely data-driven and does not require significant judgment on the dip and frequency content of present surface waves, which often vary from place to place.

This chapter was published as F. Balestrini, D. Draganov, A. Malehmir, P. Marsden, and R. Ghose, *Improved target illumination at Ludvika mines of Sweden through seismic-interferometric surface-wave suppression*, [Geophysical Prospecting](#) **68**, 200 (2019).

Minor changes have been applied to make the text and figures consistent with this thesis.

2.1. INTRODUCTION

The main aim of a mineral exploration programme is to discover new deposits in a cost-effective and environmentally-friendly manner. The exploration process usually starts by looking for mineral targets that can be of economic interest as observed in surface and aerial measurements, and by sampling geological areas that have a potential to yield commercially viable concentrations of minerals. It is important to determine if the exploration project is likely to be profitable. To do so, it is necessary to know the full extent of the mineralised horizons and their geometry, as well as their host rock.

The Bergslagen mineral district in central Sweden is characterised by several multi-commodity mineral deposits. In particular, the district is known by its iron-oxide apatite-bearing deposits, since they are the most abundant and economically important natural resources in this area Stephens *et al.* [1]. Our study area is located in Blötberget, part of the Bergslagen district and the Ludvika mines (Figure 2.1). The Blötberget iron-oxide deposit was exploited up to a depth of approximately 240 m, until the mining operations stopped in the year 1979 due to the low market price of iron ore [2]. However, new favourable market conditions accompanied by the increase of the iron-ore price a few years ago (2011-2014), which is currently between four and five times higher, encouraged a number of initiatives for a reassessment of the deposit and possible generation of new targets [3, 4].

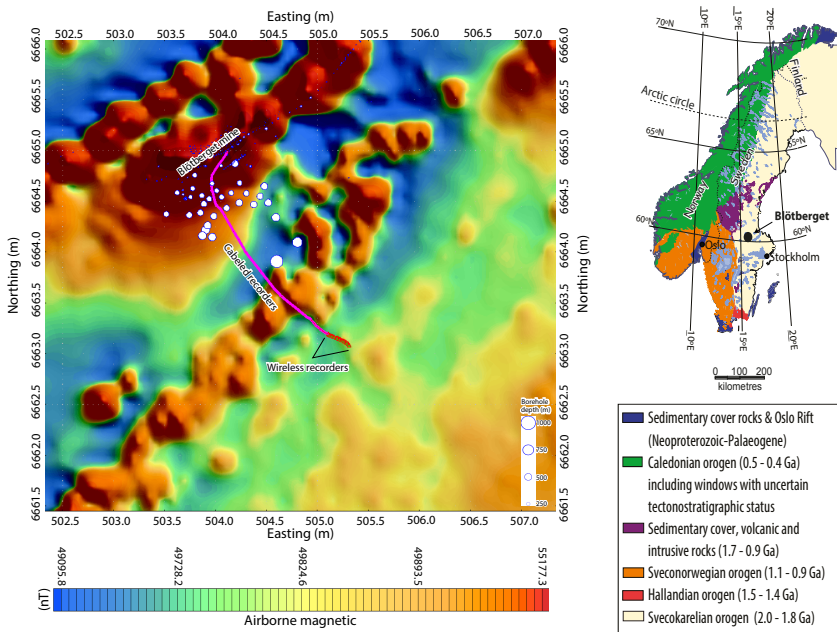


Figure 2.1: Magnetic map of the Blötberget mine showing the signature of the mineralisation zone and the location of the seismic profile (magenta line) used in this study. The white and blue circles indicate the position of boreholes used for downhole logging.

Currently, the ore deposits being mined are characterised by shallow depths due to the ease of their exploration and extraction. But as these ore deposits are already discovered, new ore discoveries in the near future would be at relatively larger depths. To explore for such deeper targets effectively, efficient and high-resolution methods are needed. In this regard, an ever-increasing utilisation of seismic methods in mineral exploration and mine planning is noteworthy (e.g., Eaton *et al.* [5], Koivisto *et al.* [6], Malehmir *et al.* [7] and references therein; Malinowski *et al.* [8], Manzi *et al.* [9], Buske *et al.* [10] and references therein). There is a significant growth in the last few years in the use of these methods due to their capability of exploring relatively greater depths (e.g., 850 m and deeper for our case) with higher resolution compared to other geophysical methods, making them more convenient for deep mineral exploration. However, because the seismic impedance contrast between the mineral deposit and the embedding medium is commonly low, a good signal-to-noise ratio is needed in order to enable better imaging and characterisation of the targets.

In exploration seismology, surface waves (sometimes also referred to as ground roll) constitute a form of source-generated energy. These waves propagate along the Earth's surface and are generally the most energetic arrivals in land seismic records. Surface waves are strongly influenced by the elastic properties of the subsurface and, therefore, contain information that could be useful to characterise the medium they propagate through [11]. However, when one aims to use reflected body waves for imaging, the surface waves are considered noise because they often mask the reflection events of interest, especially in high-noise, near-mine environments. That is why great efforts are required to suppress the surface waves [12], especially when the overburden is thick or has a large impedance contrast with the underlying crystalline bedrock.

As mentioned in Chapter 1, surface waves can be suppressed already in the field by deploying receiver arrays instead of single stations, or in the recorded data during processing using suitable filters in the f - k or f - x domains [13]. Such filtering methods can be ineffective when the surface waves occupy the same regions in the f - k or f - x domains as the reflected body waves that we wish to preserve [14, 15]. Additionally, an incorrect choice of the f - k or f - x filter parameters may generate artefacts, affecting the quality of the seismic images. In this study, we illustrate the application of a novel method of surface-wave noise suppression for deep mineral exploration through the utilisation of SI. Using SI, we estimate the surface-wave energy between receivers in a purely data-driven manner. We then subtract the retrieved surface-wave energy in an adaptive way from the original data to obtain shot gathers with higher signal-to-noise ratio. These results can be then used in seismic reflection-data processing and imaging. This technique has been referred to as interferometric surface-wave suppression by a number of authors studying the application of SI for the purpose of surface-wave suppression. Dong *et al.* [16] and Halliday *et al.* [17] showed results in the context of hydrocarbon exploration, whereas Konstantaki *et al.* [18] and Liu *et al.* [19] showed results for near-surface applications. These studies suggest how surface waves between two receivers could be retrieved by cross-correlating recorded traces at these receivers, and how subsequently these retrieved responses could be used for surface-wave suppression.

In this study, we apply interferometric surface-wave suppression for imaging the iron-oxide mineralisation in Blötberget, using seismic reflection data acquired in 2016

[2, 20]. This study is part of a larger effort in exploring the potential of the acquired seismic dataset at the site for delineating the deep iron-oxide mineralisation zone [21].

2.2. BLÖTBERGET IRON-OXIDE DEPOSIT

The study area, Blötberget in the Ludvika mining area (Figure 2.1), is located in Bergslagen in central Sweden, one of the major mineral districts in the country. The mineralisation in Bergslagen comprises of a banded-iron formation (BIF), skarn-type iron-oxide deposits, and apatite-rich iron-oxide deposits, with the latter deposits accounting for more than 40% of the iron ore produced in the country [22, 23]. Bergslagen has always been economically important, but due to the low metal prices in the 1980-1990s, output from the mines decreased or even stopped, leading to just a few mines operating in the region. In particular, Blötberget is well-known for its rich and high-quality iron-oxide deposit. However, the mining operation ceased in 1979, with most of the mining taking place at approximately 240 m depth at the time of closure. Nowadays, there is a renewed interest in exploring and mining this deposit, but also similar ones in the area, due to accessibility to the market and the recent advancements made in low-cost mining and metallurgical technologies. A number of recent works in the Blötberget and neighbouring areas are aimed at achieving a better understanding of the mineralisation at depth, as well as at technological developments (e.g., Malehmir *et al.* [2], Yehuwalashet and Malehmir [4], Place *et al.* [24]).

The mineralisation in Blötberget consists of magnetite and hematite. Additionally, apatite and small amounts of quartz and calc-silicate minerals are present. The deposit contains approximately 55 Mt of iron with an average iron content of 41%, dominantly from magnetite, but it is also composed of several horizons where hematite is rich or notably present. The hematite ores are less massive than the magnetite ones, and their skarn host-rock mineralogy is slightly different, containing more quartz and feldspar. The origin of the iron-oxide apatite-bearing deposit is considered to be synvolcanic, although this is disputed, with a new study favouring a magmatic to high-temperature hydrothermal origin [25]. The mineralised units dip moderately (about 45°) towards the southeast down to 500 m, at which depth they become gently dipping until the known depth of approximately 800-850 m (known from historical one-inch diameter holes; [3]). Deeper than that level, the mineralisation units still need to be explored [2, 3].

2.3. SEISMIC DATA ACQUISITION

The 2D reflection seismic dataset used in this study was acquired in a field campaign in 2016 that used both wireless and cabled recorders [20]. Figure 2.1 shows the seismic profile (magenta crooked line), along which the sources and receivers were positioned. The white and blue circles indicate the position of historical boreholes in the area. The profile was designed such that it intersects perpendicularly the strike direction of the known mineralisation in order to keep any possible cross-dip and 3D scattering effects to a minimum. The aim of the 2016 survey was to delineate any potential depth extension of the mineralisation toward the south-east, which could not be achieved in an earlier survey conducted in 2015 using mainly a landstreamer system. The landstreamer survey was characterised by a lower common midpoint (CMP) fold coverage and, as a result, could

only confirm the known mineralisation [2]. The 2016 survey consisted of two profiles. The data for these profiles were acquired using 10-Hz geophones. One of the profiles was located perpendicular to the first 2015 profile, and used 78 wireless units. This profile is not the focus of this study, and thus is not represented in Figure 2.1. The second profile (focus of this study) was positioned along the profile of the 2015 survey, but only north of road 50. On the northern part of the profile, 427 cabled units were used, followed by 24 wireless units on the southern end. The receiver spacing was 5 m, with a total profile length of around 2.2 km. A 500-kg Bobcat-mounted drophammer was used as the seismic source. In order to improve the signal-to-noise ratio (S/N), three shots were recorded next to each receiver station and subsequently stacked. The record length was of 2 s with a sampling rate of 1 ms.

Markovic *et al.* [26] showed the conventional processing results for this dataset merged with the 2015 dataset in order to improve the CMP fold and handle the low signal-to-noise ratio of the data in the area.

2.4. SEISMIC INTERFEROMETRY WITH ACTIVE SOURCES FOR SURFACE-WAVE RETRIEVAL

As explained in Chapter 1, SI generally refers to the principle of retrieving seismic responses from virtual sources by cross-correlating seismic observations at different receiver locations. One can distinguish between controlled-source and passive SI [27]. Controlled-source SI refers to the process of retrieving the response between two receivers \mathbf{x}_A and \mathbf{x}_B as if there was a source at one of the receiver locations. This process is carried out, most commonly, by cross-correlating the recordings at the two receivers and stacking the cross-correlations over all available controlled sources [28].

For an active-source seismic survey, the retrieved response between two receivers at positions \mathbf{x}_A and \mathbf{x}_B can be written in the frequency domain as [29]

$$\hat{u}(\mathbf{x}_B, \mathbf{x}_A, \omega) + \hat{u}^*(\mathbf{x}_B, \mathbf{x}_A, \omega) \approx \sum_{n=1}^N \hat{u}(\mathbf{x}_B, \mathbf{x}_n, \omega) \times \hat{u}^*(\mathbf{x}_A, \mathbf{x}_n, \omega), \quad (2.1)$$

where $\hat{u}(\mathbf{x}_B, \mathbf{x}_n, \omega)$ is the frequency-domain response of a recording at receiver \mathbf{x}_B from a source at \mathbf{x}_n . Note that Equation 2.1 is similar to Equation 1.4 but replacing the integration over $\partial\mathbb{D}$ with a summation over N numbers of active sources at the surface. If an active source emits an impulse, $\hat{u}(\mathbf{x}_B, \mathbf{x}_A, \omega)$ would represent an impulse response (i.e., $\hat{G}(\mathbf{x}_B, \mathbf{x}_A, \omega)$ in Equation 1.4). For transient sources, $\hat{u}(\mathbf{x}_B, \mathbf{x}_A, \omega)$ would represent a pressure or a particle velocity recording convolved with the autocorrelation of the sources' time function (in the frequency domain, this is, $\hat{u}(\mathbf{x}_B, \mathbf{x}_A, \omega) = \hat{G}(\mathbf{x}_B, \mathbf{x}_A, \omega) \hat{S}(\mathbf{x}, \omega)$, with $\hat{S}(\mathbf{x}, \omega) = \hat{s}^*(\mathbf{x}, \omega) \hat{s}(\mathbf{x}, \omega)$, and \hat{s} the source wavelet spectrum).

Through Equation 2.1, we can turn the receiver at \mathbf{x}_A into a virtual source. If we keep the receiver at \mathbf{x}_A fixed and repeat the correlation and summation process for all other receivers, the retrieved result would approximate a virtual common-source gather with a virtual source located at \mathbf{x}_A .

For a laterally homogeneous medium, sources at points in-line with the receivers, whose recordings are to be correlated, contribute to the retrieval of direct body or surface wave arrivals, since they all fall in the so-called stationary-phase region [30]. For retrieval

of direct (P-, S-, or surface) waves from active sources at the surface, all in-line points are stationary (Figure 2.2); for retrieval of pseudo- or non-physical reflections and scattered surface waves only a few points are stationary. This way, the result retrieved by SI will be dominated by surface waves. Note that if we assume that the surface sources mainly contribute to excitement of the fundamental mode, the fundamental mode retrieved by SI would be correct. To retrieve also higher modes, sources in the subsurface are required as well [31–34].

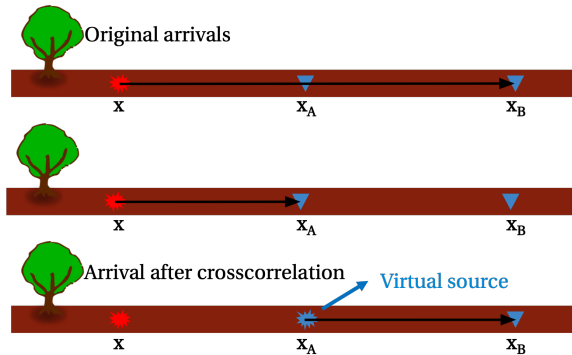


Figure 2.2: Correlation of direct or surface waves recorded at receiver x_B and x_A from a source in x yields to the retrieval of direct or surface waves between the receivers. In this case, the source is redatumed from x to a virtual source in x_A .

If each source position within an exploration survey is located near a receiver position, then a corresponding retrieved virtual source–receiver pair with its estimated surface waves can be found for each active source–receiver pair. This is needed in order to obtain virtual-source gathers with surface-wave estimations that properly represent the surface waves in the active-shot gathers. These estimates can then be adaptively subtracted from the full responses recorded in the field, thus applying interferometric surface-wave suppression [15–17, 19].

For this study, in order to test the interferometric surface-wave suppression and extraction method on the Blötberget seismic reflection dataset, we isolate and process only the 2016 dataset (magenta line in Figure 2.1) since it is the most complete one, the source and receiver spacing is more regular, and it has no complication due to landstreamer overlaps. All these factors help us avoid challenges in the retrieval of the seismic-interferometric responses. From this part of the 2016 dataset, we have not used the northernmost 50 stations for surface-wave retrieval. These stations correspond to the curved part of the 2016 line, for which the active sources are positioned in line only with a few neighbouring receivers, precluding retrieval of direct surface waves. Note that in the particular situation of the Ludvika seismic data, there are receivers at every active-source location. Therefore, we can safely assume that the surface waves are well-represented at each po-

sition.

2.5. ADAPTIVE SUBTRACTION

To perform adaptive subtraction, we estimate a shaping filter that minimises the difference between the field-recorded data with the surface waves and the surface waves retrieved by the application of SI to the field-recorded data. In other words, we solve the following minimisation problem for \mathbf{f} using the least-squares criterion,

$$\min_{\mathbf{f}} \|\mathbf{D} - \mathbf{f}\mathbf{D}_{SW}\|, \quad (2.2)$$

where \mathbf{D} is data with all the information (raw data) and \mathbf{D}_{SW} are the surface waves retrieved by SI applied to \mathbf{D} . The vertical double bars ($\|\cdot\|$) denote the L2-norm. After obtaining \mathbf{f} , the data with reflections after suppression of the surface waves \mathbf{D}_{refl} are obtained by

$$\mathbf{D}_{refl} = \mathbf{D} - \mathbf{f}\mathbf{D}_{SW}, \quad (2.3)$$

where the multiplication (or convolution in time) between the estimated shaping filter \mathbf{f} and \mathbf{D}_{SW} leads to $\mathbf{f}\mathbf{D}_{SW}$, which then is directly subtracted from \mathbf{D} , giving \mathbf{D}_{refl} . Equation 2.2 is solved using an iterative least-squares fit with a conjugate-gradient algorithm to design the 2D matching filters [35, 36]. We perform different tests (shown in the following section) by varying the parameters of the adaptive subtraction (e.g., filter length and time and space windows) in order to find the most suitable filter that suppresses the surface waves in an optimal way, minimising the filter artefacts.

2.6. RESULTS

The primary aim of this study is to illustrate the effectiveness of the interferometric surface-wave suppression method, applied to shot gathers of field data (Blötberget 2016 dataset, Maries *et al.* [3]). For this reason, the data-processing work follows a simple and conventional common midpoint (CMP) stacking workflow after suppression of the surface waves. Table 2.1 shows a summary of the processing steps that we implement to suppress the surface waves and to process the seismic data in order to obtain the final stacked section. We apply SI to the recorded active-source data in order to estimate the surface wave energy between the receivers. We then adaptively subtract the retrieved result from the original active data to suppress the surface waves. Prior to surface-wave suppression, the data are subjected to surface-consistent refraction static corrections [2, 26]. Before applying SI, we first filter the data using a band-pass filter between 20 and 45 Hz, by studying the power spectra of several shot gathers. The main idea is to reject frequencies that might contain reflection and refraction information in order to have the SI data that retrieve predominantly the surface waves, while having nearly no reflection energy retrieved. Even though the application of SI to data from active sources recorded at the surface naturally suppresses retrieval of body-wave reflections and favours the retrieval of surface waves, this extra step of filtering for reflection attenuation only strengthens the surface-wave retrieval.

Malehmir *et al.* [2], Markovic *et al.* [26] showed in their work the reflections to be interpreted from the mineralisation zone already visible in a raw shot gather; those reflections become more evident after a few pre-stack processing operations. In Figure 2.3,

| Step | Instruction |
|------|---|
| 1 | Raw data with static corrections applied |
| 2 | Band-pass filter 10 – 20 – 40 – 50 Hz |
| 3 | SI to estimate the surface waves |
| 4 | Adaptive subtraction of the estimated surface waves |
| 5 | 20 Hz low-cut filter |
| 6 | Automatic gain correction (AGC) |
| 7 | Velocity analysis |
| 8 | Normal Move Out (NMO) correction |
| 9 | Common midpoint/ensemble stack |

Table 2.1: Steps to suppress surface waves and process seismic reflection data to obtain the final stacked section.

we show an example of a common-source gather as recorded in the field. In green, we highlight the surface waves that contaminate the data and interfere with the known mineralisation-related reflections (red arrows).

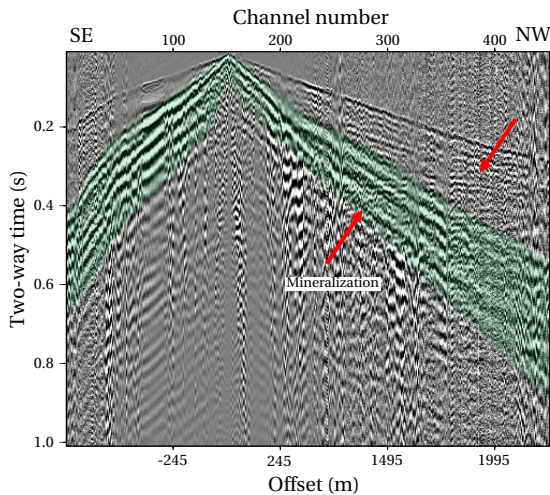


Figure 2.3: Example of one of the common-shot gather acquired in the field (Ludvika mine), which is used for adaptive subtraction of surface waves. The active source is positioned at station 150. In green, we highlight the surface waves that contaminate the dataset and overlap the mineralisation-zone reflections (red arrows).

We subject such common-source gathers to band-pass filtering and application of SI. Figure 2.4 shows the retrieved surface waves after the application of SI. We can note that the retrieved surface waves are dominant and well-represented (green areas). We then perform adaptive subtraction of the result in Figure 2.4 from the original data in Figure 2.3. Figure 2.5 shows the result for the same shot gather as in Figure 2.3 but after surface-wave removal and after applying a low-cut (20 Hz) filter in order to suppress re-

maining surface-wave energy. It can be seen that the surface waves are suppressed, and the reflections from the mineralisation zone (red arrows) can now be appreciated also at later times. The mineralisation signature is represented by reflection events that are hyperbolic in nature, though in this case, they exhibit very little curvature. [Figure 2.6a](#), [Figure 2.6b](#), and [Figure 2.6c](#) show the results when using a filter length of 50, 100, and 200 samples, respectively. While changing the time and space window sizes does not generate appreciable variations, we can see that increasing the filter length generates undesired artefacts at earlier times (red circles). Therefore, we apply [Equation 2.2](#) using 2D windows (spatial width of 5 traces, time length of 0.1 s) with a filter length of 50 samples and an iterative least-squares fit with a conjugate-gradient algorithm to design the 2D matching filters [[35](#), [36](#)].

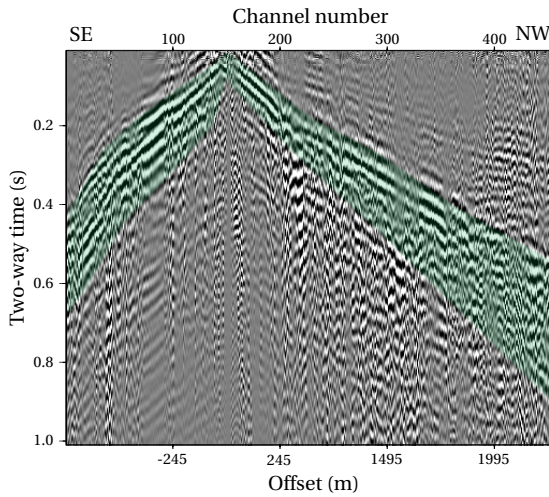


Figure 2.4: Result of application of SI for retrieval of the response of a virtual source at station 150, to be used as an estimation of the surface-wave energy. Highlighted in green are the retrieved surface waves. It can be seen that they are dominant and well represented.

To compare these results with results derived from techniques that are commonly applied, for example, f - k filtering, we perform a power-spectrum analysis and design a polygon filter for each common-shot gather to reject the surface-wave noise. In order to avoid the suppression of frequencies representing reflection energy, we constrain the filters between 5 and 60 Hz frequency and 1400 and 3400 m/s velocity. In [Figure 2.7](#), we present the result of the application of the designed f - k filter to the common-shot gather in [Figure 2.3](#). It can be observed that the surface-wave noise is suppressed as well. However, comparing this result with the one obtained from the interferometric surface-wave suppression, we see that some high-amplitude linear events (yellow arrows in [Figure 2.7](#)) still remain after the f - k filtering, while they are suppressed in [Figure 2.5](#). These linear events represent remaining surface-wave energy, which is still present as the f - k filter was designed in order to preserve the reflection events of interest. Additionally, the application of the f - k filter has produced some linear artefacts (magenta arrows in

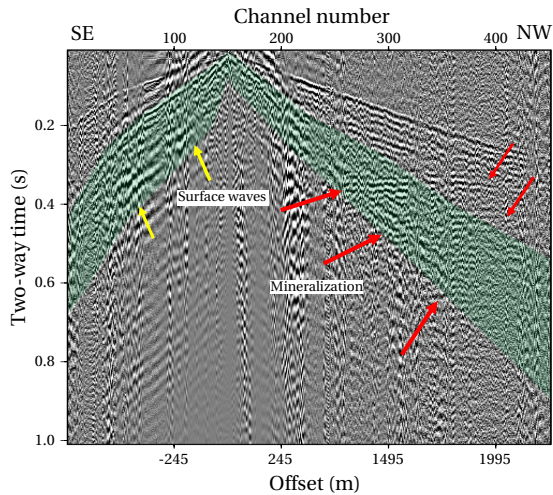


Figure 2.5: Result after adaptively subtracting the surface waves estimated using SI (Figure 2.4) from the original raw data (Figure 2.3). The part of the dataset where surface waves were filtered is highlighted in green. Surface waves are suppressed, and the mineralisation-zone signature is better illuminated (red arrows). The yellow arrows indicate the remaining surface-wave energy.

Figure 2.7). Furthermore, the seismic reflection signature of the mineralisation zone is better preserved in Figure 2.5.

Figure 2.8a, Figure 2.8b, and Figure 2.8c show the power spectrum in the f - k domain for the same shot gather prior to any processing, after interferometric surface-wave suppression, and after f - k filtering, respectively. We can easily identify the surface waves in Figure 2.8a (red area); this helps the selection of parameters and the design of the f - k filter as mentioned above. Comparing Figure 2.8b and Figure 2.8c, we can see that both methods are effective and help suppress the surface-wave energy. However, it is also clear that the use of f - k filters results in a very aggressive suppression of the frequencies and that, in this case, some artefacts are produced.

After the suppression of the surface waves, we apply a conventional processing sequence to obtain the stacked seismic section. We first apply AGC for amplitude balancing. After that, we obtain a preliminary stacked section using a 1D velocity model. The 1D velocity model is built using a root-mean-square velocity obtained for one representative common midpoint (CMP) gather. The CMP spacing is 2.5 m. As expected, the CMP fold increases at the centre of the line where a better illumination is achieved.

Figure 2.9a, Figure 2.9b, and Figure 2.9c show the preliminary unmigrated stacked sections between CMP 270 and CMP 860 using the 1D velocity model obtained from the raw dataset, from the dataset after surface-wave suppression using f - k filtering and from the data after interferometric surface-wave suppression, respectively. The latter two results already show improved imaging of the mineralisation zone (red arrows), which is represented by linear reflectors slightly dipping in the SE direction. It is clear that the high-amplitude and high-frequency linear events, which represent surface-

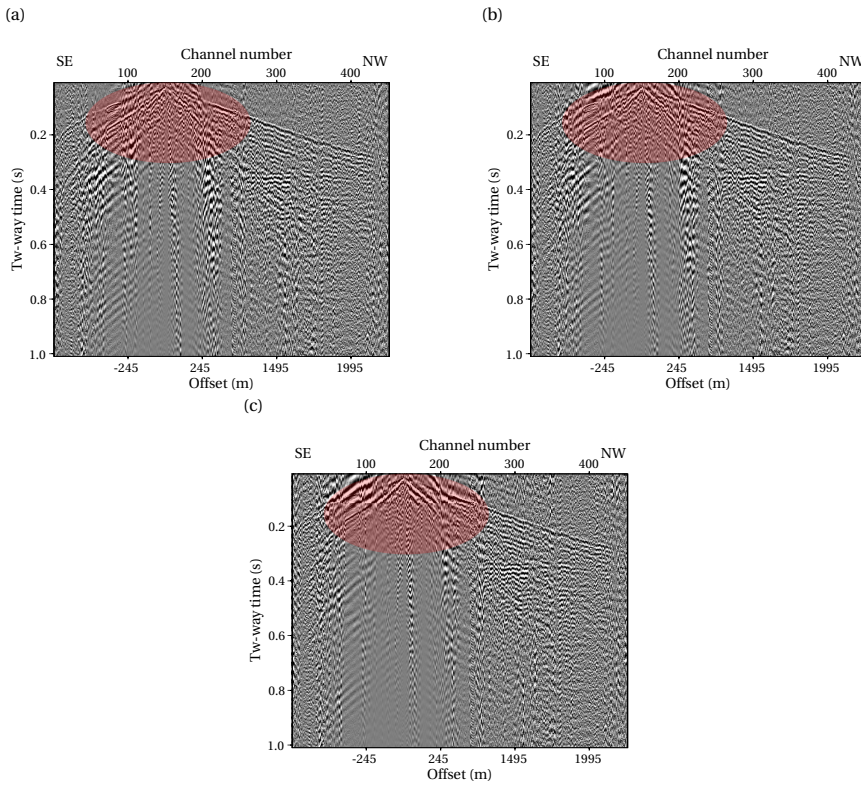


Figure 2.6: Results at station 150 after adaptively subtracting the surface waves estimated using SI (Figure 2.4) with filter lengths of (a) 50, (b) 100 and (c) 200 samples. The red circles indicate the areas where the filter artefacts arise.

wave noise, are well suppressed in both cases (Figure 2.9b and Figure 2.9b). Nevertheless, in the case of interferometric surface-wave suppression, the linear noise artefacts are avoided, and the mineralisation zone is better imaged. Note that even though the interferometric suppression of surface waves performs better, it does not suppress all the surface-wave energy (yellow arrows in Figure 2.5). Therefore, we can see steeper linear events in the stacked section that we interpret as surface-wave energy that still remains (yellow arrows in Figure 2.9c) at places corresponding to a lower CMP fold in the active-source data.

Note further that the seismic stacked section after interferometric surface-wave suppression also reveals a shallower, slightly curved reflector around 0.1 s. Such a reflector is obscured by linear surface-wave noise in Figure 2.9a and partly covered by the remaining surface-wave noise (and possibly by f-k filtering artefacts) in Figure 2.9b (yellow arrows).

Through generating constant-velocity stacks, we perform a velocity analysis along the line to better image the mineralisation-zone reflections and new potential geological structures. This velocity analysis is carried out by generating constant-velocity stacks between 3000 and 8000 m/s with an increment of 100 m/s. After this, we create a 2D

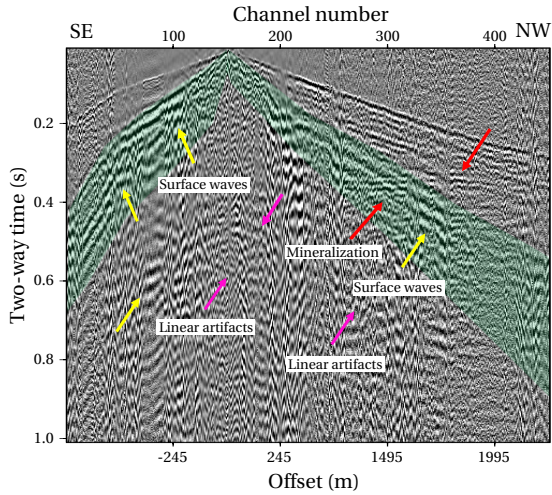


Figure 2.7: Result after the suppression of the surface waves using an f-k filter on the shot gather shown in Figure 2.3. The part of the dataset where surface waves were filtered is highlighted in green. The yellow arrows indicate the remaining surface-wave energy; the magenta arrows point to linear artefacts produced by the f-k filter.

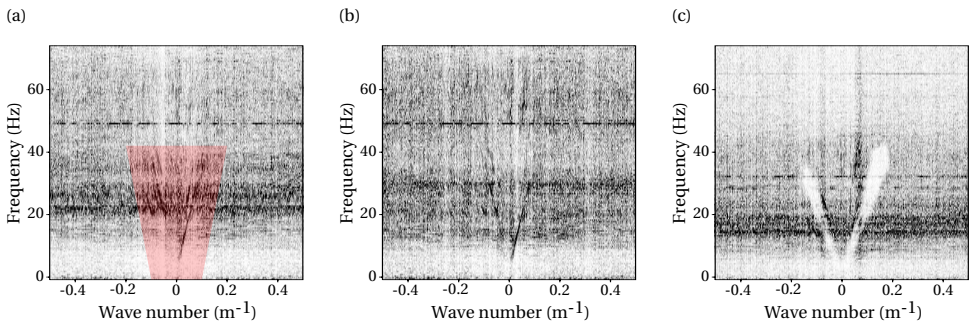


Figure 2.8: Power spectrum in the f-k domain for (a) the shot gather prior to any processing, (b) the same shot gather after interferometric surface-wave suppression and (c) after surface-wave suppression using f-k filtering. The red area highlights the part where the surface waves are located.

velocity model to generate a final stacked section of the subsurface. Only a conventional CMP processing flow is applied, focusing on noise attenuation and signal enhancement by frequency filtering.

Figure 2.10a, Figure 2.10b, and Figure 2.10c show the unmigrated stacked section of the subsurface between CMP 270 and CMP 860 using the picked 2D velocities and applied to the raw dataset, to the data with surface waves suppressed using f-k filtering and to the data after interferometric surface-wave suppression, respectively. Again, we obtain better results for interferometric surface-wave suppression. We can see that the images are clearer for both surface-wave filtering methods, using the same velocity

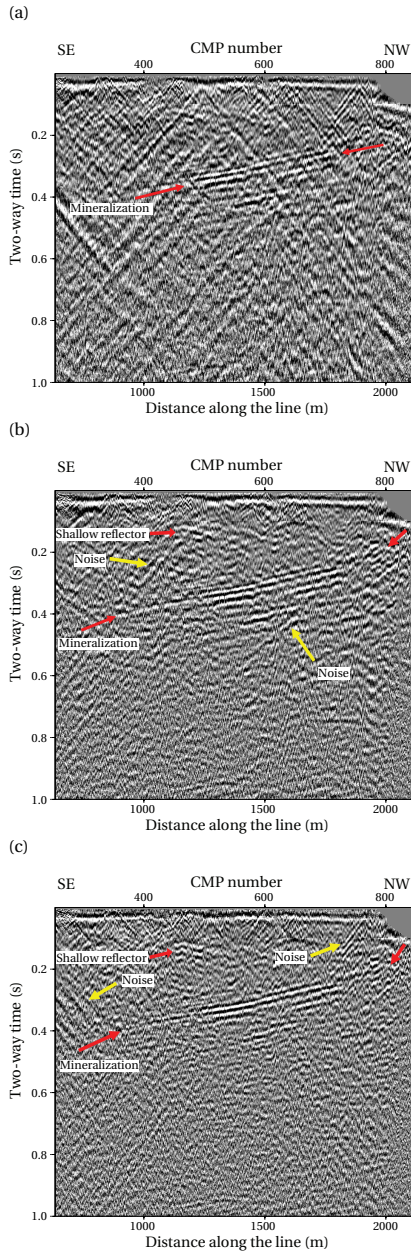


Figure 2.9: Preliminary unmigrated stacked section, using an 1D velocity model obtained from (a) the raw dataset, (b) the dataset after surface-wave suppression using the f-k filter and (c) the dataset after interferometric surface-wave suppression. The red arrows point to the imaged mineralisation zone. The yellow arrows mark artefacts generated by f-k filtering and noises that remain in the dataset.

model. However, [Figure 2.10c](#), which corresponds to interferometric surface-wave suppression, appears to be less noisy and the mineralisation-zone reflectors (red arrows) are more continuous. We notice some linear events in [Figure 2.10b](#) (yellow arrows) which are artefacts of the f-k filtering due to remaining surface-wave energy. The shallower structures at earlier times (around 0.1 s) are, once again, clearer when interferometric surface-wave suppression is performed.

In order to quantify the comparison between these two techniques, we calculate the S/N for the latter obtained images ([Figure 2.10](#)) using the raw data, using the data after f-k filtering for surface-wave suppression, and using the data after interferometric surface-wave suppression. We select two windows from these images, one window to represent the signal (where the mineralisation-zone reflections are located), and a second window to represent the background energy (i.e., the noise). We then compute the ratio of their summed squared magnitude to obtain the S/N. We choose both windows between CMP 500 and CMP 630. The window corresponding to the signal is located between 310 and 400 ms, and the window representing the noise is located between 550 and 640 ms. For the image obtained using the raw data, the S/N is 5.25. For the image obtained using the data after f-k filtering for surface-wave suppression, the S/N is 6.03. For the image obtained using the data after interferometric surface-wave suppression, the S/N is 6.94. Therefore, while both surface-wave suppression techniques improve the S/N, the interferometric surface-wave suppression performs clearly better, resulting in a greater improvement of the subsurface image. We perform a second comparison using the same signal window but moving the noise window to a later time, placing it between 850 and 960 ms. In this case, for the image obtained using raw data, the S/N is 7.15. For the image obtained using data after f-k filtering for surface-wave suppression, the S/N is 8.07. For the image obtained using data after interferometric surface-wave suppression, the S/N is 8.09. Again, both surface-wave suppression techniques show increased S/N, but the interferometric surface-wave suppression slightly outperforms the suppression using f-k filtering.

2.7. CONCLUSIONS

We have processed a reflection seismic dataset acquired for exploration of the iron oxide mineralisation zone in Blötberget, in the Ludvika mining area, south-central Sweden. We applied seismic interferometry to retrieve dominant surface waves between receivers while minimising the retrieved reflection energy. The retrieved dominant surface waves were then adaptively subtracted from the original data. We showed that, compared to other surface-wave suppression methods, the interferometric method can naturally predict the surface waves in the shot gather without the use of any a priori velocity model, resulting in a fully data-driven suppression of surface waves.

We compared stacked sections obtained through the interferometric surface-wave suppression with stacked sections of the raw data (no surface-wave suppression) and with stacked sections where the surface waves were suppressed using frequency-wavenumber filtering. Our results showed not only an improved delineation of the mineralisation zone using the interferometric surface-wave suppression, but also the delineation of new features above and below the known ore deposit.

Our study also aims to show the value of legacy data, and how they could be opti-

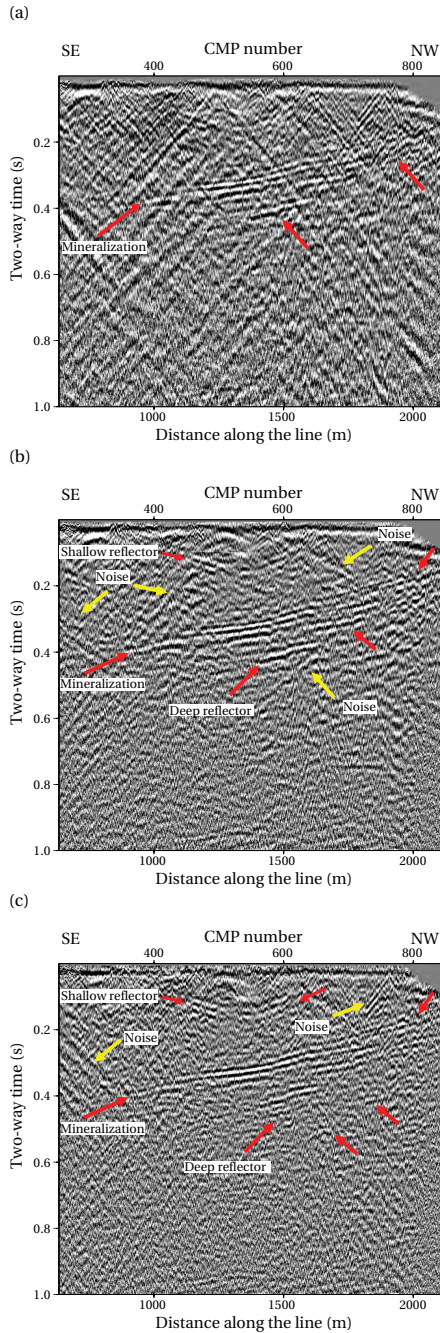


Figure 2.10: As in Figure 2.9, but using the picked 2D velocity model.

mally reprocessed using new seismic techniques in order to allow the generation of new mineral exploration targets. It further illustrates the potential of seismic methods in the exploration of deep deposits.

2

2.8. ACKNOWLEDGEMENTS

This study was carried out within the Smart Exploration project. Smart Exploration has received funding from the European Union's Horizon 2020 research and innovation programme under grant agreement number 775971. We thank Uppsala University and Nordic Iron Ore AB (NIO) for providing access to the datasets and for collaborating with us through the Smart Exploration project. Seismic data were processed using a combination of Seismic Unix, ProMAX and the software from the Delphi Consortium. We would like to thank two anonymous reviewers for their constructive comments that helped improve this manuscript.

REFERENCES

- [1] M. Stephens, M. Ripa, I. Lundström, L. Persson, T. Bergman, M. Ahl, C.-H. Wahlgren, P.-O. Persson, and L. Wickström, *Synthesis of bedrock geology in the Bergslagen region, Fennoscandian Shield, south-central Sweden*, Vol. v. 58 (2009).
- [2] A. Malehmir, G. Maries, E. Bäckström, M. Schön, and P. Marsden, *Developing cost-effective seismic mineral exploration methods using a landstreamer and a drophammer*, *Scientific Reports* **7** (2017), [10.1038/s41598-017-10451-6](https://doi.org/10.1038/s41598-017-10451-6).
- [3] G. Maries, A. Malehmir, E. Bäckström, M. Schön, and P. Marsden, *Downhole physical property logging for iron-oxide exploration, rock quality, and mining: An example from central Sweden*, *Ore Geology Reviews* **90**, 1 (2017).
- [4] E. Yehuwalashet and A. Malehmir, *Gravity and magnetic survey, modeling and interpretation in the Blötberget iron-oxide mining area of central Sweden*, *SEG Technical Program Expanded Abstracts 2018*, (2018), [10.1190/segam2018-2992225.1](https://doi.org/10.1190/segam2018-2992225.1).
- [5] D. W. Eaton, B. Milkereit, and M. Salisbury, *Seismic methods for deep mineral exploration: Mature technologies adapted to new targets*, *The Leading Edge* **22**, 580 (2003).
- [6] E. Koivisto, A. Malehmir, P. Heikkinen, S. Heinonen, and I. Kukkonen, *2D reflection seismic investigations at the Kevitsa Ni-Cu-PGE deposit, northern Finland*, *Geophysics* **77**, WC149 (2012).
- [7] A. Malehmir, R. Durrheim, G. Bellefleur, M. Urosevic, C. Juhlin, D. J. White, B. Milkereit, and G. Campbell, *Seismic methods in mineral exploration and mine planning: A general overview of past and present case histories and a look into the future*, *Geophysics* **77**, WC173 (2012).
- [8] M. Malinowski, E. Schetselaar, and D. J. White, *3D seismic imaging of volcanogenic massive sulfide deposits in the Flin Flon mining camp, Canada: Part 2 — Forward modeling*, *Geophysics* **77**, WC81 (2012).

- [9] M. S. D. Manzi, M. A. S. Gibson, K. A. A. Hein, N. King, and R. J. Durrheim, *Application of 3D seismic techniques to evaluate ore resources in the West Wits Line goldfield and portions of the West Rand goldfield, South Africa*, *Geophysics* **77**, WC163 (2012).
- [10] S. Buske, G. Bellefleur, and A. Malehmir, *Introduction to special issue on “hard rock seismic imaging”*, *Geophysical Prospecting* **63**, 751 (2015).
- [11] P. M. Shearer, *Introduction to Seismology* (Cambridge University Press, 2009).
- [12] E. Roots, A. J. Calvert, and J. Craven, *Interferometric seismic imaging around the active Lalor mine in the Flin Flon greenstone belt, Canada*, *Tectonophysics* **718**, 92 (2017).
- [13] Öz Yilmaz, *Seismic Data Analysis* (Society of Exploration Geophysicists, 2001).
- [14] Y. Xue, S. Dong, and G. T. Schuster, *Interferometric prediction and subtraction of surface waves with a nonlinear local filter*, *Geophysics* **74**, S11 (2009).
- [15] L. Konstantaki, D. Draganov, R. Ghose, and T. Heimovaara, *Seismic interferometry as a tool for improved imaging of the heterogeneities in the body of a landfill*, *Journal of Applied Geophysics* **122**, 28 (2015).
- [16] S. Dong, R. He, and G. T. Schuster, *Interferometric prediction and least squares subtraction of surface waves*, in *SEG Technical Program Expanded Abstracts 2006* (Society of Exploration Geophysicists, 2006).
- [17] D. F. Halliday, A. Curtis, P. Vermeer, C. Strobbia, A. Glushchenko, D.-J. van Manen, and J. O. Robertsson, *Interferometric ground-roll removal: Attenuation of scattered surface waves in single-sensor data*, *Geophysics* **75**, SA15 (2010).
- [18] L. A. Konstantaki, R. Ghose, D. Draganov, G. Diaferia, and T. Heimovaara, *Characterization of a heterogeneous landfill using seismic and electrical resistivity data*, *Geophysics* **80**, EN13 (2015).
- [19] J. Liu, D. Draganov, and R. Ghose, *Seismic interferometry facilitating the imaging of shallow shear-wave reflections hidden beneath surface waves*, *Near Surface Geophysics* **16**, 372 (2018).
- [20] G. Maries, A. Malehmir, E. Backström, M. Schön, and P. Marsden, *Reflection seismic imaging of iron-oxide deposits - an example from bergslagen mining district of sweden, 23rd European Meeting of Environmental and Engineering Geophysics*, (2017), [10.3997/2214-4609.201702092](https://doi.org/10.3997/2214-4609.201702092).
- [21] A. Malehmir, P. Holmes, P. Gisselø, L. Socco, J. Carvalho, P. Marsden, A. Verboon, and M. Loska, *Smart exploration: Innovative ways of exploring for the raw materials in the EU*, in *81st EAGE Conference and Exhibition 2019* (European Association of Geoscientists & Engineers, 2019).
- [22] N. Magnusson, *The Origin of the Iron Ores in Central Sweden and the History of Their Alterations*, Ser C. Avhandlingar och uppsatser (Svensk reproduktions AB (distr.), 1970).

- [23] M. B. Stephens, M. Ahl, T. Bergman, I. Lundström, L. Persson, M. Ripa, and C.-H. Wahlgren, *Syntes av berggrundsgeologisk och geofysisk information, bergslagen och omgivande områden., regional berggrundsgeologisk undersökning*. Sammanfattning av pågående undersökningar 1999. ed. Sveriges geologiska undersökning Rapporten och medde – landen 102 (2000).
- [24] J. Place, A. Malehmir, K. Högdahl, C. Juhlin, and K. P. Nilsson, *Seismic characterization of the Grängesberg iron deposit and its mining-induced structures, central Sweden*, [Interpretation 3, SY41 \(2015\)](#).
- [25] E. Jonsson, V. R. Troll, K. Högdahl, C. Harris, F. Weis, K. P. Nilsson, and A. Skelton, *Magmatic origin of giant 'kiruna-type' apatite-iron-oxide ores in central sweden*, [Scientific Reports 3 \(2013\), 10.1038/srep01644](#).
- [26] M. Markovic, G. Maries, A. Malehmir, J. Ketelhodt, E. Bäckström, M. Schön, and P. Marsden, *Deep reflection seismic imaging of iron-oxide deposits in the Ludvika mining area of central Sweden*, [Geophysical Prospecting 68, 7 \(2019\)](#).
- [27] K. Wapenaar, D. Draganov, and J. O. A. Robertsson, eds., *Seismic Interferometry* (Society of Exploration Geophysicists, 2008).
- [28] K. Wapenaar and J. Fokkema, *Green's function representations for seismic interferometry*, [Geophysics 71, SI33 \(2006\)](#).
- [29] D. F. Halliday, A. Curtis, J. O. A. Robertsson, and D.-J. van Manen, *Interferometric surface-wave isolation and removal*, [Geophysics 72, A69 \(2007\)](#).
- [30] R. Snieder, *Extracting the Green's function from the correlation of coda waves: A derivation based on stationary phase*, [Physical Review E 69, 046610 \(2004\)](#).
- [31] D. Halliday and A. Curtis, *Seismic interferometry, surface waves and source distribution*, [Geophysical Journal International 175, 1067 \(2008\)](#).
- [32] W. P. Kimman and J. Trampert, *Approximations in seismic interferometry and their effects on surface waves*, [Geophysical Journal International, no \(2010\)](#).
- [33] K. N. van Dalen, K. Wapenaar, and D. F. Halliday, *Surface wave retrieval in layered media using seismic interferometry by multidimensional deconvolution*, [Geophysical Journal International 196, 230 \(2014\)](#).
- [34] K. N. van Dalen, T. D. Mikesell, E. N. Ruigrok, and K. Wapenaar, *Retrieving surface waves from ambient seismic noise using seismic interferometry by multidimensional deconvolution*, [Journal of Geophysical Research: Solid Earth 120, 944 \(2015\)](#).
- [35] D. J. Verschuur, A. J. Berkhout, and C. P. A. Wapenaar, *Adaptive surface-related multiple elimination*, [Geophysics 57, 1166 \(1992\)](#).
- [36] A. Guitton and D. J. Verschuur, *Adaptive subtraction of multiples using the L1 -norm*, [Geophysical Prospecting 52, 27 \(2004\)](#).

3

SURFACE-WAVE SUPPRESSION THROUGH SEISMIC INTERFEROMETRY: A CASE STUDY AT THE SIILINJÄRVI PHOSPHATE MINE IN FINLAND

In near-mine environments, seismic data usually suffer from high level of noise. Furthermore, data are often characterised by low-impedance contrasts between the host rock and the mineral deposits. Additionally, when seismic methods are utilised, the employed active sources generate surface waves that introduce another type of high-amplitude noise and pose a further challenge to the seismic-data denoising and processing stage. In this work, we show a data-driven methodology for surface-waves suppression in active-source reflection seismic data acquired in 2018 at the Siilinjärvi mine in eastern Finland. By applying seismic interferometry to the active-source data, we retrieve dominant surface waves between receivers that we use as surface-wave estimates. We then use this result and adaptively subtract the estimated surface waves from the original data. After applying several processing steps for further denoising, data enhancement, and imaging, we obtain a migrated stacked section that shows clearer reflections and an enhanced image of the subsurface as a result of a well-achieved surface-wave suppression that helps improve the subsequent processing steps.

This chapter was published as F. Balestrini, D. Draganov, R. Ghose, E. Koivisto, A. Malehmir, and M. Savolainen, *Surface-wave suppression through seismic interferometry: A case study at the Siilinjärvi phosphate mine in Finland*, in [SEG Technical Program Expanded Abstracts 2020](#) (Society of Exploration Geophysicists, 2020). Note that changes have been applied to make the text and figures consistent with this thesis.

3.1. INTRODUCTION

Phosphate rock has been listed as one of the 26 critical raw materials for the European Union [1]. Of the total amount of phosphate rock produced globally, 95% is utilised as fertilizer. The Siilinjärvi mine, located in eastern Finland, is a major mine producing this material in the European Union. It has been active since 1979, when Kemira Oy began the mining for apatite as a source for phosphorus. Since 2007, the mine is operated by Yara International ASA with two open pits – the main Särkijärvi pit (Figure 3.1) and the satellite Saarinen pit – producing approximately 11 Mt of ore annually. The production is expected to continue until 2035. The Särkijärvi pit will be extended 2 km further north. Additionally, a new Jaakonlampi pit, located north of the Särkijärvi pit, is expected to start operating in 2021–2022. The extent of the deposit and new locations for open pits are currently being investigated to ensure the continuation of mining operations also after 2035. Therefore, different studies are being carried out in the area to better determine the extent of the ore body south of the Särkijärvi pit, the distribution of the present waste-rock diabase dikes, and to image major structures like fault and shear zones that may define the extent of possible sustainable mining.

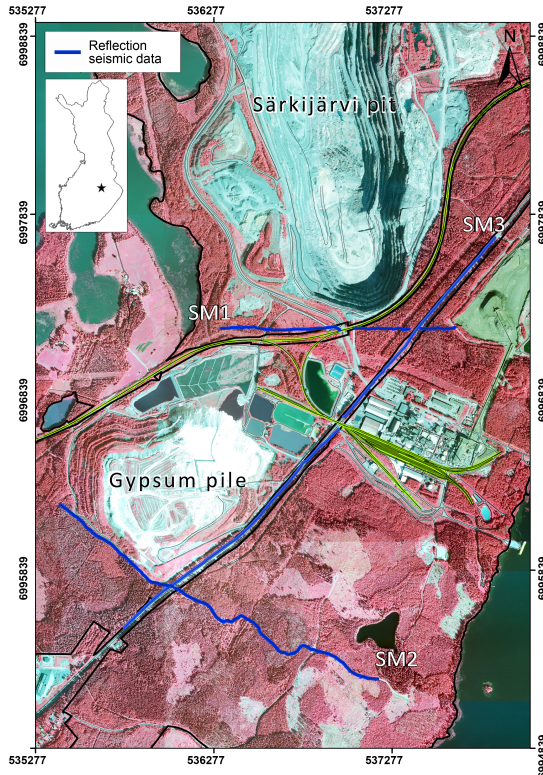


Figure 3.1: Location of the Siilinjärvi mine site and the reflection seismic data profiles SM1, SM2, and SM3 acquired in October 2018.

The use of seismic methods consolidated prominently in the mineral exploration industry in the past few decades due to their competency to gather superior-quality information at greater depths compared with other geophysical methods. These methods allow obtaining high-resolution earth models and images of the subsurface, which are essential for mine planning. In 2014, four seismic profiles were acquired in the Siilinjärvi mine with the main objective of imaging various types of dikes and shear zones in order to study the stability of the open-pit wall [2]. This study helped motivate a large seismic survey that was conducted in October 2018, southwards of the main Särkijärvi pit. As part of this survey, three active-source 2D reflection profiles were acquired (blue lines in Figure 3.1).

This work focuses on the 2D reflection profile SM1, located at the southern end of the Särkijärvi pit (Figure 3.1) with the aim to demonstrate how seismic methods and novel processing methodologies can be effectively utilised for mineral exploration and mine planning. We present a processing procedure for surface-wave suppression through the utilisation of SI. We apply SI to estimate surface waves and then subtract these estimated surface waves in an adaptive way from the original dataset. Interferometric surface-wave suppression has been utilised for hydrocarbon exploration [3, 4], in near-surface applications [5, 6] and in hard-rock for mineral exploration [7] (see also Chapter 2). Here, we further consolidate the application of this procedure in hard-rock mining environments, and we show its efficacy to enhance the processing of the data, obtaining an improved image of the subsurface and the target area.

3.2. SIILINJÄRVI PHOSPHATE MINE

The Siilinjärvi mine is a phosphate mine at the Archean Siilinjärvi carbonatite-glimmerite complex. It is situated in eastern Finland, approximately 28 km to the northeast of the city of Kuopio, and it comprises the largest open-pit mine in Finland. It constitutes the oldest carbonatite deposit that is currently being mined for phosphorous, and one of the oldest known on Earth at 2610 ± 4 Ma [8–11].

The Siilinjärvi complex is about 16 km long and up to 1.5 km wide (Figure 3.2), covering an area of 14.7 km^2 [12, 13]. A fenite margin encloses the ore body, which is intruded into the granite gneiss basement which extends some 100 km to the north from Siilinjärvi [12]. The rocks of the ore body are closely intermixed. They comprise principally glimmerite, carbonatite, and syenite, and vary from nearly pure glimmerites closer to the edges of the ore, to near pure carbonatites towards the central parts [13]. The main glimmerite-carbonatite intrusion within the Siilinjärvi complex is up to 900 m wide and occurs as a central tubular body that extends along the entire length of the complex. Younger diabase dikes of basaltic composition crosscut the entire Siilinjärvi complex, mainly showing a northwest-southeast or north-northwest-south-southeast orientation. Their widths range from centimetres to several meters [12]. Additionally, the carbonatite complex is intruded by a tonalite-diorite body in the southwestern part of the Särkijävi pit, resulting in an intricate structural setting [14].

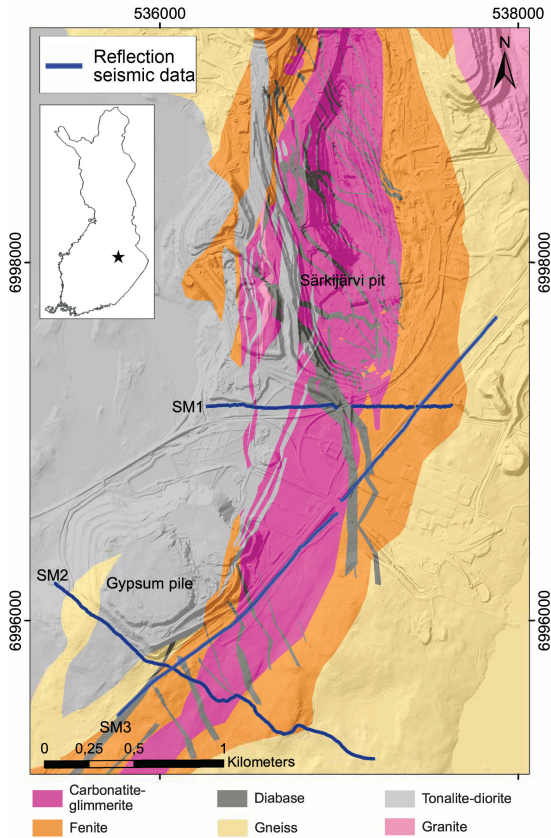


Figure 3.2: Geological map of the main Särkijärvi pit in the Siilinjärvi mine, eastern Finland, showing the location of the active-source reflection seismic profiles SM1, SM2, and SM3 (blue lines).

3.3. ADAPTIVE SUBTRACTION OF SURFACES WAVES THROUGH SEISMIC INTERFEROMETRY

SI is a method used to estimate the Green's function between two receivers. This involves the cross-correlation of responses at two receiver locations for each different source, and summation over the available sources [15], see also Chapters 1 and 2. Consequently, virtual sources are retrieved at positions where there are only receivers. An advantage of using this technique is that no knowledge of the subsurface-medium parameters is required. Moreover, the positions of the active sources do not have to be exactly known.

When SI is applied to active-source data by cross-correlating the seismic observations for a relatively straight-line survey, all the active sources contribute to the retrieval of the direct P- or S- and surface waves because all of them fall into the so-called stationary-phase region [16]. Therefore, surface waves will be dominant in the result retrieved by applying SI. This can be used for surface-wave estimation in order to further subtract these estimates from the original dataset. As explained above, this processing

procedure has been denoted as interferometric surface-wave suppression [3, 4, 6, 7, 17].

Note that, if there are receivers located at the source points, then a corresponding virtual source and surface-wave estimates can be retrieved for each active-source/receiver pair. For the particular case of profile SM1, receiver and shot positions are located close to each other. Therefore, we can assume that the retrieved surface waves are accurately represented for each active-source gather.

After the surface-wave estimation with SI, we perform adaptive subtraction by estimating a shaping filter that minimizes the difference between the field-recorded data and the surface waves retrieved by SI. This filter is then applied to the surface-wave estimates, and the thus shaped surface-wave estimates are subtracted from the field-recorded data, obtaining a result with suppressed surface waves.

3.4. DATA ACQUISITION AND PROCESSING

The active-source data were acquired within a period of two weeks during a fieldwork campaign in October 2018. The profile SM1, the focus of this study, is located south of the Särkijärvi pit, crossing several geological structures, i.e., the carbonatite-glimmerite mineralization, the fenite-surrounding body, and the diabase dikes and tonalite-diorite intrusions (Figure 3.2). The seismic profile is approximately east-west oriented and perpendicular to the ore body, which is nearly in the north-south direction. The total length of the profile is about 1.36 km. Gaps in the source coverage are present since the survey profile crosses a forest road and a railway line (Figure 3.2).

The data were acquired using 10-Hz geophones at each receiver location. On the western side of the seismic profile, 147 cabled receivers were used, plus 115 wireless recorders on the eastern side. The receiver spacing was set at 5 m. A gap of around 50 m was left between the end of the cabled-receivers section and the beginning of the wireless-receivers section (Figure 3.2) due to the railway line and the road present along the seismic profile. Explosives were used as the main sources, positioned in approximately 2-to-3-m-deep holes, with charges ranging from 125 g to 250 g. A 520-kg bobcat-mounted drop hammer was used in the areas close to the railway line and road, where explosives could not be used due to safety reasons. The sources were located every 20 m. The total number of source points was 69, with 59 explosive source locations and 10 drop-hammer source locations.

The data processing involved several steps (Table 3.1), focusing on further investigating the effectiveness of the methodology in hard-rock environments. As a first step, the geometry of the survey profile is set with a 2.5 m bin spacing, and a total of 544 CMPs, 4 m bin size along the line and 16 m bin size perpendicular to the line. After setting and applying the geometry, the data were subjected to refraction statics corrections and floating redatuming [18]. Prior to applying SI to retrieve surface-wave estimations, we apply a low-pass frequency filter at 35 Hz after studying the surface-wave content using the power spectra of the shot gathers. This is done in order to reject high frequencies that can contain reflection information that we do not want to be retrieved in the SI responses and, therefore, obtain more suitable surface-wave estimates. Following, we subject the filtered data to SI, and we use then this result as an input to adaptively subtract the retrieved surface waves from the original data without filtering.

Once we obtain the data with suppressed surface waves, we apply spherical diver-

| Step | Instruction |
|-----------------------|---|
| Pre-stack processing | |
| 1 | Set geometry |
| 2 | First-break picking |
| 3 | Refraction statics |
| 4 | Floating datum statics |
| 5 | SI to estimate the surface waves |
| 6 | Adaptive subtraction of the estimated surface waves |
| 7 | Spherical divergence correction |
| 8 | Trace muting |
| 9 | Air-wave and S-wave muting |
| 10 | AGC (500 ms time window) |
| 11 | Band-pass frequency filtering |
| 12 | Velocity analysis |
| 13 | NMO correction |
| 14 | Residual statics |
| 15 | CMP/ensemble stack |
| Post-stack processing | |
| 16 | Final datum statics |
| 17 | Kirchoff migration |
| 18 | F-X deconvolution |
| 19 | Semblance smoothing |
| 20 | Band-pass filtering |
| 21 | Trace balancing |
| 22 | AGC |
| 23 | Time-to-depth conversion |

Table 3.1: Summary of steps to suppress surface waves and process seismic reflection data to obtain the final stacked section.

gence correction, trace muting to remove highly noisy traces, and air- and S-waves muting for 330 m/s and 2700 m/s, respectively. Subsequently, we apply AGC with a 500 ms window for amplitude balancing, and band-pass frequency filtering between 50 Hz and 150 Hz to remove noises that remain in the data. After performing velocity analysis along the seismic profile, we apply NMO corrections using a 2D velocity model [18]. We then calculate and apply residual static corrections and stack the data.

The post-stack processing involved post-stack Kirchhoff migration using a simple 3-layer velocity model (5100 m/s for 0–500 ms, 5200 m/s for 500–2000 ms and 6000 m/s for >2000 ms). Following, in order to enhance reflective features, f-x deconvolution, semblance smoothing, additional filtering, trace balancing and AGC were applied to the stacked data. Finally, we use a constant velocity of 5500 m/s was used for time-to-depth conversion to present the data in the depth domain.

3.5. RESULTS

Figure 3.3a shows an example of a common-shot gather as recorded in the field. The high-amplitude energy from the surface waves (yellow arrows) is covering prominently useful reflections. Figure 3.3b shows the SI responses obtained for the same common-shot gather. These SI responses are subsequently used as surface-wave estimates for adaptive subtraction. We can see that the surface waves are dominant and well represented, and even some high-amplitude noises outside these areas are also retrieved.

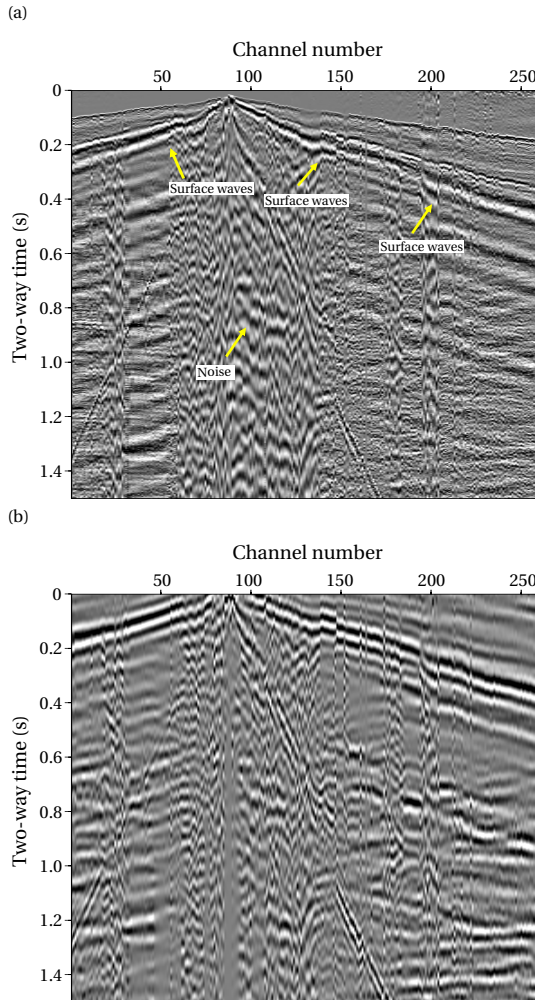


Figure 3.3: (a) An example of a common-shot gather from seismic line SM1 as used for adaptive subtraction of surface waves. (b) SI responses obtained for the common-shot gather in (a), used as surface-wave estimation for adaptive subtraction. AGC was applied for plotting. The yellow arrows point to surface-wave arrivals and other noises present in the common-shot gather.

Figure 3.4 and Figure 3.5 show the same common-source gather as in Figure 3.3 be-

fore and after SI surface-wave suppression, respectively. We apply band-pass filtering before plotting to remove some low-frequency noises that remain in the data in order to better compare the enhancements after this step. The high-amplitude energy from the surface waves (yellow arrows) is covering prominently useful reflections. After the application of interferometric surface-wave suppression, it can be seen clearly that the surface waves are attenuated. Some other coherent noises and energy from the air waves are also suppressed, as well as linear noises that appear to be surface-wave low-frequency ringing present throughout later times. Even though there is still some surface-wave energy remaining (yellow arrows in Figure 3.5), the reflections are now clearer and shallower arrivals are now revealed (red arrows in Figure 3.5).

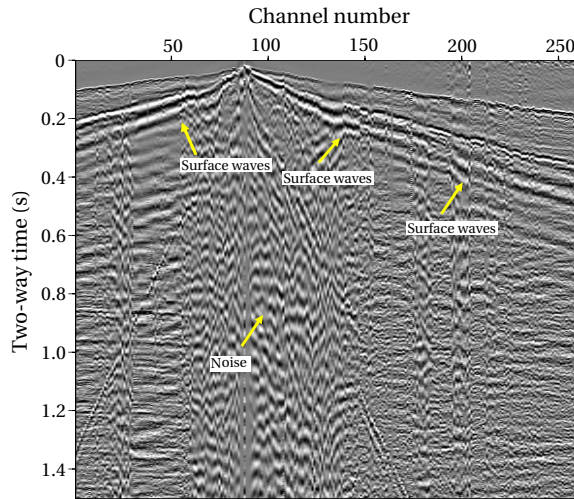


Figure 3.4: An example of a common-shot gather from profile SM1 and used for adaptive subtraction of surface waves. Band-pass filtering to remove some low-frequency noises and AGC were applied for plotting. The yellow arrows point to surface-wave arrivals and other noises present in the common-shot gather.

For comparison, Figure 3.6 shows the result after the application of f-k filtering for surface-wave suppression in the same common-shot gather. We can see that, in spite of also suppressing the surface waves, some surface-wave energy still remains (yellow arrows), as well as the air waves. Additionally, the low-frequency ringing from the surface-wave energy is still present (yellow arrows).

After applying NMO corrections, residual statics, and subsequent stacking, we apply the post-stack processing steps (Table 3.1), obtaining the migrated stacked sections for the differently processed datasets. Figure 3.7, Figure 3.8 and Figure 3.9 show the migrated seismic-reflection stacked sections for the dataset with the conventional processing applying only band-pass filtering for surface-wave suppression [18], for the dataset applying interferometric surface-wave suppression, and for the dataset applying f-k filtering for surface-wave suppression, respectively. Figure 3.10, Figure 3.11, and Figure 3.12 show their corresponding upper 1000 m close up, in order to more precisely analyse the near-surface features. This upper section is of main interest in this study area since it has the potential to be mined.

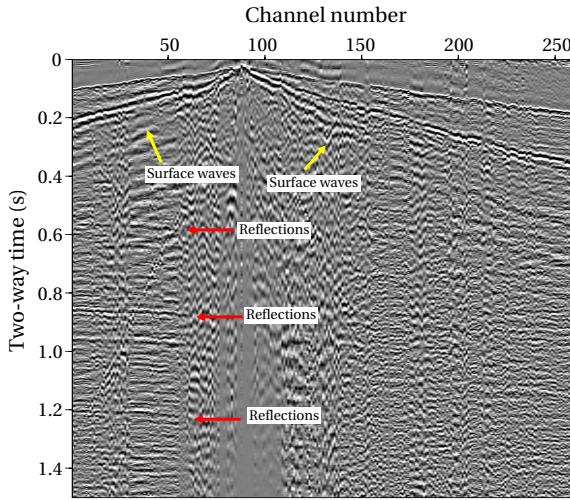


Figure 3.5: The same common-shot gather as in Figure 3.4, after interferometric surface-wave suppression. Band-pass filtering to remove some low-frequency noises and AGC were applied for plotting. The red arrows point to reflection arrivals, the yellow arrows point to surface-wave arrivals and other noises present in the common-shot gather.

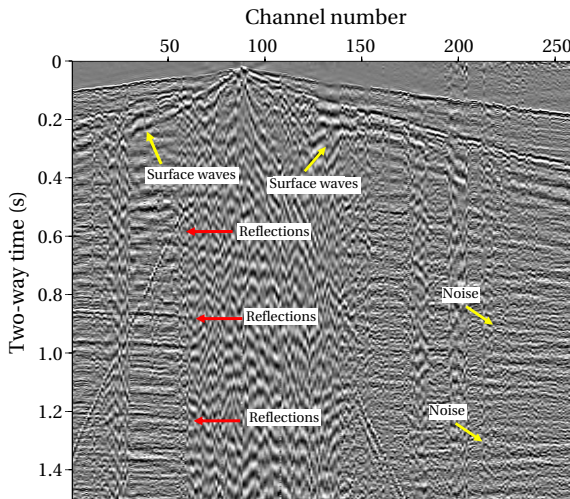


Figure 3.6: The same common-shot gather as in Figure 3.4, after the application of f-k filtering for surface-wave suppression. Band-pass filtering to remove some low-frequency noises and AGC were applied for plotting. The red arrows point to reflection arrivals, the yellow arrows point to surface-wave arrivals and other noises present in the common-shot gather.

In the result with f-k filtering for surface wave suppression (Figure 3.9 and Figure 3.12), we can see that the strongest shallow reflectors look less continuous and, overall, the images appear noisier (light blue arrows). The use of this type of filtering clearly

damages the frequency content and, therefore, the amplitudes in the final result. On the other hand, we can see that the result after interferometric surface-wave suppression (Figure 3.8 and Figure 3.11) gives sharper and more continuous reflectors for shallower and deeper structures (yellow and green arrows, respectively). We can see that the possible damage of the amplitudes due to the adaptive subtraction is much less in contrast with the result after f-k filtering. Comparing Figure 3.10 and Figure 3.11, we can see that some shallow structures are imaged differently around approximately 100 m and 500 m depth. The calculation of residual statics is a very important step in seismic imaging in hard-rock, near-mine environments, where data possess low signal-to-noise ratio, subsurface structures are very complex, and, therefore, reflections are not always continuous. Thus, this step will have a great impact on the processing flow and on the final stack. For this reason, it is important to first obtain a dataset after careful processing steps that provide the highest signal-to-noise ratio possible and cleaner reflections. Taking a look at the main reflectors, imaged below 500 m, and between 700 m and 900 m, we can see that they look sharper and more continuous for the result with interferometric surface-wave suppression. Additionally, the deeper reflectors (green arrows in Figure 3.7 and Figure 3.8) look more continuous for this result. Thus, given the improvements obtained throughout the entire depth of the image, we can safely assume that the methodology has helped obtain a more accurate residual-static calculation, giving more confidence to the structures that are imaged at shallower depths, which are harder to precisely recover due to the noise content and the complex reflectivity setting.

Similarly to the procedure followed in Chapter 2, in order to quantify the results obtained for the different methods applied for surface-wave suppression, we calculate the signal-to-noise ratio (S/N) for the obtained migrated stacked sections of the SM1 data using band-pass filtering (Figure 3.7), interferometric surface-wave suppression (Figure 3.8), and f-k filtering for surface-wave suppression (Figure 3.9). We calculate the S/N in two different sections of the images in order to compare the results for the shallow part of the image and the deeper part of the image. For both cases, we select two windows from the images, one window to represent the signal (where continuous reflectors are located), and a second window to represent the noise. We then compute the ratio of the summed squared magnitude of each window to obtain the S/N. For the deeper section, we choose the signal window between CMP 414 and CMP 468, and between 1300 m and 1450 m depth. The window corresponding to the noise is located between CMP 484 and CMP 538, and between 1270 m and 1420 m depth. For the image obtained using band-pass filtering, the S/N is 1.19. For the image obtained using f-k filtering for surface-wave suppression, the S/N is 0.98. For the image obtained using the data after interferometric surface-wave suppression, the S/N is 1.57. For the shallower section, we choose the signal window between CMP 117 and CMP 217, and between 380 m and 830 m depth, which corresponds to one of the main reflectors imaged in the shallower part of the section. The corresponding noise window is located between CMP 17 and CMP 117, and between 121 m and 1420 m depth. For the image obtained using band-pass filtering, the S/N is 1.16. For the image obtained using f-k filtering for surface-wave suppression, the S/N is 0.91. For the image obtained using the data after interferometric surface-wave suppression, the S/N is 1.38. These results help confirm and quantify the observations previously done about the higher noise content of the result for the data using f-k filter-

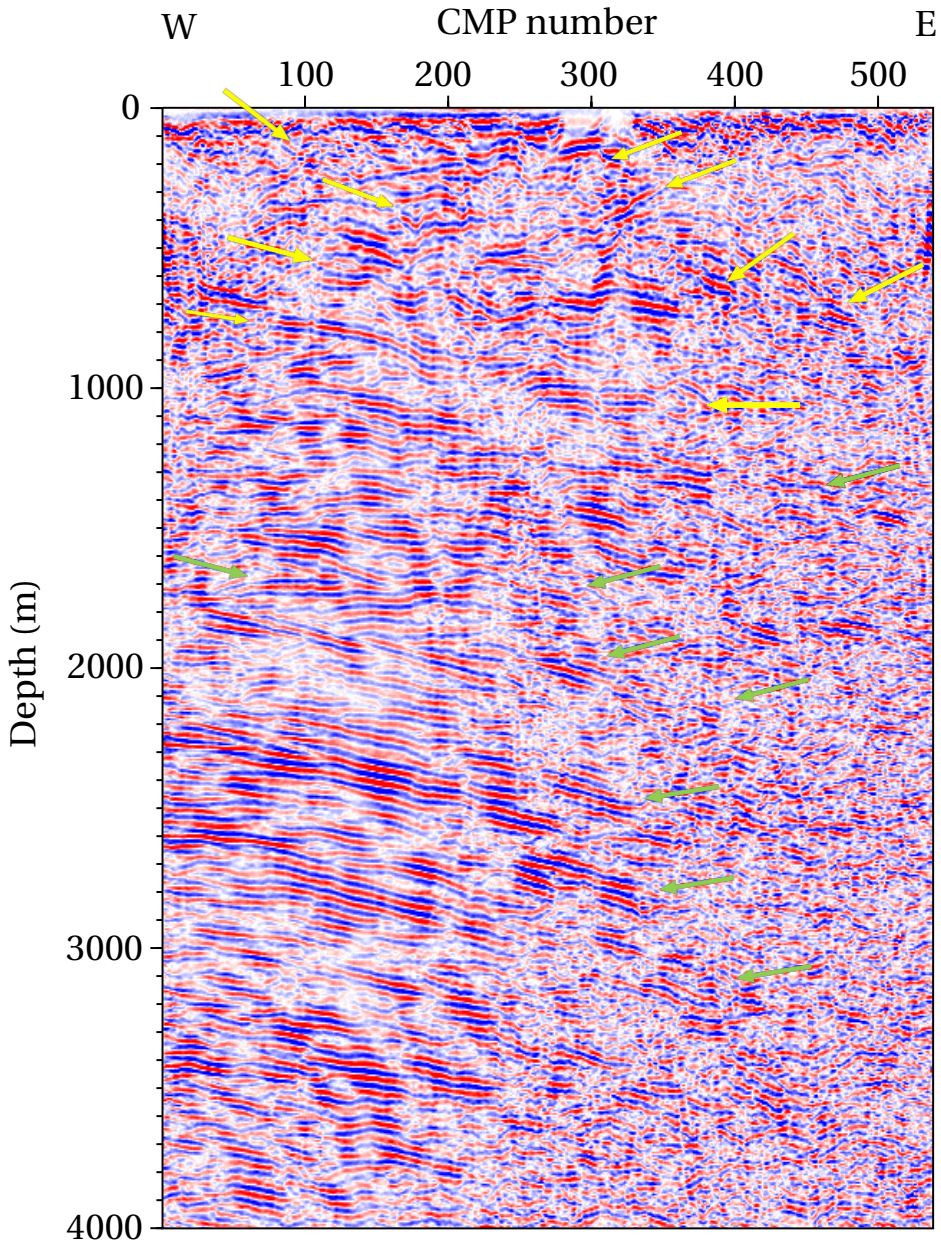


Figure 3.7: Migrated stacked section of the SM1 data using band-pass filtering for surface-wave suppression. The yellow and green arrows point at shallower and deeper structures, respectively.

ing for surface-wave suppression. We can see that utilising interferometric surface-wave suppression improves the S/N and enhances the continuity of the reflectors.

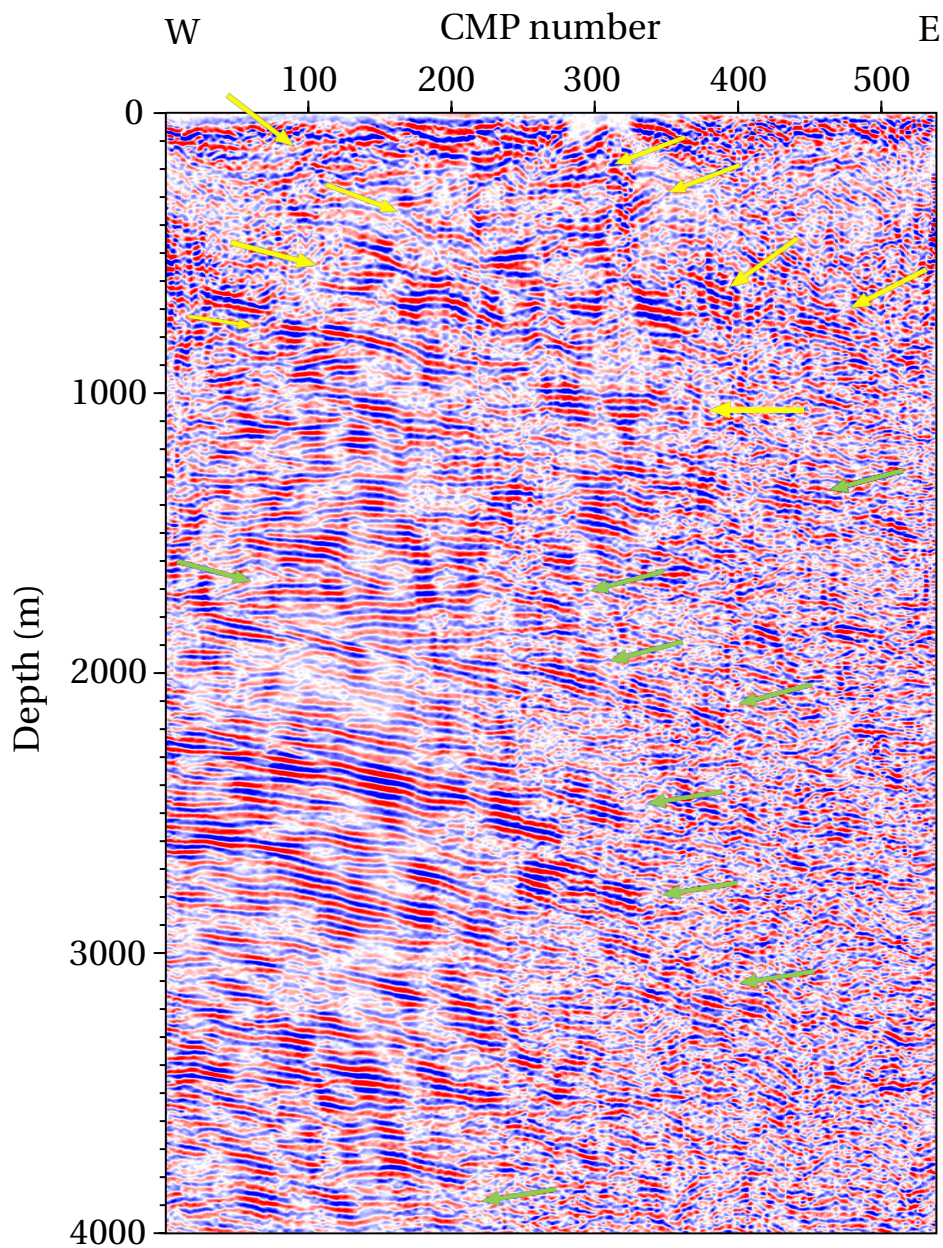


Figure 3.8: Migrated stacked section of the SM1 data after interferometric surface-wave suppression. The yellow and green arrows point at shallower and deeper structures, respectively, that now look sharper and more continuous throughout the entire length of the image.

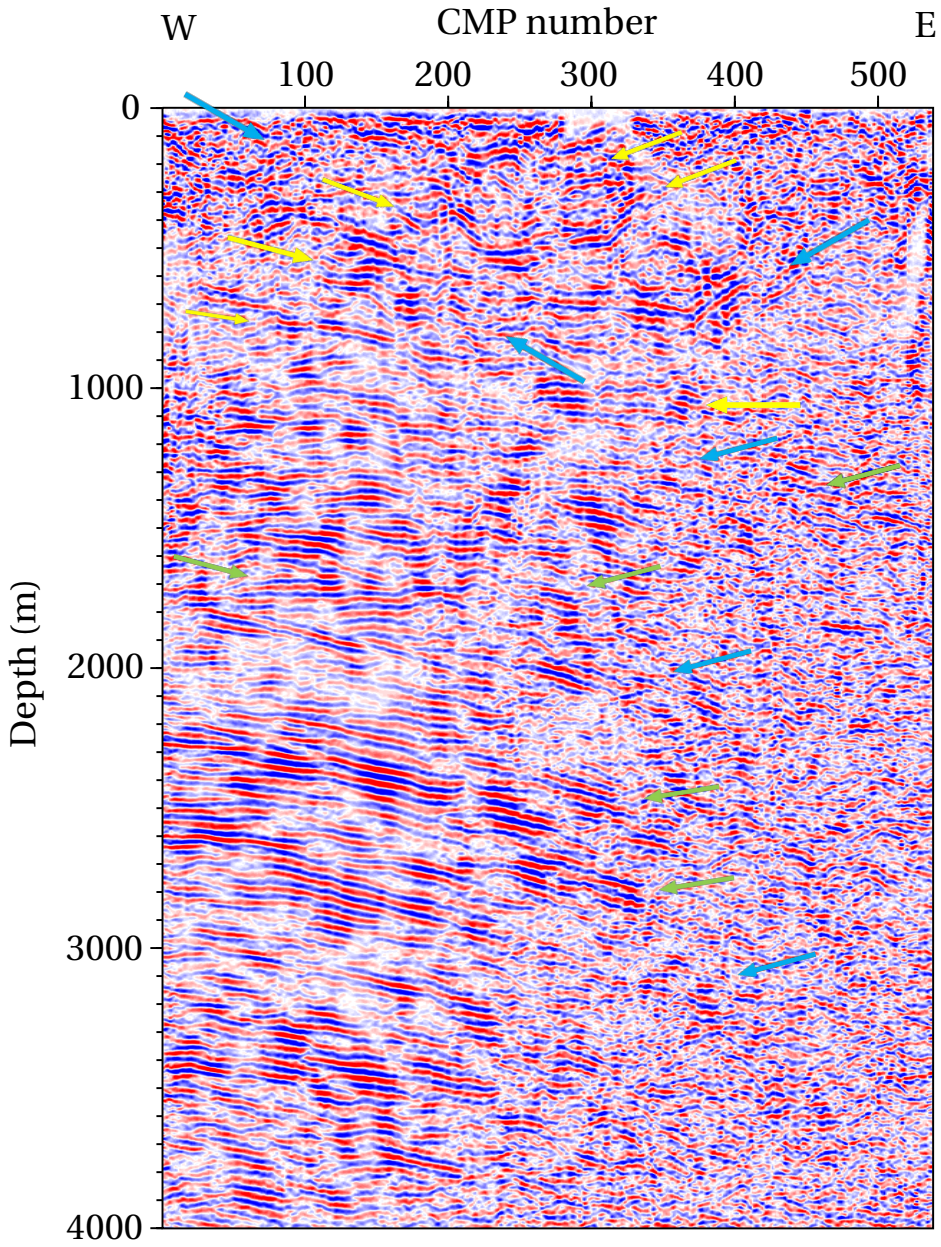


Figure 3.9: Migrated stacked section of SM1 data using f-k filtering for surface-wave suppression. The yellow and green arrows point at shallower and deeper structures, respectively. The light-blue arrows point at some strong reflectors that have lost continuity and other noises that appear stronger in this result.

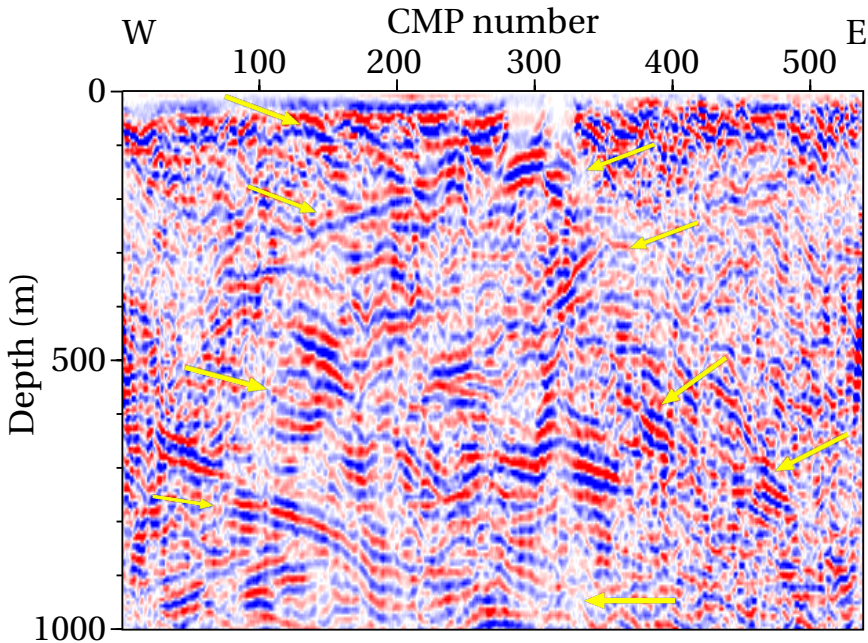


Figure 3.10: Migrated stacked section of the uppermost 1000 m of the SM1 data using band-pass filtering for surface-wave suppression. The yellow arrows point at shallower main structures.

Finally, [Figure 3.13](#) shows the geological interpretation of the result in [Figure 3.11](#). The reflectivity of the study area consists of a very complex reflection setting, comprised of several mostly sub-horizontal reflectors. From the known geology of the area ([Figure 3.2](#)), the interpreted carbonatite-glimmerite deposit can be delineated (pink area), a clear sub-vertical contact with the eastern fenite body can be interpreted from a clear reflectively contrast (orange area), as well as the western contact with the tonalite-diorite intrusion (grey area). Borehole data available for the area [2] show tonalite-diorite intermingled within the carbonatite-glimmerite body. These contacts could likely cause some of the reflection within the carbonatite-glimmerite body, but most of it is interpreted as diabase dyke contacts (grey lines). Lastly, the carbonatite-glimmerite deposit is interpreted to continue up to ~ 900 m depth, where it appears to be constrained by the uppermost of several sub-horizontal structures dipping towards the east (yellow arrow). Looking back to [Figure 3.10](#) and [Figure 3.11](#), although the conventional processing utilising band-pass filtering produces a good result, we can see that the result after interferometric surface-wave suppression provides a sharper boundary between the carbonatite-glimmerite body and the surrounding bodies.

3.6. CONCLUSIONS

We retrieved dominant surface waves by applying seismic interferometry and then adaptively subtracted the retrieved surface waves from data acquired for exploration at depth of the mineralization in the Siilinjärvi mine, eastern Finland. After careful processing

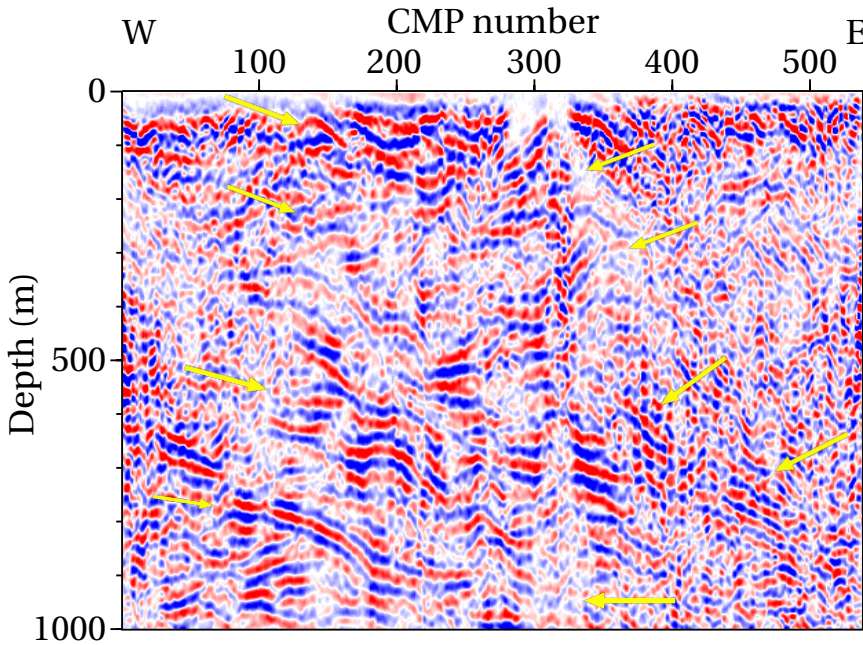


Figure 3.11: Migrated stacked section of the uppermost 1000 m of SM1 after interferometric adaptive subtraction of surface waves. The yellow arrows point at shallower structures that now look sharper and more continuous, also throughout the entire length of the image.

of these data, we obtained a migrated stacked section with enhanced image quality and also different features at earlier and later times.

Comparison with the migrated stacked sections of the data using band-pass filtering for surface-wave suppression and with f-k filtering for surface-wave suppression shows the efficacy of the methodology, which represents a powerful tool for denoising, helping improve the effectiveness of the subsequent processing steps and thus the final result, avoiding potential artefacts and achieving less amplitude damages that f-k filtering can cause. Our results show that utilising interferometric surface-wave suppression enhances the continuity and sharpness of the imaged reflectors, and improves the S/N.

The SI surface-wave suppression represents a fully data-driven methodology for surface-wave suppression that does not require previous knowledge of the subsurface. This study aims to illustrate the potential of seismic methods and novel processing methodologies in the exploration of deep mining targets, and further consolidates the application of the interferometric surface-wave suppression procedure in these hard-rock environments.

3.7. ACKNOWLEDGEMENTS

This study was carried out within the Smart Exploration project. Smart Exploration has received funding from the European Union's Horizon 2020 research and innovation programme under grant agreement No. 775971. We thank University of Helsinki, Uppsala

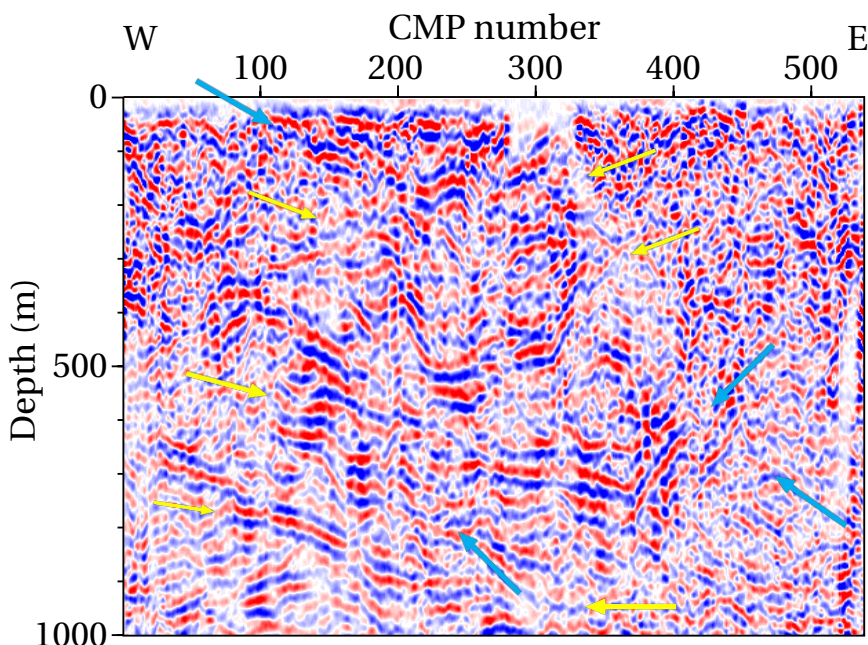


Figure 3.12: Migrated stacked section of the uppermost 1000 m of SM1 data using f-k filtering for surface-wave suppression. The yellow arrows point at shallower. The light-blue arrows point at some strong reflectors that have lost continuity and other noises that appear stronger in this result.

University and Yara Suomi Oy for providing access to the datasets and for collaborating with us through the Smart Exploration project. The seismic data were processed using Seismic Unix, ProMAX and software from the Delphi Consortium.

REFERENCES

- [1] *Communication from the commission to the European parliament, the council, the European economic and social committee and the committee of the regions on the 2017 list of Critical Raw materials for the EU*, Vol. COM(2017)490 (European Commission, 2017).
- [2] A. Malehmir, S. Heinonen, M. Dehghannejad, P. Heino, G. Maries, F. Karell, M. Suikkanen, and A. Salo, *Landstreamer seismics and physical property measurements in the Siilinjärvi open-pit apatite (phosphate) mine, central Finland*, *Geophysics* **82**, B29 (2017).
- [3] S. Dong, R. He, and G. T. Schuster, *Interferometric prediction and least squares subtraction of surface waves*, in *SEG Technical Program Expanded Abstracts 2006* (Society of Exploration Geophysicists, 2006).
- [4] D. F. Halliday, A. Curtis, P. Vermeer, C. Strobbia, A. Glushchenko, D.-J. van Manen,

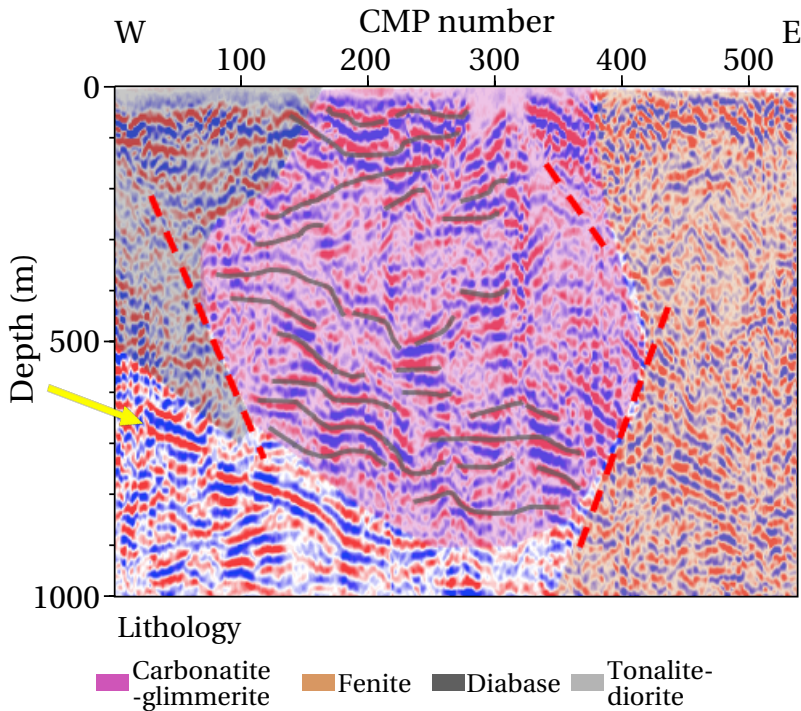


Figure 3.13: Geological interpretation of uppermost 1000 m of the migrated stacked section of SM1 after interferometric adaptive subtraction of surface waves. The interpreted carbonatite-glimmerite ore is indicated in pink. The grey lines suggest the diabase dyke and tonalite-diorite contacts within the body. The grey and orange areas indicate the interpreted tonalite-diorite intrusion and the fenite body, respectively. The red dashed lines represent possible fault zones. The yellow arrow points at the uppermost of several sub-horizontal structures dipping towards the east, that is interpreted to constrain the carbonatite-glimmerite deposit at depth.

and J. O. Robertsson, *Interferometric ground-roll removal: Attenuation of scattered surface waves in single-sensor data*, *Geophysics* **75**, SA15 (2010).

- [5] L. A. Konstantaki, R. Ghose, D. Draganov, G. Diaferia, and T. Heimovaara, *Characterization of a heterogeneous landfill using seismic and electrical resistivity data*, *Geophysics* **80**, EN13 (2015).
- [6] J. Liu, D. Draganov, and R. Ghose, *Seismic interferometry facilitating the imaging of shallow shear-wave reflections hidden beneath surface waves*, *Near Surface Geophysics* **16**, 372 (2018).
- [7] F. Balestrini, D. Draganov, A. Malehmir, P. Marsden, and R. Ghose, *Improved target illumination at Ludvika mines of Sweden through seismic-interferometric surface-wave suppression*, *Geophysical Prospecting* **68**, 200 (2019).
- [8] D. R. Zozulya, T. B. Bayanova, and P. N. Serov, *Age and isotopic geochemical characteristics of Archean carbonatites and alkaline rocks of the Baltic shield*, *Doklady Earth Sciences* **415**, 874 (2007).

- [9] A. S. Rukhlov and K. Bell, *Geochronology of carbonatites from the Canadian and Baltic Shields, and the Canadian Cordillera: clues to mantle evolution*, *Mineralogy and Petrology* **98**, 11 (2009).
- [10] M. Tichomirowa, M. Whitehouse, A. Gerdes, J. Götze, B. Schulz, and B. Belyatsky, *Different zircon recrystallization types in carbonatites caused by magma mixing: Evidence from U–Pb dating, trace element and isotope composition (Hf and O) of zircons from two Precambrian carbonatites from Fennoscandia*, *Chemical Geology* **353**, 173 (2013).
- [11] E. Heilimo, H. O’Brien, and P. Heino, *Constraints on the formation of the Archean Siilinjärvi carbonatite-glimmerite complex, Fennoscandian shield*, Goldschmidt Conference 2015, Abstracts. (2015).
- [12] K. Puustinen, *Geology of the siilinjärvi carbonatite complex, eastern finland*, Bulletin de la Commission géologique de Finlande **249**, 1 (1971).
- [13] H. O’Brien, E. Heilimo, and P. Heino, *The archean siilinjärvi carbonatite complex*, in *Mineral Deposits of Finland* (Elsevier, 2015) pp. 327–343.
- [14] H. B. Mattsson, K. Högdahl, M. Carlsson, and A. Malehmir, *The role of mafic dykes in the petrogenesis of the Archean Siilinjärvi carbonatite complex, east-central Finland*, *Lithos* **342-343**, 468 (2019).
- [15] K. Wapenaar and J. Fokkema, *Green’s function representations for seismic interferometry*, *Geophysics* **71**, SI33 (2006).
- [16] R. Snieder, *Extracting the Green’s function from the correlation of coda waves: A derivation based on stationary phase*, *Physical Review E* **69**, 046610 (2004).
- [17] L. Konstantaki, D. Draganov, R. Ghose, and T. Heimovaara, *Seismic interferometry as a tool for improved imaging of the heterogeneities in the body of a landfill*, *Journal of Applied Geophysics* **122**, 28 (2015).
- [18] V. Laakso, *Testing of reflection seismic, GPR and magnetic methods for mineral exploration and mine planning at the Siilinjärvi phosphate mine site in Finland*, Master’s thesis, University of Helsinki (2019).

4

ELECTROMAGNETIC- INTERFEROMETRIC DIRECT-WAVE SUPPRESSION FOR DETECTION OF SHALLOW BURIED TARGETS WITH GPR

One of the most common methodologies utilised for shallow geophysical and archaeological investigations is ground penetrating radar (GPR). GPR is a popular tool due to its non-invasiveness and capacity for real-time data analysis, widely used for the study of near-surface structures and the detection of buried targets. However, the direct wave propagating along the surface can completely cover the shallowest targets and, thus, needs to be suppressed. Electromagnetic interferometry (EMI) can be utilised to retrieve an estimate of the direct wave. Subsequently, this estimate can be adaptively subtracted from the field data to effectively eliminate the direct wave. We apply this methodology to a GPR dataset acquired at the Jewish Cemetery in Naaldwijk, The Netherlands, in August 2020. The main objective of the survey is to identify locations of possible old, buried tombstones. After applying the proposed methodology, our results show the direct wave is well suppressed. The earliest diffraction events that were covered by the direct arrival are visible after this step. The survey revealed anomalies where buried tombstones might be expected. This work serves to demonstrate the applicability of the GPR survey to detect shallow targets and the utilisation of EMI for direct-wave suppression in GPR data.

Part of this chapter was published as F. Balestrini, D. Draganov, D. Ngan-Tillard, and F. Hansen, *Electromagnetic-interferometric direct-wave suppression for detection of shallow buried targets with GPR*, in [NSG2021 27th European Meeting of Environmental and Engineering Geo-physics](#) (European Association of Geoscientists & Engineers, 2021).

Note that changes have been applied to make the text and figures consistent with this thesis.

4.1. INTRODUCTION

Ground penetrating radar (GPR) is commonly used for shallow geophysical and archaeological investigations since it is a non-invasive method and has the capacity for real-time data analysis with high spatial resolution [1]. The GPR methods usually consist of a transmitting and a receiving antenna on the surface, the transmitted electromagnetic pulses are reflected at different subsurface boundaries between objects that differ in their electric and magnetic properties. The received signals include, for instance, the direct-wave arrivals, which are the coupling signals between the transmitting and receiving antenna, and the reflected and diffracted waves from the underground boundaries.

The amplitude of the direct-wave arrival is much stronger than the reflected waves from the underground targets. Therefore, when the targets are buried near the surface, the earliest reflections or diffractions in the GPR data can completely overlap with the direct arrival, and this could thus obscure the detection of shallow features [2–4]. There exist several approaches that were proposed and developed for direct-waves suppression. The most commonly applied methods are based on curvelet transforms [3, 5–7], but also on shearlet transforms [2], wavelet operators [8], clutter modelling and subtraction [9, 10], f-k filters [11], singular-value decomposition [12, 13], and entropy [14]. However, these methodologies can involve strenuous steps, lack precision, or produce artefacts and damage the data.

The retrieval of new responses from cross-correlations of responses recorded at different receiver locations is commonly known as interferometry. These newly retrieved responses represent the measured wavefield between the receivers as if there were a source at one of the receiver locations. These are usually referred to as virtual sources. Firstly developed for seismic waves, interferometry has also been extended to electromagnetic wavefields, and thus used for GPR applications [15–17].

In this chapter, we extend the interferometric-suppression applications from seismic wavefields to electromagnetic wavefields and near-surface data. In August 2020, a GPR survey was carried out at the Jewish Cemetery in Naaldwijk, The Netherlands (Figure 4.1). The primary objective of the survey was to apply a non-invasive method to locate possible tombstones or pieces of tombstones laying under the ground surface of the cemetery, demonstrating also the applicability of the method to detect shallow features. These possible tombstones are expected not deeper than about a meter, but also covered by a few centimetres of soil. Thus, earlier GPR times are of great importance for the detection of events that could indicate possible locations of buried objects. We propose to use electromagnetic interferometry (EMI) to retrieve the direct wave and then adaptively subtract it from the acquired field data. This data-driven method allows obtaining a much cleaner image for the earliest times, permitting the identification of the shallowest anomalies in the subsurface. EMI has previously been proposed for GPR data [16, 17], but has not so far been used in combination with adaptive subtraction for the removal of the direct wave.



Figure 4.1: Google-map view of the Jewish cemetery in Naaldwijk, The Netherlands. The measurement area was divided into two parts, indicated by blue and orange transparent rectangles.

4.2. ELECTROMAGNETIC INTERFEROMETRY AND ADAPTIVE SUBTRACTION

Analogous to SI, EMI is a data-driven method that allows the retrieval of new electromagnetic responses from virtual sources through the cross-correlation of observations at two different receiver locations [17, 18]. For the case of active-source EMI, the cross-correlation is followed by the summation over all available sources. This allows obtaining the electromagnetic Green's function that represents the propagation between the two receivers as if there were a source at one of the receiver locations, which is usually called a virtual source.

Slob *et al.* [15] applied the theorems of the time-correlation and time-convolution types to Maxwell's equations over a volume \mathbb{D} with boundary $\partial\mathbb{D}$, and derived exact Green's function representations for electromagnetic fields and waves in media with losses. Assuming that the dissipation is negligible, electric source currents can be described as point sources inside this volume, the medium properties near the boundary $\partial\mathbb{D}$ are locally smoothly varying, the far-field approximation applies, and rays that leave the surface perpendicularly give the major contribution to the final result, the exact representation simplify to a representation that can be used in practical applications as:

$$2\Re\{\hat{G}_{kr}^{Ee}(\mathbf{x}_A, \mathbf{x}_B, \omega)\} \approx -\frac{2}{\mu V_P} \oint_{\mathbf{x} \in \partial\mathbb{D}} \hat{G}_{rj}^{Ee}(\mathbf{x}_B, \mathbf{x}_n, \omega) \{\hat{G}_{kj}^{Ee}(\mathbf{x}_A, \mathbf{x}_n, \omega)\}^* d^2\mathbf{x}_n, \quad (4.1)$$

when both $\mathbf{x}_A \in \mathbb{D}$ and $\mathbf{x}_B \in \mathbb{D}$. $\hat{G}_{kr}^{Ee}(\mathbf{x}_A, \mathbf{x}_B, \omega)$ represents the Green's functions in the frequency domain. The two indices in the superscript indicate that the received signal is an electric field E generated by an electric current e (since electric-field receivers and sources are normally used). The first subscript indicates the direction of the electric-field component, whilst the second subscript indicates the component of the electric-current source vector. Note the summation over repeated subscripts (i.e., Einstein's summation convention) is assumed. The first and second arguments of \hat{G} represent the receiver and source positions, respectively. As in Chapter 2, on the right-hand side, \mathbf{x}_A and \mathbf{x}_B are two receiver positions, while \mathbf{x}_n represents the different source locations. μ and $V_P = (\varepsilon\mu)^{-1/2}$

stand for the magnetic permeability and the propagation velocity of acoustic waves in the medium of the actual sources, respectively, with ε being the electric permittivity. The integrands in the right-hand side of Equation 4.1 are electric fields generated by impulsive sources in the j -direction, and located at \mathbf{x}_n on the boundary $\partial\mathbb{D}$. The k -component is recorded at \mathbf{x}_A , and the r -component at \mathbf{x}_B . The left-hand side of Equation 4.1 represents the real part of the k -component of the electric field recorded at \mathbf{x}_A , generated by the r -component of an impulsive electric source located at the position of the recorder \mathbf{x}_B . Thus, Equation 4.1 shows that the cross-correlation of the two recordings in the time domain and subsequent summation over all the three perpendicular source directions at all locations on the boundary retrieves the electric field Green's function recorded at \mathbf{x}_B that would be generated by an impulsive source at location \mathbf{x}_A [15, 19].

The \sim sign arises from considering the boundary $\partial\mathbb{D}$ to be a sphere with a large enough radius so that the far-field conditions apply [20]. Additionally, the integration over the boundary $\partial\mathbb{D}$ means that sources surrounding the virtual source position are required. In reality, we do not have such source distribution. A limited source distribution creates spurious events. Waves that should cancel when summed over all sources will now not show complete destructive interference, and this is expressed as non-physical events in the interferometric result [15, 19].

For transient sources, the source signatures are incorporated defining the electric wavefield observed at the receiver locations \mathbf{x}_A and \mathbf{x}_B as [15, 19]

$$\hat{u}_{kj}^{obs}(\mathbf{x}_A, \mathbf{x}_n, \omega) = \hat{G}_{kj}^{Ee}(\mathbf{x}_A, \mathbf{x}_n, \omega) s^{(j)}(\mathbf{x}_n, \omega), \quad (4.2)$$

$$\hat{u}_{rj}^{obs}(\mathbf{x}_A, \mathbf{x}_n, \omega) = \hat{G}_{rj}^{Ee}(\mathbf{x}_B, \mathbf{x}_n, \omega) s^{(j)}(\mathbf{x}_n, \omega). \quad (4.3)$$

$s^{(j)}(\mathbf{x}_n, \omega)$ is the source frequency spectrum in the j -direction at position \mathbf{x}_n , which can be different for each one of the three perpendicular directions and each source position. The power spectrum of the sources is then defined as

$$\hat{S}^{(j)}(\mathbf{x}_n, \omega) = \{\hat{s}^{(j)}(\mathbf{x}_n, \omega)\}^* \hat{s}^{(j)}(\mathbf{x}_n, \omega). \quad (4.4)$$

A shaping filter $\hat{F}^{(j)}(\mathbf{x}_n, \omega)$ can be introduced as [15],

$$\hat{F}^{(j)}(\mathbf{x}_n, \omega) = \frac{Y \hat{S}_0(\omega)}{\hat{S}^{(j)}(\mathbf{x}_n, \omega)}, \quad (4.5)$$

where $Y = 1/(\mu c)$ is the plane-wave admittance of the embedding, and \hat{S}_0 is a desired source power spectrum. Using Equation 4.2 to Equation 4.5 in Equation 4.1, we obtain [15]

$$\hat{S}_0(\omega) \Re\{\hat{G}_{kr}^{Ee}(\mathbf{x}_B, \mathbf{x}_A, \omega)\} \approx - \oint_{\mathbf{x} \in \partial\mathbb{D}} \hat{F}^{(j)}(\mathbf{x}_n, \omega) \hat{u}_{rj}^{obs}(\mathbf{x}_B, \mathbf{x}_n, \omega) \{\hat{u}_{kj}^{obs}(\mathbf{x}_A, \mathbf{x}_n, \omega)\}^* d^2\mathbf{x}, \quad (4.6)$$

with $\mathbf{x}_A \in \mathbb{D}$ and $\mathbf{x}_B \in \mathbb{D}$. Analogous to Equation 2.1, Equation 4.6 indicates that we can obtain the electric field response due to an electric virtual source at \mathbf{x}_B recorded at \mathbf{x}_A from the cross-correlations in the time-domain of the electric field recordings at both \mathbf{x}_A

and \mathbf{x}_B due to electric point sources at \mathbf{x}_n along the boundary $\partial\mathbb{D}$ and summing over all these source contributions.

For a conventional GPR survey, sources and receivers are placed at the surface, so they all contribute to the retrieval of the direct wave since they all fall in the so-called stationary-phase region [21]. The estimated response retrieved by EMI will thus be dominated by the direct wave since it has the highest energy in the recordings. This fact can be used to our advantage to use the retrieved direct wave as a direct-wave estimate to adaptively subtract it from the original full-field responses [22–24]. Similar to the applications in Chapters 2 and 3, when adaptive subtraction is performed, a shaping filter that minimises the difference between the original field-recorded direct wave and the direct wave retrieved by EMI is estimated using a least-squares fit [22–24]. This filter compensates for the amplitude, phase, and frequency distortions in the predicted model. Here, we apply a regularised nonstationary regression technique that allows the matching filter become smoothly nonstationary without the need to break the input data into local windows [25, 26].

4.3. DATA ACQUISITION AND PROCESSING

For ease of recording, the investigated area was divided in two parts, represented by the blue and orange rectangles in Figure 4.1. The measurements were performed along parallel lines in fixed common-offset setup with the aim to obtain 3-dimensional information of the subsurface. The transmitting antenna of the GPR was sending a pulse signal with a centre frequency of 500 MHz, the receiver antenna had a recording sampling of 0.2 ns. In the bigger (blue) area, the line measurements started at $X = 0$ m, and were performed parallel to the Y -axis. In the smaller (orange) area, the line measurements started at $Y = 0$ m, and were performed parallel to the X -axis. The distance between neighbouring lines was 0.25 m. The measurements along each line were taken every 0.02 m. The length of the lines depended on the surface obstacles, with an average of ~ 25 m length for the bigger area and of ~ 12 m length for the smaller area.

Additionally, two multiple-offset (common-source) GPR lines were collected along the Y -axis in $X = 0$ m for velocity analysis and direct-wave retrieval through EMI and consecutive adaptive subtraction. The first source position was at $Y = 2.5$ m. The first receiver point was 0.23 m from the source along the Y -axis. This distance was equal to the fixed offset distance between the source and receiver antenna during the survey. The following receiver positions had a step of 0.05 m. The second source position was located at $Y = 2.73$ m. The first receiver point was 0.25 m from the source along the Y -axis. The following receiver positions had a step of 0.05 m.

Prior to processing the data, we apply EMI to the two multiple-offset lines. As output, we obtain a trace that represents an estimate of the direct arrival. Even though the direct arrival is dominant, this estimate also contains events from the cross-correlation of different reflection arrivals. Therefore, we use a taper to isolate the retrieved direct arrival. Since the area of study is small and, upon visual inspection, the top soil appears relatively homogeneous, we can safely assume that this is a good representation for the entire dataset.

Following, we apply standard processing steps to the common-offset data. The performed steps involve dewow to remove the low-frequency component that causes a

direct-current (DC) drift of the data [4], maximum-phase correction, and start-time correction to remove the time delay before the first arrival [1]. Then, we use the previous result obtained by EMI to adaptively subtract the retrieved direct-wave estimate from the common-offset data. Finally, we apply AGC with a window length of 10 ns for amplitude balancing, and bandpass filtering between 150 MHz and 850 MHz.

4.4. RESULTS

Figure 4.2a and Figure 4.2b show the two multiple-offset radagrams recorded along the Y-axis. A clear first arrival corresponding to the direct wave is observed. Additionally, we can see hyperbolic events arriving at later times, corresponding to waves reflected from subsurface heterogeneities. The blue trace in Figure 4.2c represents the trace obtained as a direct-wave estimate after applying EMI to the two multiple-offset lines. For comparison, Figure 4.2c shows the first trace from the first multiple-offset line in red.

Figure 4.3a and Figure 4.4a show two examples of time sections or radagrams measured with GPR in the bigger part (blue rectangle in Figure 4.1) at $X = 4.25$ m and at $X = 5$ m, respectively, after applying dewow, maximum-phase correction, start-time correction, AGC, and bandpass filtering. Both sections exhibit various diffraction events, but also clear horizontal events along their complete length just below time 0 ns. This is the direct wave propagating from the source to the receiver antenna along the surface, and that we want to suppress. Additionally, a sub-horizontal event is present below 20 ns in both lines, and it is observed throughout all the lines in both the bigger and the smaller surveyed areas. This event represents a change in the subsurface soil types. A transition from an upper aeolian sand, or sand and clayey layer, to clayey sediments is observed in nearby boreholes between 1.5 m and 2 m depth [27]. Thus, the sub-horizontal event at 22 ns (~ 0.88 m, assuming a propagation velocity of the electromagnetic waves of 0.08 m/ns) could still correspond to this transition.

Figure 4.3b and Figure 4.4b show the results after EMI direct-wave suppression using the direct wave estimated through EMI (Figure 4.2c), applied to the time sections in Figure 4.3a and Figure 4.4a, respectively. We can see that the direct wave is well suppressed and now the first nanoseconds of the time sections are much clearer and the earliest diffraction events that were before obscured by the direct wave, are visible (red and magenta dashed ellipses).

To compare these results with commonly applied methodologies in GPR processing, we apply background removal to the same examples shown in Figure 4.3a and Figure 4.4a. This methodology comprises the most classic and simplest technique for direct-wave suppression and background-noise attenuation. Being very easy to apply, it consists of removing the horizontal bands found in the radagrams. Most popular filter processes included in commercial processing software comprise calculating this average pulse across the section and then subtracting the average pulse from each individual trace [1]. The average pulse is calculated with a given window length with a specified number of traces. A short window will suppress all horizontal and sub-horizontal events, but can heavily damage the signal. Contrarily, a window with a relatively large number of traces will fail to suppress the direct wave, since this average pulse will not represent this event correctly. We perform several tests with different window lengths in order to find an optimal number of traces so that the direct wave is still suppressed, while trying

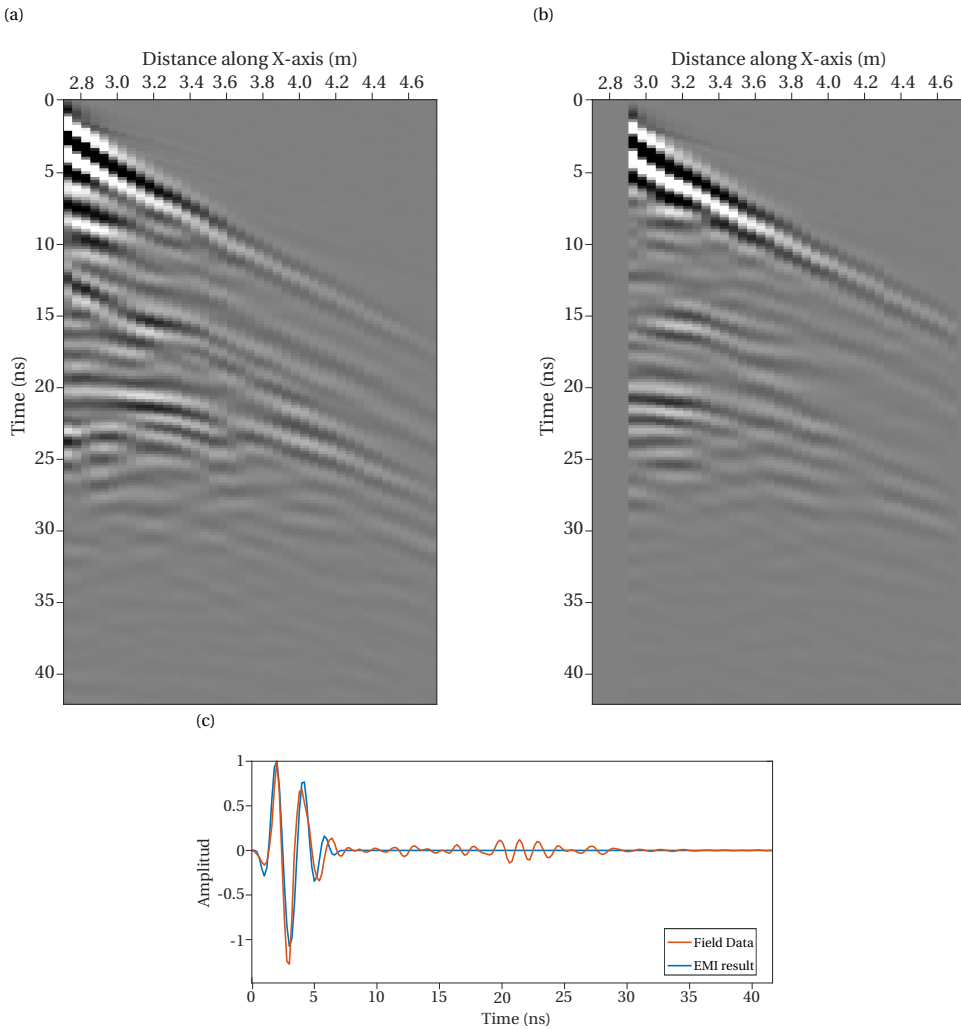


Figure 4.2: (a) Multiple-offset GPR data collected along line $X = 0$ m. The first source position was at $Y = 2.5$ m. (b) Multiple-offset GPR data collected along line $X = 0$ m. The first source position was at $Y = 2.73$ m. (c) In blue, trace obtained as a direct-wave estimate after applying EMI; in red, first trace from (a) for comparison.

to preserve the near-horizontal reflection signal, e.g., at around 20 ns. [Figure 4.3c](#) and [Figure 4.4c](#) show the results utilising background removal with a window length of 20 traces to the same radagrams shown in [Figure 4.3a](#) and [Figure 4.4a](#), respectively. We can observe that after this step, the direct-wave arrival is also well suppressed. Additionally, background noises are also successfully removed. However, a great disadvantage of this method is that it strongly removes horizontal linear features parallel to the acquisition line. This can be observed in the sub-horizontal event below 20 ns, that for the result applying background removal has been almost completely suppressed. Moreover, we

can observe that this methodology causes severe damage in the shape of the hyperbolic events which can lead to incorrect time-mapping of the reflected targets.

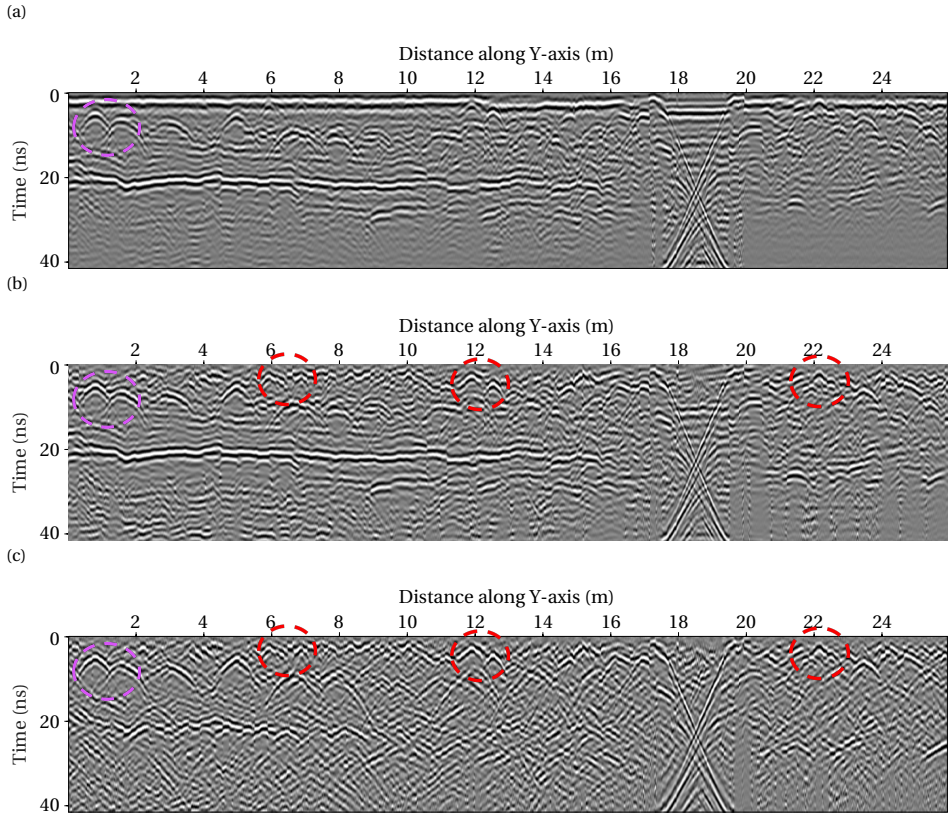


Figure 4.3: (a) Example of a time section measured with GPR in the bigger part (blue rectangle in Figure 4.1) at $X = 4.25$ m. (b) Result from (a) after application of EMI direct-wave suppression. (c) Result from (a) after application of background removal with 20 traces. The red and magenta dashed ellipses indicate diffraction events that were obscured by the direct wave and now are visible and clearer after direct-wave suppression.

After the applied processing steps, we analyse time slices for a preliminary interpretation of the shallowest part of this dataset. The time slices in Figure 4.5, Figure 4.6 and Figure 4.7 correspond to depths of ~ 0.14 m, ~ 0.17 m, and ~ 0.2 m, respectively (assuming a propagation velocity of 0.08 m/ns). Figure 4.5a, Figure 4.6a and Figure 4.7a show the time slices from the data as measured in the field. Figure 4.5b, Figure 4.6b and Figure 4.7b show the respective time slices after EMI direct-wave suppression. We can see that after this data-driven processing, different features in the image look much sharper, the low-frequency amplitudes from the direct wave are removed and, overall, the amplitudes in the image are more balanced. The time slices exhibit curved tubular lines (yellow arrows). These are interpreted as tree roots. The same figures also exhibit rectangles elongated in the direction of the Y-axis (green arrows). These represent subsurface structures under tombstones at the surface. Figure 4.5c, Figure 4.6c and Figure 4.7c show

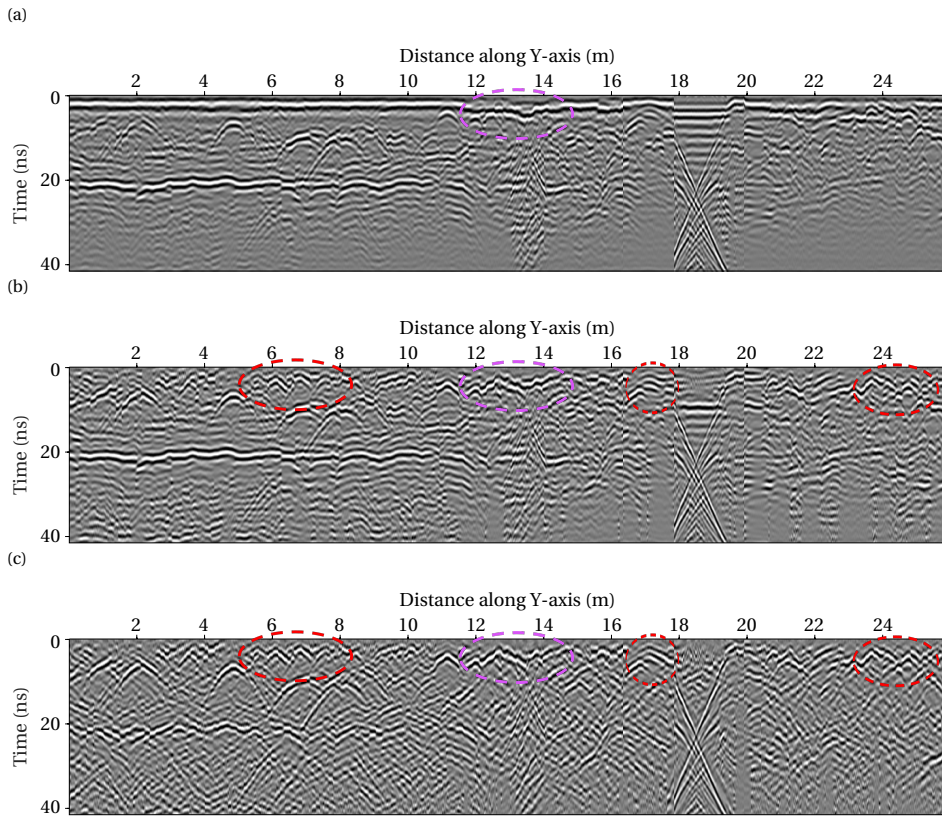


Figure 4.4: (a) Example of a time section measured with GPR in the bigger part (blue rectangle in Figure 4.1) at $X = 5$ m. (b) Result from (a) after application of EMI direct-wave suppression. (c) Result from (a) after application of background removal with 20 traces. The red and magenta dashed ellipses indicate diffraction events that were obscured by the direct wave and now are visible and clearer after direct-wave suppression.

the respective time slices utilising background removal. We can see that after applying this step, the low-frequency energy is removed as well, and root patterns appear well defined. This methodology also effectively removes background noises. Nevertheless, comparing these results with the data as measured in the field and the result after EMI direct-wave suppression, the events that represent structures under the tombstones at the surface are not noticeable, and other events, in particular on the left part of the images, appear less clear.

The magenta dashed ellipses highlight anomalies in the time slices, which did not have any visible tombstone at the surface, and are potentially of interest. In particular, the anomaly highlighted on the left half of the time slices ($X \sim 4$ m, $Y \sim 1$ m) is appreciable for all the obtained results for the deeper time slices (Figure 4.6 and Figure 4.7). Nevertheless, it is already noticeable for the shallower time slice (Figure 4.5) in the result utilising EMI direct-wave suppression. Moreover, throughout lower depths, it is more clearly defined after this processing step (Figure 4.6 and Figure 4.7). Taking a look at the

radagrams in [Figure 4.3](#), we can see that this event might correspond to the hyperbolic event highlighted by the magenta dashed ellipse. This event arrives just below the direct arrival. This step allows clearing the first nanoseconds that are still overlapped with the direct arrival.

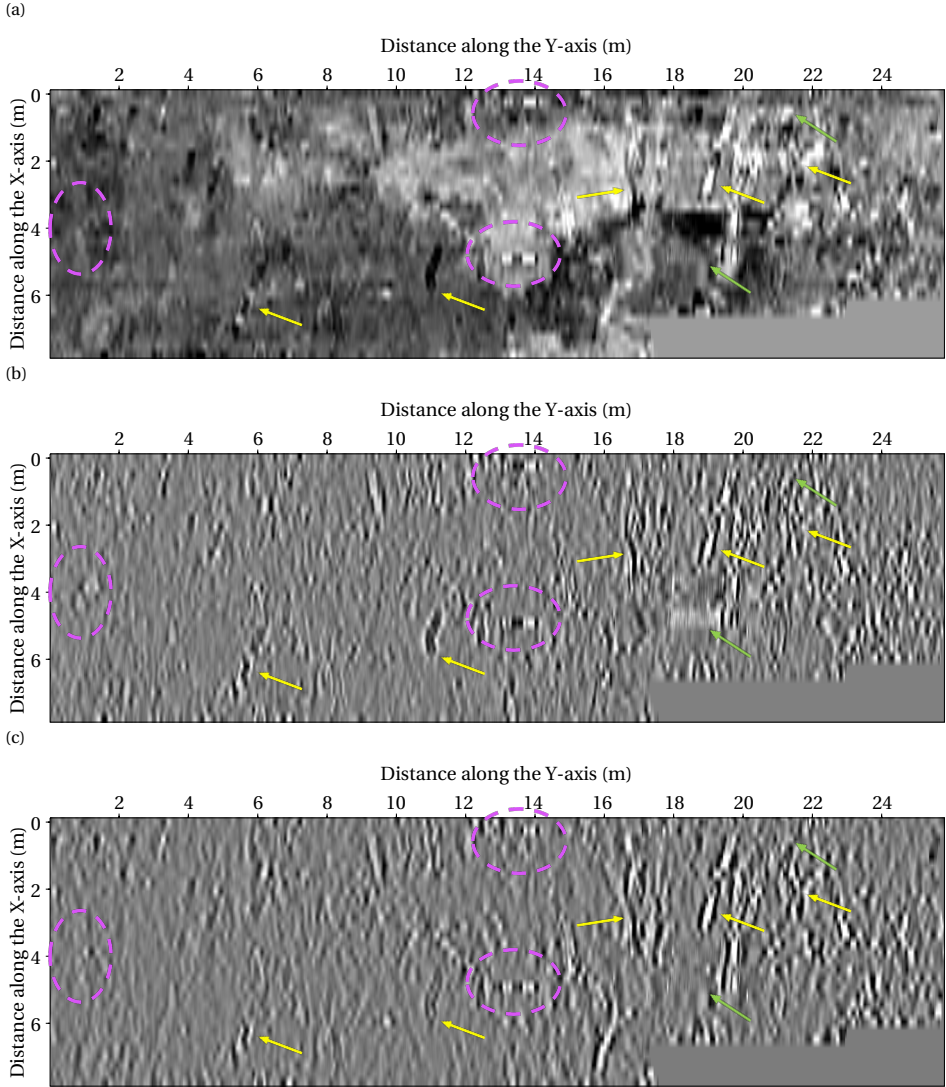


Figure 4.5: (a) Time slice measured with GPR in the bigger part (blue rectangle in [Figure 4.1](#)) at ~ 0.14 m depth. (b) Result from (a) after application of EMI direct-wave suppression. (c) Result from (a) after application of background removal with 20 traces. The yellow arrows indicate curved tubular lines that are interpreted as tree roots. The magenta dashed ellipses highlight anomalies that did not have any visible tombstone at the surface, and are potentially of interest.

The anomalies highlighted by the magenta dashed ellipses in the right half of the

time slices, both located at $Y \sim 13.5$ m, have a similar rectangular signature to those generated by the structures under the tombstones at the surface. We can see the signature of one of these anomalies at $X \sim 5$ m in the time section (magenta dashed ellipse in Figure 4.4), which appears to be also similar in later times to the one generated by the structures under the tombstones at the surface (between $Y \sim 18$ m and $Y \sim 20$ m).

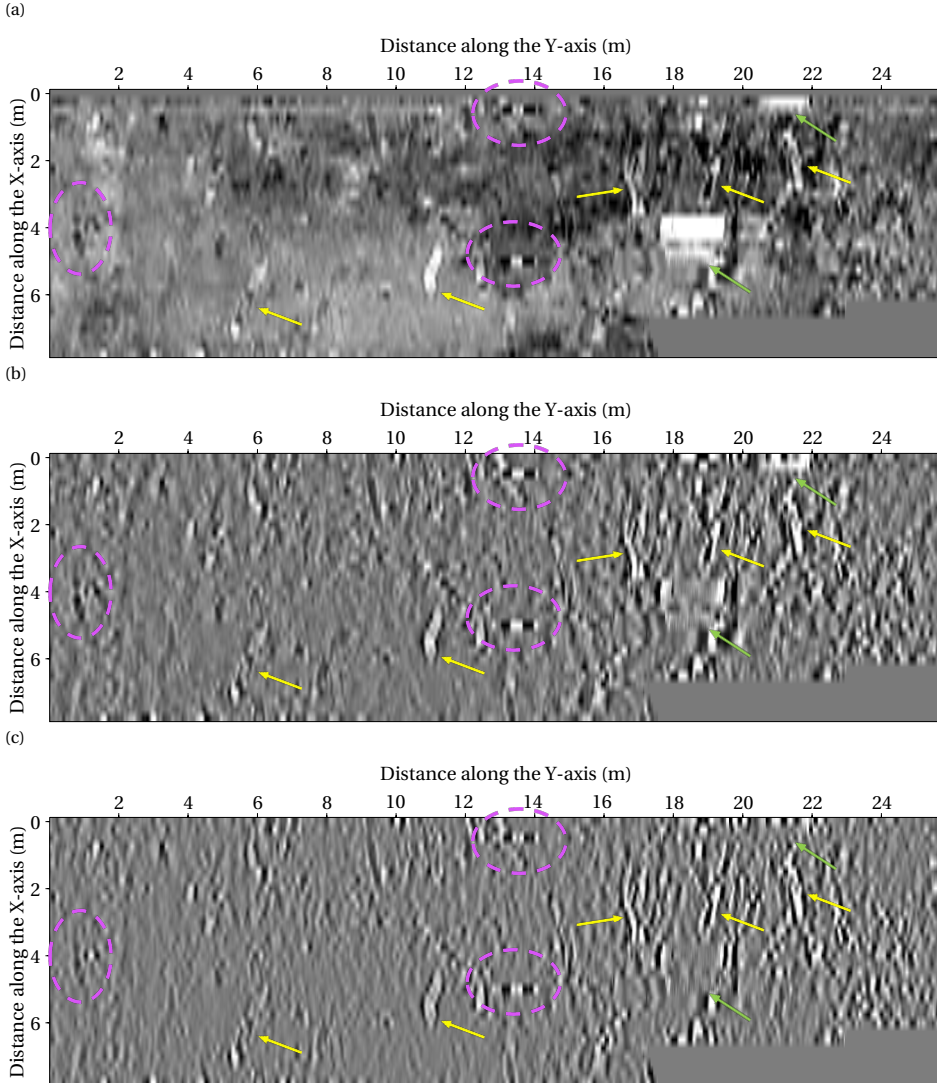


Figure 4.6: As in Figure 4.5, but for depth of ~ 0.17 m.

Subsequent inspection of the study area confirms the presence of buried objects at the three identified locations. However, the nature of these objects remains unclear due to restrictions on excavating the area at the present moment.

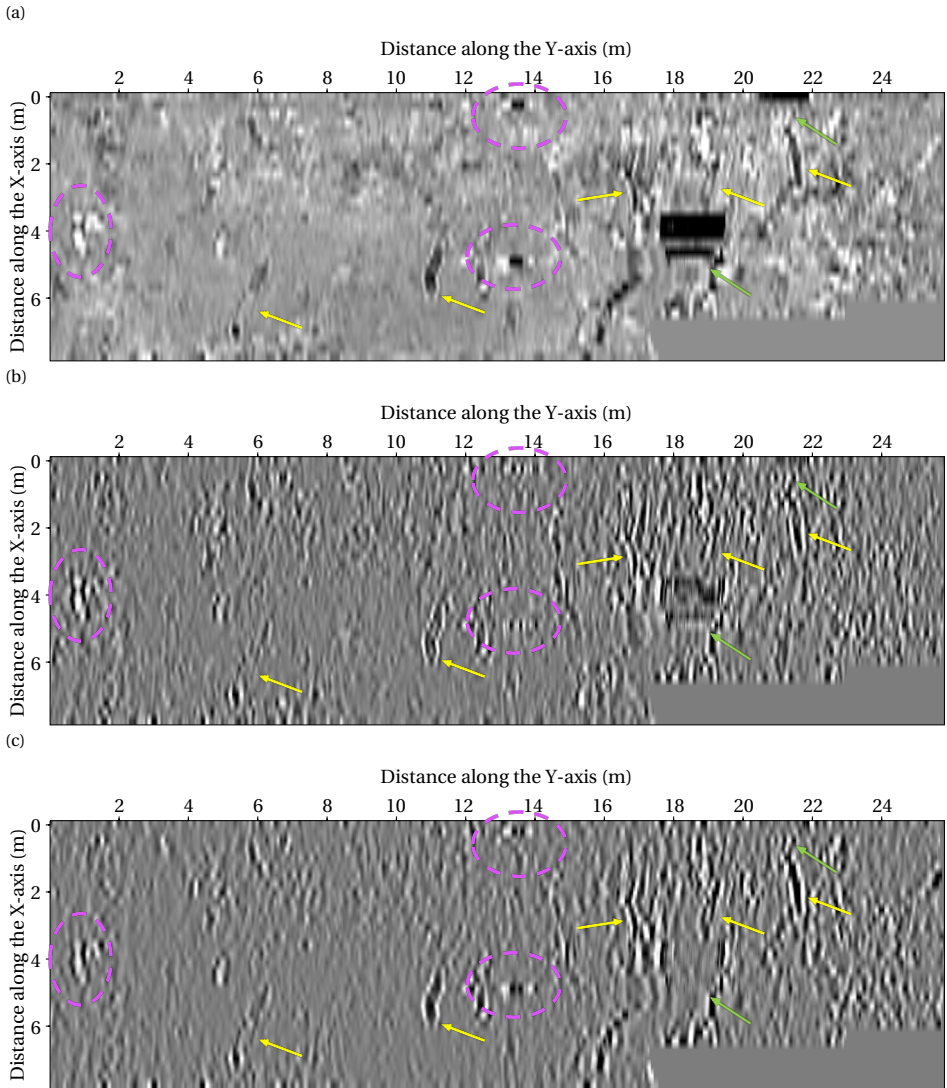


Figure 4.7: As in Figure 4.5, but for depth of ~ 0.20 m.

4.5. CONCLUSIONS

The flat and sandy nature of the graveyard allowed the acquisition of GPR signals of good quality and sufficient signal penetration to reach the shallow targets of the survey. We apply electromagnetic interferometry (EMI) for retrieval of the direct wave in order to adaptively subtract it from the field dataset. We showed that after this processing step, the direct arrival is well suppressed, the earliest part of the data looks much clearer and the shallowest events in the time slices can now be appreciated. This is an

effective data-driven method that does not require any previous knowledge of the subsurface for its application. Additionally, it does not require extra data acquisition in the field since multi-offset data are commonly acquired for velocity analysis. We also applied the classic methodology of background removal for direct-wave suppression. We showed that also this processing step successfully removes the direct wave and background noises. However, this methodology very harshly affects the shapes of the hyperbolic events and strongly removes horizontal and sub-horizontal features throughout the entire time sections. Comparison with this result helps validate the effectiveness of the proposed methodology.

The survey revealed anomalies where buried tombstones might be present. Root patterns are clearly visible on the time slices. This also serves to demonstrate the applicability of the GPR survey to detect shallow features, which can be expected to be wider and more reflective than tree roots.

4.6. ACKNOWLEDGMENTS

We thank the foundation Jewish Westland for approaching us and giving us access to the study site. We thank J. Liu for the constructive discussions about adaptive subtraction.

REFERENCES

- [1] D. Goodman and S. Piro, *GPR Remote Sensing in Archaeology* (Springer Berlin Heidelberg, 2013).
- [2] X. Wang and S. Liu, *Noise suppressing and direct wave arrivals removal in GPR data based on Shearlet transform*, *Signal Processing* **132**, 227 (2017).
- [3] Q.-Z. Bao, Q.-C. Li, and W.-C. Chen, *GPR data noise attenuation on the curvelet transform*, *Applied Geophysics* **11**, 301 (2014).
- [4] N. J. Cassidy, *Ground penetrating radar data processing, modelling and analysis*, in *Ground Penetrating Radar Theory and Applications* (Elsevier, 2009) pp. 141–176.
- [5] J.-L. Starck, E. Candes, and D. Donoho, *The curvelet transform for image denoising*, *IEEE Transactions on Image Processing* **11**, 670 (2002).
- [6] Z.-Y. Zhang, X.-D. Zhang, H.-Y. Yu, and X.-H. Pan, *Noise suppression based on a fast discrete curvelet transform*, *Journal of Geophysics and Engineering* **7**, 105 (2010).
- [7] G. Terrasse, J.-M. Nicolas, E. Trouve, and E. Drouet, *Application of the curvelet transform for clutter and noise removal in GPR data*, *IEEE Journal of Selected Topics in Applied Earth Observations and Remote Sensing* **10**, 4280 (2017).
- [8] J. Baili, S. Lahouar, M. Hergli, I. L. Al-Qadi, and K. Besbes, *GPR signal de-noising by discrete wavelet transform*, *NDT & E International* **42**, 696 (2009).
- [9] I. J. Gupta, A. van der Merwe, and C.-C. Chen, *Extraction of complex resonances associated with buried targets*, in *SPIE Proceedings*, edited by A. C. Dubey, J. F. Harvey, and J. T. Broach (SPIE, 1998).

- [10] A. van der Merwe and I. Gupta, *A novel signal processing technique for clutter reduction in GPR measurements of small, shallow land mines*, *IEEE Transactions on Geoscience and Remote Sensing* **38**, 2627 (2000).
- [11] D. Potin, E. Duflos, and P. Vanheeghe, *Landmines ground-penetrating radar signal enhancement by digital filtering*, *IEEE Transactions on Geoscience and Remote Sensing* **44**, 2393 (2006).
- [12] B. Cagnoli and T. Ulrych, *Singular value decomposition and wavy reflections in ground-penetrating radar images of base surge deposits*, *Journal of Applied Geophysics* **48**, 175 (2001).
- [13] P. K. Verma, A. N. Gaikwad, D. Singh, and M. J. Nigam, *Analysis of clutter reduction techniques for through wall imaging in UWB range*, *Progress In Electromagnetics Research B* **17**, 29 (2009).
- [14] R. Solimene, A. Cuccaro, A. DellAversano, I. Catapano, and F. Soldovieri, *Ground clutter removal in GPR surveys*, *IEEE Journal of Selected Topics in Applied Earth Observations and Remote Sensing* **7**, 792 (2014).
- [15] E. Slob, D. Draganov, and K. Wapenaar, *GPR without a source*, in *Eleventh International Conference on Ground Penetrating Radar* (2006).
- [16] E. Slob and K. Wapenaar, *General representations of electromagnetic interferometry*, in *2007 4th International Workshop on, Advanced Ground Penetrating Radar* (IEEE, 2007).
- [17] E. Slob, *Practical representations of electromagnetic interferometry for GPR applications: a tutorial*, *Near Surface Geophysics* **6**, 391 (2008).
- [18] K. Wapenaar, D. Draganov, R. Snieder, X. Campman, and A. Verdel, *Tutorial on seismic interferometry: Part 1 — basic principles and applications*, *Geophysics* **75**, 75A195 (2010).
- [19] E. Slob, D. Draganov, and K. Wapenaar, *Interferometric electromagnetic Green's functions representations using propagation invariants*, *Geophysical Journal International* **169**, 60 (2007).
- [20] K. Wapenaar, J. Fokkema, and R. Snieder, *Retrieving the Green's function in an open system by cross correlation: A comparison of approaches*, *The Journal of the Acoustical Society of America* **118**, 2783 (2005).
- [21] R. Snieder, *Extracting the Green's function from the correlation of coda waves: A derivation based on stationary phase*, *Physical Review E* **69**, 046610 (2004).
- [22] J. Liu, D. Draganov, and R. Ghose, *Seismic interferometry facilitating the imaging of shallow shear-wave reflections hidden beneath surface waves*, *Near Surface Geophysics* **16**, 372 (2018).

- [23] F. Balestrini, D. Draganov, A. Malehmir, P. Marsden, and R. Ghose, *Improved target illumination at Ludvika mines of Sweden through seismic-interferometric surface-wave suppression*, [Geophysical Prospecting](#) **68**, 200 (2019).
- [24] F. Balestrini, D. Draganov, R. Ghose, E. Koivisto, A. Malehmir, and M. Savolainen, *Surface-wave suppression through seismic interferometry: A case study at the Siilinjärvi phosphate mine in Finland*, in [SEG Technical Program Expanded Abstracts 2020](#) (Society of Exploration Geophysicists, 2020).
- [25] S. Fomel, *Shaping regularization in geophysical-estimation problems*, [Geophysics](#) **72**, R29 (2007).
- [26] S. Fomel, *Adaptive multiple subtraction using regularized nonstationary regression*, [Geophysics](#) **74**, V25 (2009).
- [27] *BRO GeoTop v1.4 DINOloket*, *TNO Geological Survey of The Netherlands*, www.dinoloket.nl.

5

DATA RECONSTRUCTION USING SEISMIC INTERFEROMETRY APPLIED TO ACTIVE-SOURCE DATA FROM THE LUDVIKA MINES OF SWEDEN

Dense and regular trace sampling is of great importance when utilising seismic methods for exploration. An increment in the fold coverage can improve the illumination of the subsurface, resulting in better images of potential deposits and the structures hosting them. Additionally, different advanced seismic processing and imaging algorithms require dense and regular datasets in order to achieve optimum results. Thus, we propose using data retrieved by seismic interferometry as a data-driven method to provide missing traces for relatively large source or receiver gaps. Together with a data-reconstruction algorithm, we merge these two datasets in a more optimal way for further processing as just one dataset. We apply the proposed methodology to a simple numerically modelled dataset and an active-source dataset acquired at the Ludvika Mines of Sweden for imaging its iron-oxide deposit.

Part of this chapter was published as F. Balestrini, M. Sacchi, A. Malehmir, P. Marsden, R. Ghose, and D. Draganov, *Data reconstruction using seismic interferometry applied to active-source data from the Ludvika Mines of Sweden*, in *NSG2020 3rd Conference on Geophysics for Mineral Exploration and Mining* (European Association of Geoscientists & Engineers, 2020).

Note that changes have been applied to make the text and figures consistent with this thesis.

5.1. INTRODUCTION

The utilisation of advanced seismic algorithms to gather information at relatively greater depths with higher resolution increases the demand for dense and regular sampling of the seismic traces. Examples include surface-related multiple elimination and wave-equation migration, which require densely sampled traces and the development of effective interpolation methods. As a consequence, datasets that do not fulfil these requirements will suffer from poor processing results [1]. In addition, because of the low impedance contrast between the mineral deposit and the host rocks, increasing fold coverage might improve the signal-to-noise ratio and lead to better depth illumination. This could help obtain clearer images of the deposits and the structures hosting them.

A way to achieve these requirements is to exploit the available seismic data to the maximum. This can be done through the use of seismic interferometry (SI) [2]. When SI is applied to active-source data, virtual sources are retrieved at the position of the receivers, or reciprocally, virtual receivers are retrieved at the position of the sources. This method allows increasing the amount of the data available with no extra field-acquisition costs, just by data reprocessing.

In this work, we propose to use data retrieved by SI to supply missing traces in relatively large source or receiver gaps in the active-source data. Using SI, we retrieve in a purely data-driven manner virtual sources at positions where there are only receivers, without the use of any a priori velocity model. Since the active-source and the virtual-source datasets have different origins and, thus, amplitudes and wavelets, we aim to implement an algorithm that interpolates and merges these two datasets in an optimal way for further processing them as just one dataset. We developed this methodology through testing on a simple numerically modelled dataset. We then apply this to the 2D reflection seismic profile acquired at the Ludvika mines in 2016, south-central Sweden [3–7].

5.2. METHODOLOGY

SI is a method used to estimate the Green's function between two receivers [8]. This involves the cross-correlation of their responses from different sources and the summation over all the available sources. Consequently, virtual sources are retrieved at positions where there are only receivers. Thus, SI allows the generation of additional data, also where it might not be available from the field acquisition. Another advantage of utilising this method is that no knowledge of the subsurface-medium parameters is required. Moreover, the positions of the active sources do not have to be exactly known.

The responses retrieved by SI can be thus utilised to supply missing traces, in particular, when the active-source data have relatively large gaps, which are the focus of this study. To merge active- and virtual-source data, we propose to apply a data-reconstruction algorithm that merges these two datasets for further processing as just one dataset. In spite of not being a substitute for well-sampled field data, this could still provide a superior result after processing and imaging, and help the data interpretation.

From observed data (or active-source data) that contain a source gap, we retrieve SI responses from virtual sources at the positions of receivers inside the active-source gap. We then use this result to fill in the source gap. We expect that this response will contain

the pseudo-physical events that would be present in the active-source data. However, it will also contain spurious contributions like virtual refractions and non-physical reflections (Chapter 1 and references therein). Hence, we subject this combined dataset to an interpolation algorithm, obtaining the merged data as output (Figure 5.1). For this, we utilise a type of projection-onto-convex-sets (POCS) image-restoration algorithm [9] that performs 2D Fourier transforms to interpolate missing traces. This is a simple iterative method (Figure 5.1) that consists of a 2D Fourier transformation of the data, the application of a threshold to the transformed data leaving only the highest amplitudes, an inverse 2D Fourier transformation of the results of the data with the threshold applied, and finally the reinsertion of the values of the original samples that do not need to be interpolated [10]. The threshold value is varied from a large value during the first iteration to a small value during the last iteration. Similar to other interpolation algorithms, for the case of irregularly missing data, when the events in the trace gaps can be linearly approximated, POCS algorithms generally produce satisfactory interpolation results [10]. However, they fail for the reconstruction of larger gaps, when the recorded event might exhibit curvature. The insertion of SI responses can contribute to overcoming this, since they will pose a constraint and give extra information that can help the reconstruction.

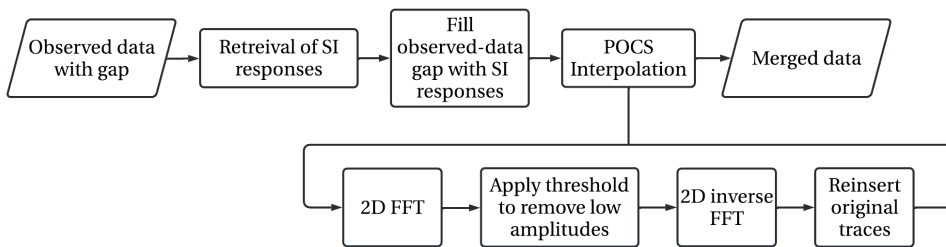


Figure 5.1: Flowchart that illustrates the proposed steps for data reconstruction using SI. The bottom part shows an example of an iteration of the POCS algorithm [10].

5.3. SIMPLE 2D NUMERICALLY MODELLED DATA EXAMPLE

In this section, we show the results obtained after applying the proposed methods to a simple 2D numerically modelled dataset. This dataset is generated using the simple 2D velocity model shown in Figure 5.2a and a 2D finite-difference wavefield modelling code [11] in acoustic mode. The seismic records are computed for a 6 km straight line. Sources are modelled from 0 m to 6000 m every 50 m. Receivers are also placed from 0 m to 6000 m every 25 m. The record length is 3 s, with a time sampling of 4 ms. As a source time function, we use the first derivative of a Gaussian wavelet with a maximum frequency of 65 Hz. The direct wave is generated separately using the same modelling parameters but for a homogeneous model with the velocity and the density of the first layer of the 2D model shown in Figure 5.2a. This direct wave is then subtracted from the generated dataset. Figure 5.2b shows an example of a common-shot gather generated with the velocity model shown in Figure 5.2a. The source is located in the middle of the

array at 3000 m, corresponding to source number 61 and receiver number 121.

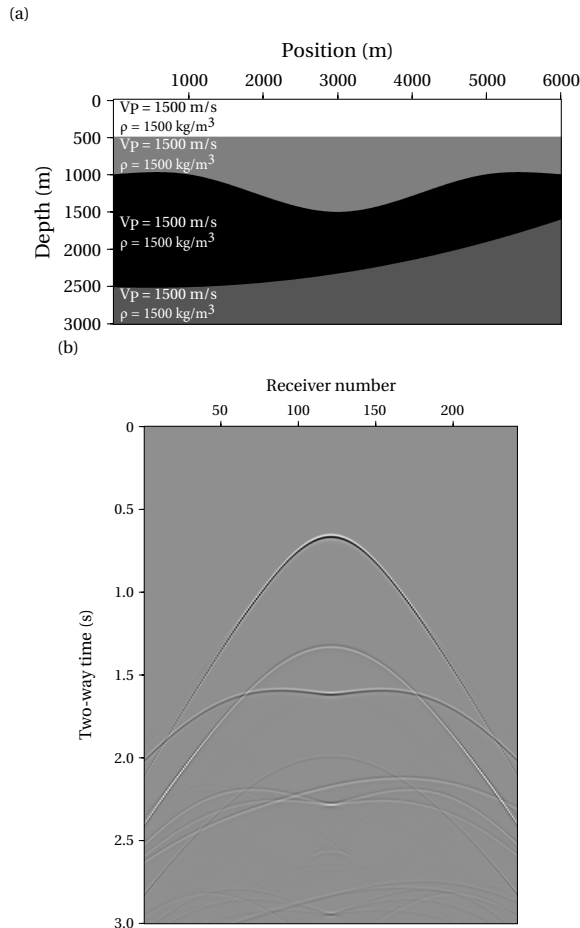


Figure 5.2: (a) Simple velocity model used to generate the active-source data to test the proposed methodology for data reconstruction. (b) Example of a common-shot gather generated with the velocity model in (a) with the source located in the middle of the array at 3000 m, corresponding to source number 61 and receiver number 121.

In order to simulate data characterised by missing sources, we create a gap in the active-source data by removing the recordings from sources located between positions 1200 m and 2500 m (Figure 5.3a), which represent approximately 20% of the data. Following the proposed steps (Figure 5.1), we use the observed data with the source gap as an input to retrieve the SI responses. In Figure 5.3b, we can see that SI has retrieved not only the events present in the active-source data but also spurious contributions like virtual refractions and non-physical reflections. We apply a top-mute mask to these SI responses in order to remove the ringing noises and artefacts that arrive at times earlier than the first arrival in the active-source data. Following, we use the traces retrieved

by SI to fill in the gap in the active-source data (Figure 5.3c). Again, we can see, more clearly now, that most events present in the active-source dataset are well kinematically retrieved (red arrows), especially for earlier times. However, noises and spurious events are still present (yellow arrows). In order to avoid amplitude differences, both datasets are normalised. Note that retrieval of events by SI requires the presence of multiple reflections in the active-source data to be cross-correlated with primary or lower-order multiple reflections. This way, multiples are transformed into primaries or lower-order multiples. Therefore, to retrieve events at later times, longer recordings are needed. For this case, the length of the active-source data recordings allows retrieving events up until ~ 2.4 s. Reflection events at later times cannot be retrieved because multiples at times later than 3 s are required, which are not recorded in the simulated data.

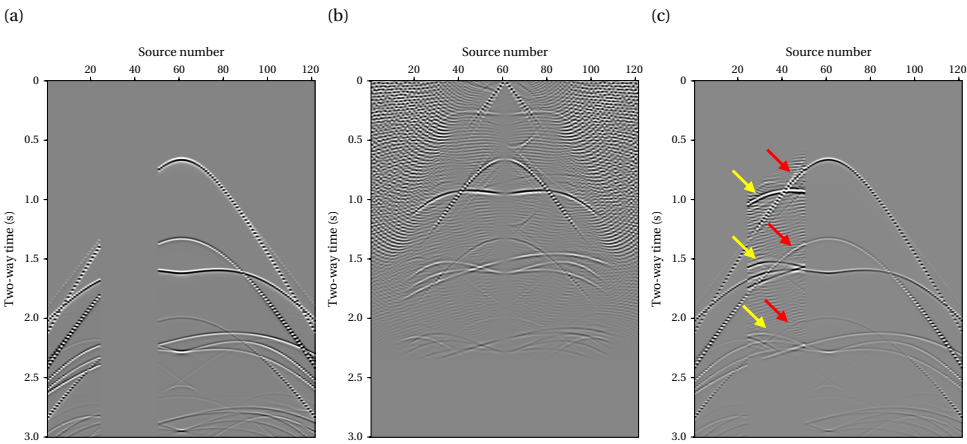


Figure 5.3: (a) Example of a common-receiver gather with the receiver located in the middle of the array at position 3000 m, corresponding to receiver number 121 and shot number 61, with a generated source gap between positions 1200 m and 2500 m. (b) SI responses obtained for the common-receiver gather in (a). (c) The common-receiver gather in (a) with the source gap filled in with the traces retrieved with SI in (b) after top-mute. The red arrows indicate several retrieved pseudo-physical events that coincide with those in the active-source data. The yellow arrows indicate retrieved non-physical reflections.

Subsequently, we subject the active-source data with the generated source gap filled in with the responses retrieved with SI (Figure 5.3c) to the POCS interpolation algorithm, obtaining the output shown in Figure 5.4a. We can observe that some low-amplitude background noise arises, which was expected from the use of this interpolation algorithm [10]. However, the active-source events are reconstructed (red arrows), whilst spurious events are suppressed, achieving better results for earlier times. In order to investigate the usefulness of the methodology we propose, we subject the active-source data with the source gap (Figure 5.3a) directly to the POCS interpolation algorithm (without the use of the responses retrieved with SI to fill in the source gap), obtaining the result shown in Figure 5.4b. We can see, once more, that low-amplitude background noise is present. Additionally, the interpolation algorithm performs poorly to reconstruct the missing events, even though for this common-receiver gather, the gap is located mostly at the slopes of the hyperbolic events from the reflections, where they do not exhibit

curvature and are nearly linear. Comparing both results, we can clearly see that by using the SI responses to fill in the source gap present in the active-source data, prior to subjecting the data to the POCS interpolation algorithm, we can obtain a much better reconstruction of the events of interest.

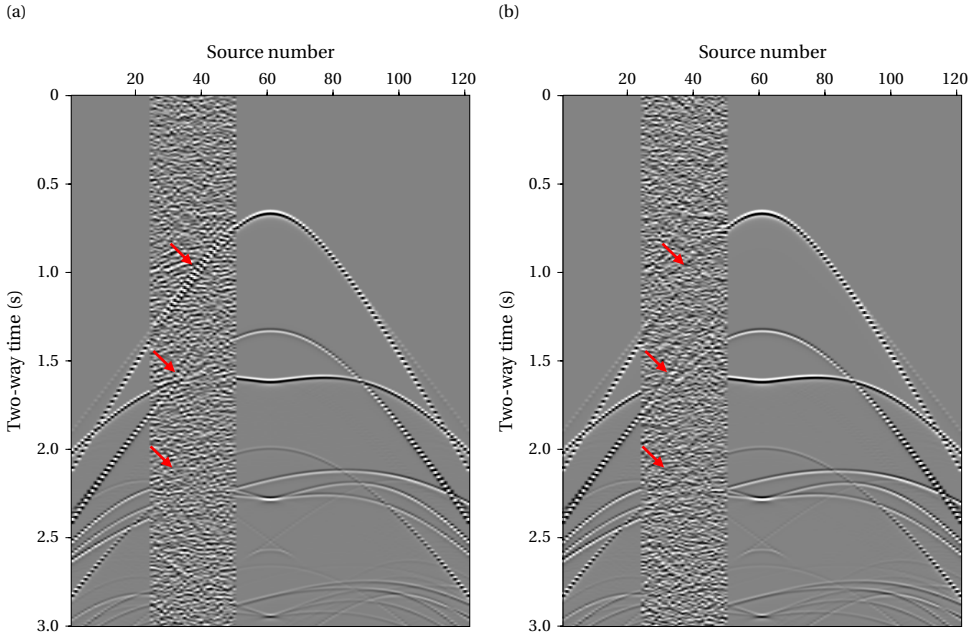


Figure 5.4: (a) Result obtained after subjecting the common-receiver gather with the generated source gap filled in with the responses retrieved with SI (Figure 5.3c) to the POCS interpolation algorithm. (b) Result obtained after subjecting the common-receiver gather with the generated source gap (Figure 5.3a) directly to the POCS interpolation algorithm (without the use of the responses retrieved with SI to fill in the source gap). The red arrows point at the locations of reflection events.

After obtaining these results, we apply pre-stack depth migration to the data with the source gap (Figure 5.5a), the interpolated data using the SI responses to fill in the source gap (Figure 5.5b), and the interpolated data using the data with the source gap (Figure 5.5c) utilising the velocity model in Figure 5.2a. Once more, we can see that the imaged events are better reconstructed when using the SI responses to fill in the source gap in the active-source data. Additionally, the events located around 1250 m depth and around 2000 m depth are reconstructed, even though they are a result of the presence of multiples in the data, do not represent subsurface structures and, thus, they have lower amplitudes. Additionally, in spite of not achieving a perfect wavelet matching and that some background noise arises due to the use of the interpolation algorithm, using SI responses to fill in the source gap allows obtaining structures that are laterally much more continuous. However, we can observe in Figure 5.5b that there are some linear artefacts around the imaged reflectors (yellow arrows). These result from the imperfect elimination of artefacts and non-physical events present in the SI responses. Nonetheless, our approach gives a result that also avoids the various sources of noise present at

larger depths (yellow arrows in Figure 5.5a and Figure 5.5c) that come from the lack of information due to the existence of a source gap. In Figure 5.5c, we can see some reconstruction on the sides of the gap. However, the interpolation algorithm fails to retrieve events towards the centre of the gap (red arrows).

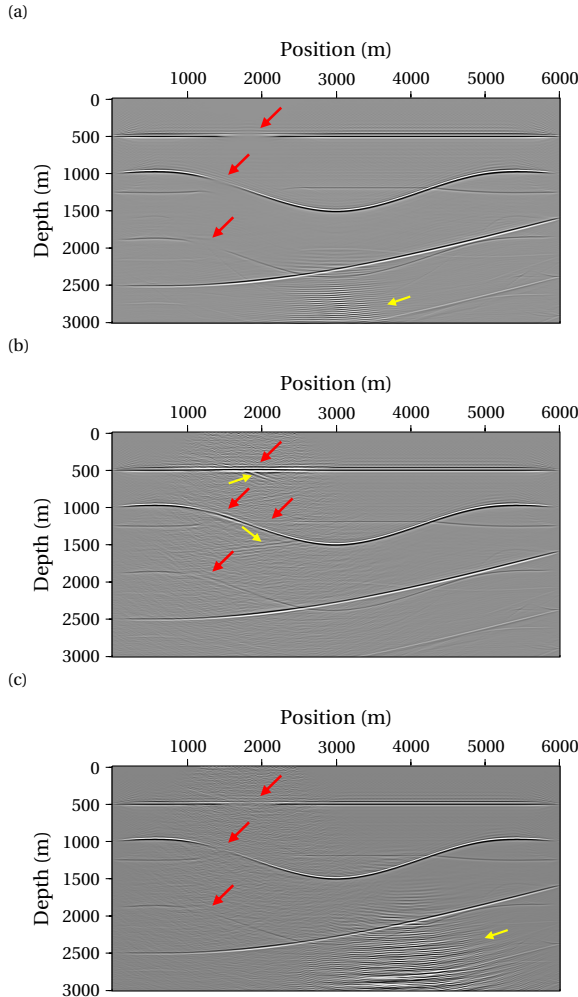


Figure 5.5: (a) Pre-stack depth migrated section of the active-source data with the source gap. (b) Pre-stack depth migrated section of the interpolated data using the SI response to fill in the source gap. (c) Pre-stack depth migrated section of the interpolated data using the data with the source gap. The red arrows point at the location where the reflectors should be imaged. The yellow arrows point at noises and spurious events.

5.4. BLÖTBERGET IRON-OXIDE DEPOSIT DATA

As mentioned in Chapter 2, the mineralisation in the Blötberget mining area of the Ludvika Mines of Sweden is known for its rich and high-quality iron-oxide deposits, and it

consists mainly of magnetite and hematite, along with the presence of small amounts of apatite, quartz, and calc-silicate minerals. The mineralised units are known to dip approximately 45° towards the southwest, down up to 500 m depth. Further below, the units start dipping more gently until the known depth of about 850 m [3–6]. Figure 5.6 shows a bedrock map of the Blötberget mining area and the location of the seismic profile (red and blue crooked line), along which the sources and receivers were positioned when a 2D reflection seismic dataset was acquired in a field campaign in 2016 [3–6]. The spacing between receivers as well as the spacing between shots was 5 m. More details about the data acquisition can be found in Chapter 2.

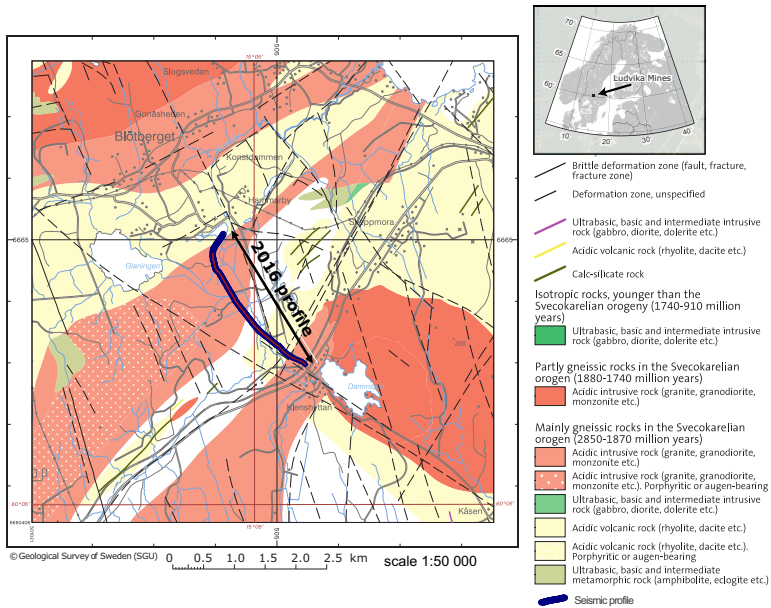


Figure 5.6: Bedrock map of the Blötberget mine and the location of the seismic profile, focus of this study, modified from the Geological Survey of Sweden.

As mentioned in Chapter 1, the suppression of surface waves is an important processing step. In Chapters 2 and 3, we showed that the responses retrieved with SI will be dominated by surface waves. Thus, the suppression of the surface waves is particularly required to be able to retrieve stronger reflection events through SI and to avoid extra artefacts. Thus, before applying SI for data reconstruction, the data are subject to surface-consistent refraction static corrections [5, 12], interferometric surface-wave suppression (see Chapter 2) and filtering. Figure 5.7a and Figure 5.7b show an example of a common-receiver gather as recorded in the field and after the aforementioned processing steps, respectively. The reflections from the mineralisation zone (red arrows) [5, 6, 12] are better appreciated after these processing steps, also for later times. However, we can see that these kinds of data have a rather low signal-to-noise ratio, posing a further challenge to retrieve pseudo-physical reflections through SI.

After these steps, we create a source gap for the sources between station number

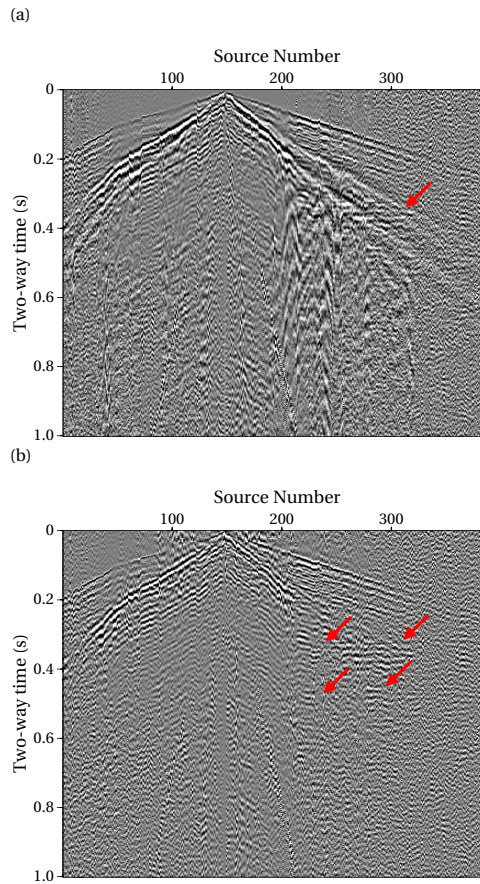


Figure 5.7: (a) Example of a common-receiver gather as recorded in the field, corresponding to receiver number 150 and source number 168. (b) Same gather but after interferometric surface-wave suppression and filtering. The reflections from the mineralisation zone (red arrows) are better appreciated after this processing step, also for later times.

200 and station number 300 (Figure 5.8a), which represent approximately 25% of the data. We then cross-correlate the responses from the same sources recorded at different receivers, and stack them over the available sources. This way, we retrieve SI responses or virtual sources at the position of the receivers (Figure 5.8b). Following, we fill in the source gap in the field data with this result (Figure 5.8c). Note that for the numerically modelled-data example, surface waves are not modelled, whilst for the field dataset there is still some surface-wave energy that remains, even though the surface waves are suppressed during the processing stage. These are also retrieved in the SI responses. Therefore, due to the fact that the field data are highly noisy, even after interferometric surface-wave suppression, it is challenging to precisely recover the active-source reflections through SI for this case. However, we can see some continuity for the direct arrival, for the surface-wave energy that is still present, and, most importantly, for the almost

flat reflection events between around 0.3 s and 0.5 s (red arrows in Figure 5.8c).

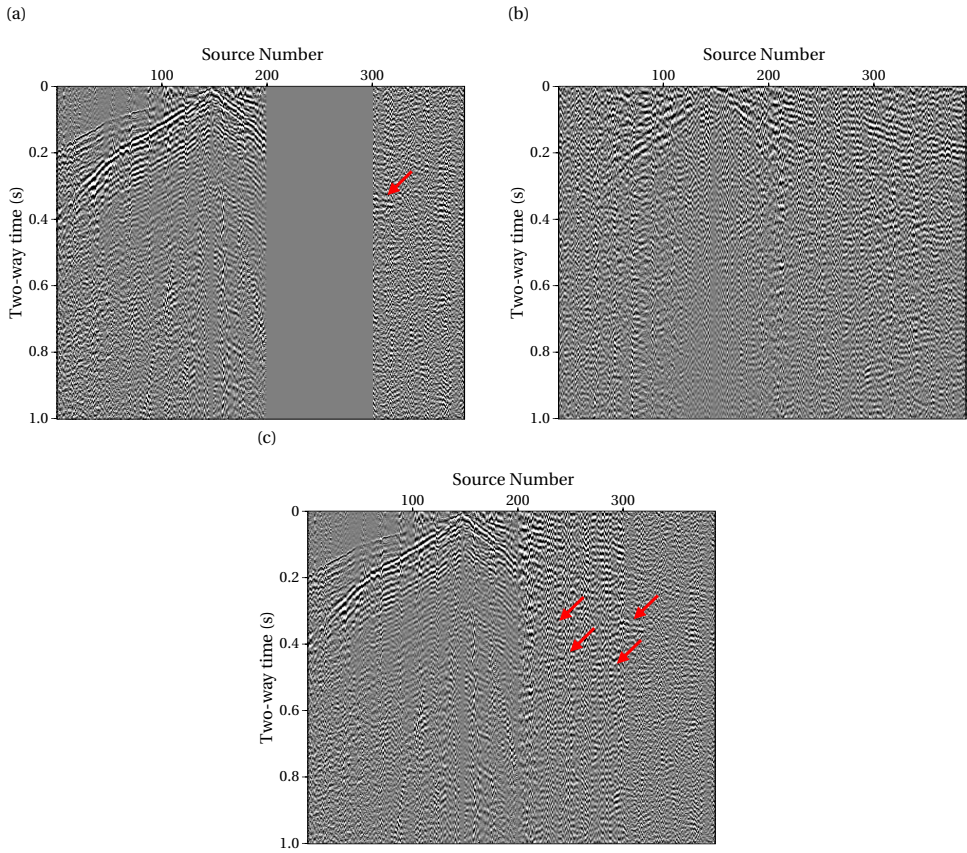


Figure 5.8: (a) Common-receiver gather in Figure 5.7b with a source gap between source number 200 and source number 300. (b) SI responses obtained for the common-receiver gather in (a). (c) Common-receiver gather in (a) with the source gap filled in with the traces retrieved with SI in (b). The red arrows point at the reflections from the mineralisation zone

Following the steps for data reconstruction, we subject the active-source data with the source gap (Figure 5.8a) and the active-source data with the source gap filled in with the SI responses (Figure 5.8c) to the POCs interpolation algorithm, obtaining the outputs shown in Figure 5.9a and Figure 5.9b, respectively. Finally, Figure 5.10a, Figure 5.10b, and Figure 5.10c show the unmigrated stacked sections between CMP 270 and CMP 860 obtained from the data with a source gap, the interpolated data obtained using the data with the source gap, and the interpolated data using the obtained SI responses to fill in the source gap, respectively. The target mineralisation is represented by the dipping nearly flat horizons between 0.3 s and 0.4 s (red arrows). Even though this reflector appears stronger in Figure 5.10a, it might be misinterpreted as being crosscut by two faults. The reconstructed result in Figure 5.10c suggests the correct interpretation of the continuity of the reflector, with the result after filling in the gap with the SI responses giving a

bit stronger continuity of the reflector at its right side. The biggest gain from filling in the gap with the SI responses appears in the shallower part, where the unmigrated stacked section gives evidence of a shallower structure (red ellipse in Figure 5.10c), known to be present (see Chapter 2), while the result in Figure 5.10a and Figure 5.10b do not give such evidence.

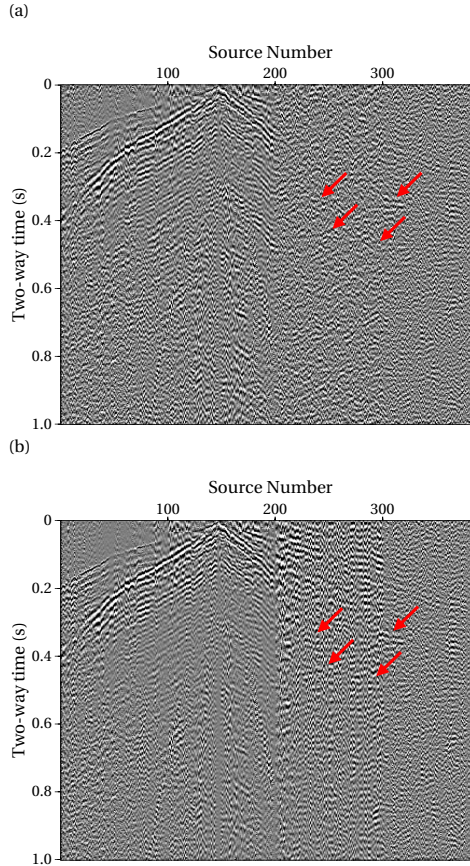


Figure 5.9: (a) Result obtained after subjecting the common-receiver gather with the source gap in Figure 5.8a to the POCS interpolation algorithm. (b) Result obtained after subjecting the common-receiver gather with the source gap filled in with the traces retrieved with SI in Figure 5.8c to the POCS interpolation algorithm.

As we have seen from the numerically modelled example, even the dipping layers should be better imaged using the data with the source gap filled in with the SI responses. The fact that we see only a small improvement in the imaging of the dipping layers in the filled-in data might actually mean that these reflectors also have a dip, albeit slight, in the crossline direction (i.e., a 3D effect). Even a slight dip in the crossline direction will result in the SI data retrieved along a line, with the assumption that the subsurface is purely 2D, to be less than optimal.

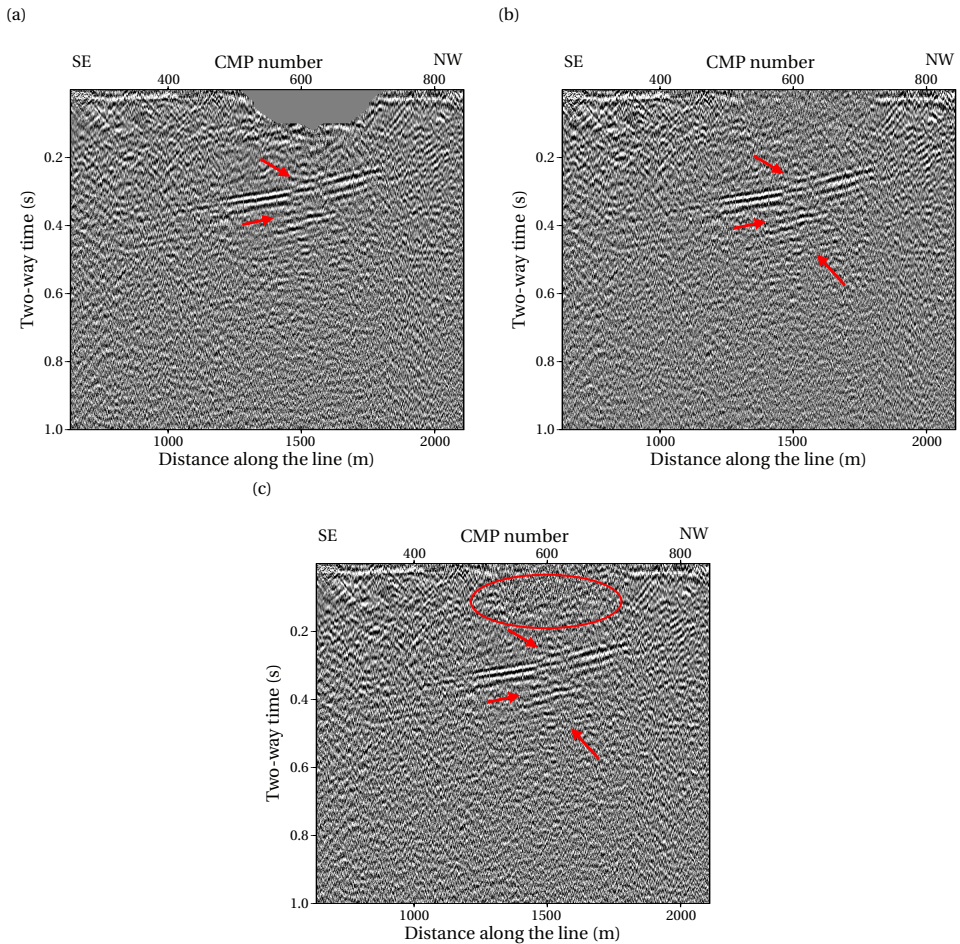


Figure 5.10: (a) Unmigrated stacked sections between CMP 270 and CMP 860 obtained for the data with the source gap. (b) Unmigrated stacked sections between CMP 270 and CMP 860 obtained for the interpolated data with the source gap. (c) Unmigrated stacked sections between CMP 270 and CMP 860 obtained for the interpolated data using the SI responses to fill in the source gap.

5.5. CONCLUSIONS

We proposed a novel methodology for data reconstruction that consists of retrieving SI responses to estimate missing traces in a relatively large source gap, followed by a projection-onto-convex-sets interpolation algorithm. These estimations are purely data-driven and do not require the use of any a priori velocity model or knowledge of the subsurface characteristics. This methodology could help fulfil the demand for dense and regular sampling of traces for seismic processing algorithms when such data are not available due to field conditions restricting the acquisition geometry.

We presented the results for two different datasets. The numerically modelled dataset showed clear improvements when using SI responses prior to the POCS inter-

polation algorithm. However, as expected, it was harder to get similar results for the field data acquired at the Ludvika Mines of Sweden. These data are highly noisy and, therefore, it is harder to precisely recover active-source reflections than for the numerically modelled cases, increasing the difficulty for the interpolator to reconstruct the missing data. Nevertheless, the field dataset still exhibited improvements when comparing the stacked section obtained when the interpolation algorithm was applied after inserting the SI responses in the source gap to the stacked sections obtained from the data with the gap and to the stacked section obtained from the data with the gap after POCS. Therefore, the methodology we proposed could help fulfil the demand for dense and regular sampling of traces for seismic processing algorithms.

5.6. ACKNOWLEDGEMENTS

This study was carried out within the Smart Exploration project. Smart Exploration has received funding from the European Union's Horizon 2020 research and innovation programme under grant agreement No. 775971. We thank Uppsala University and Nordic Iron Ore AB (NIO) for providing access to the datasets and collaborating with us through the Smart Exploration project. The seismic data were processed using a combination of Seismic Unix, ProMAX and software from the Delphi Consortium.

REFERENCES

- [1] G. Poole and D. Lecerf, *Effect of regularization in the migration of time-lapse data*, *First Break* **24** (2006), 10.3997/1365-2397.2006007.
- [2] K. Wapenaar, D. Draganov, and J. O. A. Robertsson, *Seismic interferometry: history and present status* (Society of Exploration Geophysicists, 2008).
- [3] A. Malehmir, L. Dynesius, K. Paulusson, A. Paulusson, H. Johansson, M. Bastani, M. Wedmark, and P. Marsden, *The potential of rotary-wing UAV-based magnetic surveys for mineral exploration: A case study from central sweden*, *The Leading Edge* **36**, 552 (2017).
- [4] L. Bräunig, S. Buske, A. Malehmir, E. Bäckström, M. Schön, and P. Marsden, *Seismic depth imaging of iron-oxide deposits and their host rocks in the Ludvika mining area of central Sweden*, *Geophysical Prospecting* **68**, 24 (2019).
- [5] M. Markovic, G. Maries, A. Malehmir, J. Ketelhodt, E. Bäckström, M. Schön, and P. Marsden, *Deep reflection seismic imaging of iron-oxide deposits in the Ludvika mining area of central Sweden*, *Geophysical Prospecting* **68**, 7 (2019).
- [6] F. Balestrini, D. Draganov, A. Malehmir, P. Marsden, and R. Ghose, *Improved target illumination at Ludvika mines of Sweden through seismic-interferometric surface-wave suppression*, *Geophysical Prospecting* **68**, 200 (2019).
- [7] F. Balestrini, M. Sacchi, A. Malehmir, P. Marsden, R. Ghose, and D. Draganov, *Data reconstruction using seismic interferometry applied to active-source data from the Ludvika Mines of Sweden*, in *NSG2020 3rd Conference on Geophysics for Mineral Exploration and Mining* (European Association of Geoscientists & Engineers, 2020).

- [8] K. Wapenaar, D. Draganov, R. Snieder, X. Campman, and A. Verdel, *Tutorial on seismic interferometry: Part 1 — Basic principles and applications*, [Geophysics 75, 75A195 \(2010\)](#).
- [9] H. Stark, *Image Recovery: Teory and Application* (Academic Press, Orlando, 1987).
- [10] R. Abma and N. Kabir, *3d interpolation of irregular data with a POCS algorithm*, [Geophysics 71, E91 \(2006\)](#).
- [11] J. W. Thorbecke and D. Draganov, *Finite-difference modeling experiments for seismic interferometry*, [Geophysics 76, H1 \(2011\)](#).
- [12] A. Malehmir, G. Maries, E. Bäckström, M. Schön, and P. Marsden, *Developing cost-effective seismic mineral exploration methods using a landstreamer and a drophammer*, [Scientific Reports 7 \(2017\), 10.1038/s41598-017-10451-6](#).

6

INTERFEROMETRIC DATA RECONSTRUCTION INSIDE RELATIVELY LARGE GAPS UTILISING HYPERBOLIC RADON TRANSFORMS

Seismic-interpolation algorithms are mostly developed to regularise data acquired in an irregular geometry and to reconstruct either uniformly or randomly missing traces. However, these methods tend to perform poorly when trying to reconstruct data in a relatively large gap, especially if the seismic events exhibit more pronounced curvatures. In these cases, data-reconstruction algorithms are commonly used for marine-data applications in order to interpolate the near-offset traces. Seismic interferometry can provide new responses in order to supply missing traces that can be utilised for the reconstruction of seismic events. However, these new responses contain noises and spurious events which need to be alleviated in order to obtain an appropriate result. In this work, we present a simple and practical methodology to suppress the spurious events and alleviate the noises in the SI responses to further combine active-source data with virtual-source data in a suitable way, focusing on land near-surface applications. In this new approach, we utilise the ability of Radon transforms to focus and separate hyperbolic events with different curvatures. In order to suppress the spurious events in the SI responses that are not present in the active-source data, filtering is performed in the Radon domain. We first transform the active-source data that contains a large gap and the virtual-source data to the Radon domain. Subsequently, we utilise the active-source data to create a mask to filter the SI responses in the Radon domain. After transforming the virtual-source data back to the time-offset domain, we obtain a more optimal SI result for merging. This results in a data-driven methodology for data-reconstruction that does not require the use of any a priori velocity model or knowledge of the subsurface. Our results show that, in spite of not being at the quality of well-sampled field data, the methodology can provide a superior result when compared with the results after classic Radon interpolation, producing higher-resolution images of the subsurface.

This chapter is in preparation for publication

6.1. INTRODUCTION

Seismic data often suffers from irregular or sparse spatial sampling, for instance, as a result of cost constraints or field-acquisition restrictions. Avoiding these limitations can result in superior fold coverage and help obtain higher-resolution images of the subsurface. Several processing and imaging techniques, such as multiple elimination and migration algorithms, can be severely affected by the lack of regular and sufficiently dense sampling, and have been proven to provide better-quality results once superior spatial sampling requirements are met. However, these limitations are hard to avert. Hence, algorithms for the reconstruction of seismic data are a commonly utilised processing step.

Several methods with different approaches have been proposed for this end. Prediction-based methods [1–3] make use of the linear prediction of the signal in the f - x and f - k domains. Usually, for these methods, data from lower frequencies are used to estimate prediction error filters (PEF) [4] to recover data from higher frequencies. Wave-equation-based methods [5, 6] utilise wave-propagation principles to reconstruct seismic data, most commonly by inverting operators that link the data to a subsurface model. These methods require thus knowledge of the velocity in the subsurface. Methods based on signal-processing principles, or transform-based, exploit the property of the data in an auxiliary space (such as Fourier, curvelet, and Radon domains). These methods can be implemented by many different algorithms, for instance, the antileakage Fourier transform [7], projection onto convex sets [8], curvelet transforms [9–11], and Radon transforms (RT) [12, 13].

In particular, parabolic and hyperbolic RT (PRT and HRT, respectively) are sometimes used for interpolation and aperture extension. In each case, there is an operator that maps the model space (RT domain) to the data space (time and space), and its adjoint (or conjugate transpose) that performs the reverse mapping from data to model. Then, the interpolation process entails mapping back the model space to the data space using a new geometry. The quality of the interpolation depends on the similarity between the seismic events and the basis functions [12]. Because several seismic events, like reflections and diffractions, can be approximated by hyperbolas, HRT represents a powerful tool for data reconstruction. However, it becomes more challenging when not applied to a relatively noise-free CMP gather with large aperture. If the CMP gather contains gaps and/or noise, improvement can be achieved by forcing sparseness on the Radon model [14].

SI has been utilised as well for data reconstruction in the past years. In conventional processing, multiple reflections are considered noise. Contrary to this, SI takes advantage of the extra information that multiple events provide and uses them for retrieval of primary events [15–17]. However, as mentioned in Chapter 1, the traces retrieved by SI contain several artefacts, which arise due to the non-compliance with the made assumptions, but also from the limited number and limited aperture width of sources (or receivers when sources are turned into virtual receivers), further impaired by the presence of additional source or receiver gaps. The presence of scatterers in the medium can act as an aperture enlargement [18], but they might also contribute to attenuation. Other errors could also arise due to a variable source wavelet [18]. Several methodologies have been developed making use of SI to estimate missing traces and to partially alleviate artefacts from the aforementioned conditions. Berkhouit and Verschuur [16]

transformed the primary energy into a focal point, which then transforms the surface-related multiples into primaries that are used to fill in the missing traces. Wang *et al.* [19] cross-correlated and summed active-source data to interpolate the near-offset missing traces and then applied a least-squares matching filter or PEF to correct the wavelet and amplitude distortions. Curry and Shan [17] interpolated near-offset traces by first separating primaries and free-surface related multiples. Primaries are then used to transform the multiples into virtual-source primaries by cross-correlation and summation. Then a PEF is used to optimise the result. Wang *et al.* [20] and Hanafy and Schuster [21] proposed a two-stage model-based interferometric interpolation method to fill in the near-offset trace interval. A synthetic gather is first generated with a water-layer model (sea-bed depth and water velocity are required) to replace the missing gathers. Then, virtual-source traces are created by cross-correlation and summation between the synthetic water-layer-modelled data and the original seismic data.

The methods mentioned above are commonly developed and utilised for the interpolation and regularisation of sparse data or randomly missing traces. However, they tend to fail and produce poor results when applied for the case of relatively large gaps in the data, in particular when the seismic events exhibit pronounced curvature. In addition, SI methods for data reconstructions are mostly developed for marine-data applications, utilised to supply the near-offset missing traces. Nevertheless, when applied to land data, the responses retrieved by SI contain additional spurious events from the direct and surface wave, whilst physical arrivals are harder to recover due to stronger wave attenuation.

In Chapter 5, we introduced a new methodology that utilises seismic-interferometric responses to fill in relatively large gaps before applying the POCS image restoration algorithm. The results showed that the proposed methodology could provide a superior data reconstruction when compared with the result after only applying the POCS reconstruction algorithm. However, the results obtained after applying the proposed method also exhibited background noise generated by the POCS algorithm, and artefacts from the SI responses were still present.

Therefore, in this work, we introduce a new approach for data reconstruction that utilises SI responses to supply missing traces in relatively large gaps present in the active-source data, and at the same time suppress spurious events in the SI data. Here, we focus on land near-surface applications. The developed methodology utilises HRT not only for interpolation, but also to filter the SI responses in order to combine them with the active-source data in a suitable way. Taking advantage of the ability of the HRT to focus and separate hyperbolic events with different curvatures (i.e., reflections and diffractions with different velocities), the spurious events that are not present in the active-source data can be suppressed in the Radon domain while preserving the physical arrivals to obtain a more suitable SI result for merging. The success of the interpolation depends thus on the ability of the HRT to reproduce the data and separate the seismic events. The application of the methodology can provide useful data preconditioning that allows processing techniques to work better, and hence provide a superior imaging result. Using SI, we retrieve virtual sources at positions where there are receivers by cross-correlating and summing traces in a purely data-driven manner, without the use of any a priori velocity model. Additionally, the proposed method results in a simple and practical application

that better honours the SI data.

6.2. METHODOLOGY

6.2.1. SEISMIC INTERFEROMETRY

As mentioned in the previous chapters, SI is a method used to estimate the Green's function between two receivers. SI can be used with sources of different nature such as active sources, earthquakes, and noise sources [22]. Once more, here we focus on the active-source case for near-surface applications. Thus, the SI process involves the cross-correlation of responses from an active source located at the surface, recorded at two different receiver locations. This is done for all available sources, with subsequent summation of the cross-correlated responses [23]. Consequently, sources are retrieved at the positions of the receivers, and pseudo-physical reflections are obtained by transforming multiples into primaries (Figure 1.1). These retrieved sources are usually referred to as virtual sources. An advantage of using SI to generate new responses is that no knowledge of the subsurface medium parameters is required. Moreover, the positions of the active sources do not have to be exactly known.

6.2.2. HYPERBOLIC RADON TRANSFORM

In general, the RT is implemented to map events with different shapes or curvatures in the data space, and focus them in a new domain or model space. The linear RT has been used for seismic processing in the slant-stack or $\tau - p$ domain for multiple attenuation, stack, and migration. The PRT and HRT are also used for multiple attenuation, and for interpolation and aperture extension [24]. The HRT is commonly used for processing CMP gathers. In the CMP gathers, the reflection events appear as symmetric hyperbolas with their apexes centred at zero offsets (Figure 6.1a). The HRT is defined in terms of summation along hyperbolic paths [14, 24]. Therefore, in the Radon domain, events with hyperbolic move-outs are focused into points (Figure 6.1b).

If we denote the data in the time-offset domain by $d(t, h)$ and in the Radon domain by $\tilde{m}(\tau, \nu)$, the RT is defined as

$$\tilde{m}(\tau, \nu) = \int_{h_{max}}^{h_{min}} d\{t = f(\tau, \nu), h\} dh, \quad (6.1)$$

where h indicates offset, τ indicates the zero-offset two-way travel time. For the case of the HRT, $f = \sqrt{\tau^2 + qh^2}$, where $q = 1/\nu^2$ is the curvature parameter, with ν denoting the root-mean-square velocity. The forward RT is given by

$$d(t, h) = \int_{q_{max}}^{q_{min}} m\{\tau = \sqrt{t^2 + qh^2}, q\} dq, \quad (6.2)$$

where m represents a decomposition of the gather in hyperbolic curves. Equation 6.2 can be discretised and expressed in a matrix form as

$$\mathbf{d} = \mathbf{Lm}, \quad (6.3)$$

where \mathbf{d} represents the CMP gather and \mathbf{m} its Radon panel. A low-resolution Radon panel can be estimated by using the adjoint or transpose operator \mathbf{L}^T . Then, the Radon panel

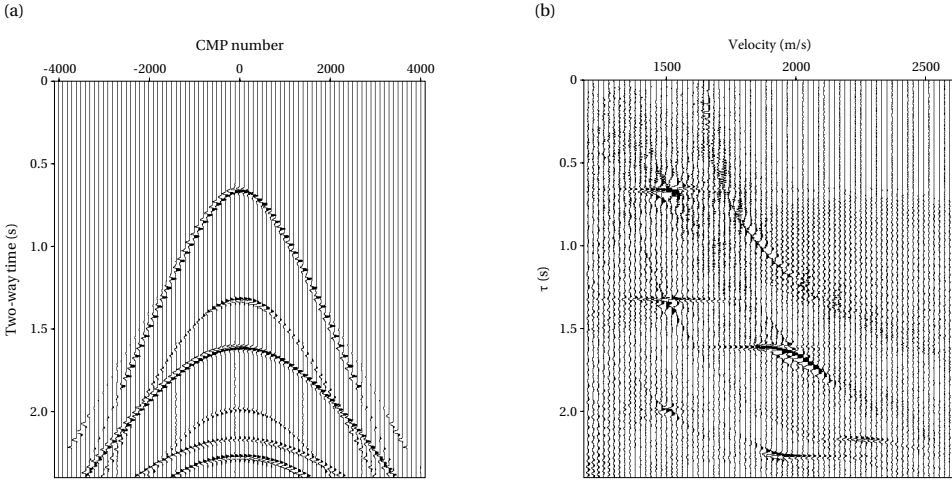


Figure 6.1: (a) Synthetic CMP gather with several hyperbolic events. (b) HRT of (a)

is given by [12, 24]

$$\tilde{\mathbf{m}} = \mathbf{L}^T \mathbf{d}. \quad (6.4)$$

Different from other transform operators, RTs are not orthogonal transforms [12, 24]. Consequently, the transformed model $\tilde{\mathbf{m}}$ and the true model \mathbf{m} are not identical since \mathbf{L}^T does not define the inverse operator ($\mathbf{L}\mathbf{L}^T \neq \mathbf{I}$, where \mathbf{I} is the identity matrix). Therefore, the problem of applying the forward and inverse operators implies loss of data, and the HRT is thus obtained most commonly by inversion methods.

In order to invert Radon operators and obtain an estimate of \mathbf{m} , the vector of residuals $\mathbf{r} = \mathbf{d} - \mathbf{L}\mathbf{m}$ is minimised. Since this represents an ill-posed problem, a regularisation term must be included to obtain a stable and unique solution for \mathbf{m} . Consequently, the inversion problem can be solved by minimising the cost function J defined as

$$J = \|\mathbf{r}\|_s^s + \mu \|\mathbf{m}\|_t^t, \quad (6.5)$$

where μ is a trade-off parameter that controls the relative weight between the model regularisation term $\|\mathbf{m}\|_t^t$ and the misfit term $\|\mathbf{d} - \mathbf{L}\mathbf{m}\|_s^s$. The indices s and t represent the different norms that could be applied to the misfit and model regularisation terms, respectively, in order to obtain, for example, sparse or smooth solutions of the inverse problem [25]. To obtain a sparse solution, one can choose an L1-norm for the model and an L2-norm for the data misfit. However, this problem with mixed norms can be transformed into an L2-L2 problem by replacing μ with model-dependent weight matrices defined as [25]

$$[W_m]_{ii} = \frac{1}{\sqrt{m_i}} \quad (6.6)$$

since

$$\|\mathbf{m}\|_1^1 = \sum_i |m_i| = \mathbf{m}^T W_m^T W_m \mathbf{m} = \|W_m \mathbf{m}\|_2^2. \quad (6.7)$$

There are many different methods to find the solution to the inverse problem (Equation 6.5). For the results presented in this work, the HRT solutions are iteratively estimated using the conjugate gradient method [26], which is commonly utilised for solving large sparse systems of linear equations [12, 25, 27, 28].

6.2.3. MERGING OF ACTIVE- AND VIRTUAL-SOURCE DATA

As previously mentioned, RTs have been widely used as efficient interpolators to extend aperture and fill in missing data, in particular, from small gaps or for randomly missing traces. This method relies on the ability of the transform to focus the seismic data in an appropriate transform space. Because hyperbolas can represent the travel times of various seismic events, the HRT can be a powerful tool for interpolation. In addition, SI can provide extra information by retrieving new seismic responses from virtual sources at the positions of the receivers, or reciprocally, virtual receivers at the positions of the sources. The data retrieved by SI can provide the missing traces to fill in source or receiver gaps. However, SI responses contain noises and spurious events, including non-physical reflections [29–35]. Therefore, we propose to use HRT not only as a tool for interpolation, but also to filter the SI data in the Radon domain to try to suppress in it undesired signals. Then, we use the SI result filtered in the Radon domain to merge the active- and virtual-source data.

Thus, the proposed method consists of firstly retrieving SI responses of virtual sources at the position of the receivers (or virtual receivers at the positions of the sources) to provide the missing traces in a source gap (or receiver gap, respectively) by cross-correlation of the active-source recordings and the consecutive summation. Secondly, we sort both the active-source dataset with missing traces and the virtual-source data retrieved with SI in CMP gathers and perform the HRT. We expect that, despite presenting a large gap, the active-data events will focus in the Radon domain. We then use each transformed active-source CMP gather to create a filter, or mask, that we apply to its respective transformed virtual-source CMP gather. This mask varies its amplitudes from 0 to 1 according to the amplitudes in the transformed active-source CMP gather. For instance, it contains 0 where the amplitudes of the transformed active-source CMP gather are below a predefined percentage of the maximum amplitude, suppressing noises and spurious events in the retrieved SI data. Above that level, the filter values increase linearly to 1, which corresponds to the highest amplitudes of the transformed active-source CMP gather where the active-source events are present, preserving the pseudo-physical events in the retrieved SI data. As a last step, we transform the masked SI responses back to the time-offset domain, and we replace the missing traces in the active-source dataset with the filtered result. Some advantages of the proposed method are that it is very practical and easy to apply, and being the retrieval of SI responses data-driven, it does not require any previous knowledge of the subsurface.

6.3. NUMERICALLY MODELLED DATA EXAMPLE

As a first example, we apply the proposed methodology to a numerically modelled dataset. The dataset is generated using a 2D finite-difference wavefield modelling code [36] in acoustic mode, applied to the 2D velocity model shown in Figure 6.2a. The seis-

mic records are computed for a 6 km straight line, sources are modelled from 0 m to 6000 m along the line every 40 m. Receivers are also placed from 0 m to 6000 m, every 20 m. The record length is 4 s with a time sampling of 4 ms. As a source function, we utilise a Ricker wavelet with a maximum frequency of 65 Hz. Figure 6.2b shows an example of a common-shot gather generated with the velocity model shown in Figure 6.2a with the source located at 3000 m, corresponding to shot number 75 and receiver number 150.

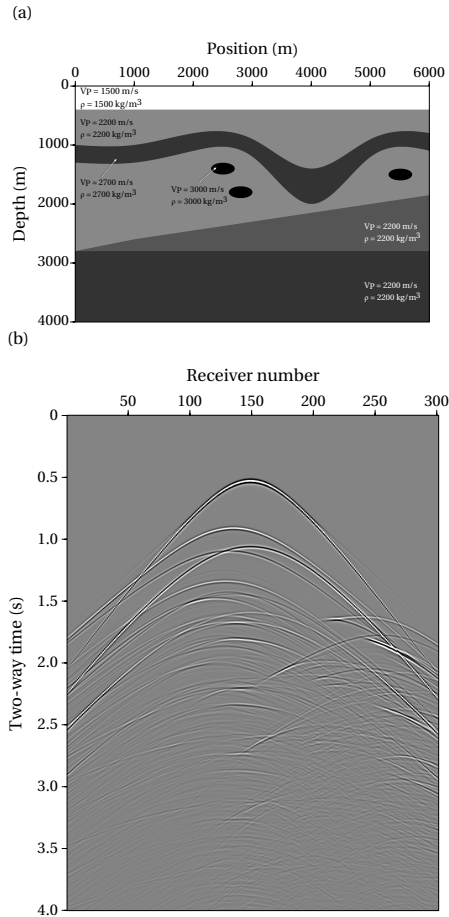


Figure 6.2: (a) Velocity model used to generate the active-source data to test the proposed methodology for data reconstruction. (b) Example of a common-shot gather generated with the velocity model in (a) with the source located at position 3000 m, corresponding to shot number 75 and receiver number 150.

We then create a gap for sources located between 1200 m and 3000 m, which represent approximately 30% of the data. Next, we use these data with a source gap to retrieve SI responses by cross-correlating the common-receiver gathers trace by trace and stacking over all sources. Figure 6.3a shows an example using CMP gather number 393, located at 3920 m with the generated source gap. Figure 6.3b shows the retrieved SI responses for the same CMP gather. The red arrows indicate retrieved pseudo-physical

primary reflections and multiple events, whilst the yellow arrows indicate noises and spurious non-physical events from SI. The latter are stronger for earlier times. Additionally, we can see that we are able to retrieve events until around 3.5 s. As explained in Chapter 5, longer active-source recordings can allow the retrieval of later events in the SI result. Figure 6.4a, Figure 6.4b, and Figure 6.4c show the pre-stack depth migrated images for the complete data, the data with the source gap, and the data with the source gap filled in with the SI responses, respectively. Comparing Figure 6.4a and Figure 6.4b, we can see that the presence of a large gap in the data mainly affects the imaging of the reflectors up to a depth of around 2000 m, and minor effects are noticeable at around 3000 m. In Figure 6.4c we can notice again the noises and spurious events from the SI responses (yellow arrows), but also the events that coincide with those in the active-source data that help have continuity of reflectors (red arrows).

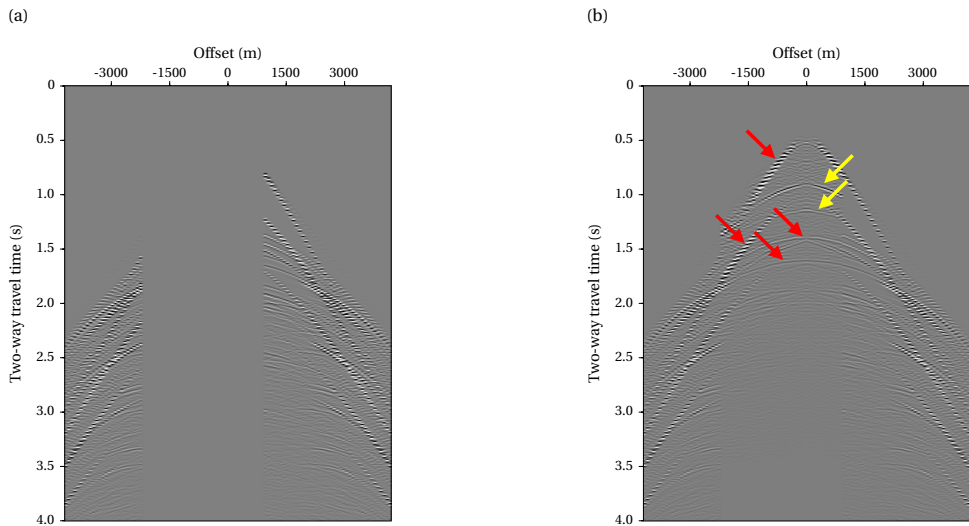


Figure 6.3: (a) Example of a CMP gather located at 3290 m with the generated source gap. (b) The CMP gather in (a) with the source gap filled in with the responses retrieved with SI. The red arrows indicate some retrieved pseudo-physical events that coincide with those in the active-source data. The yellow arrows indicate retrieved non-physical reflections.

Following the proposed methodology, we transform the active-source data with the generated source gap and the SI responses to the Radon domain using HRT. Figure 6.5a, Figure 6.5b, and Figure 6.5c show the HRT for the CMP gather in Figure 6.3 with all the traces, with the generated source gap, and for the responses retrieved through SI, respectively. For this dataset, 40 iterations are enough to obtain an appropriate transform. Comparing Figure 6.5a and Figure 6.5b, it is clear that the presence of the gap creates artefacts and noises in the transformed data. Looking at Figure 6.5c, we can see that various active-source events are retrieved (red arrows), whilst SI spurious events (yellow arrows) and background noises are also present. We then design a filter (Figure 6.6a) using the transformed active-source dataset with the gap (Figure 6.5b) and apply it to the transformed SI responses (Figure 6.5c), obtaining the result shown in Figure 6.6b.

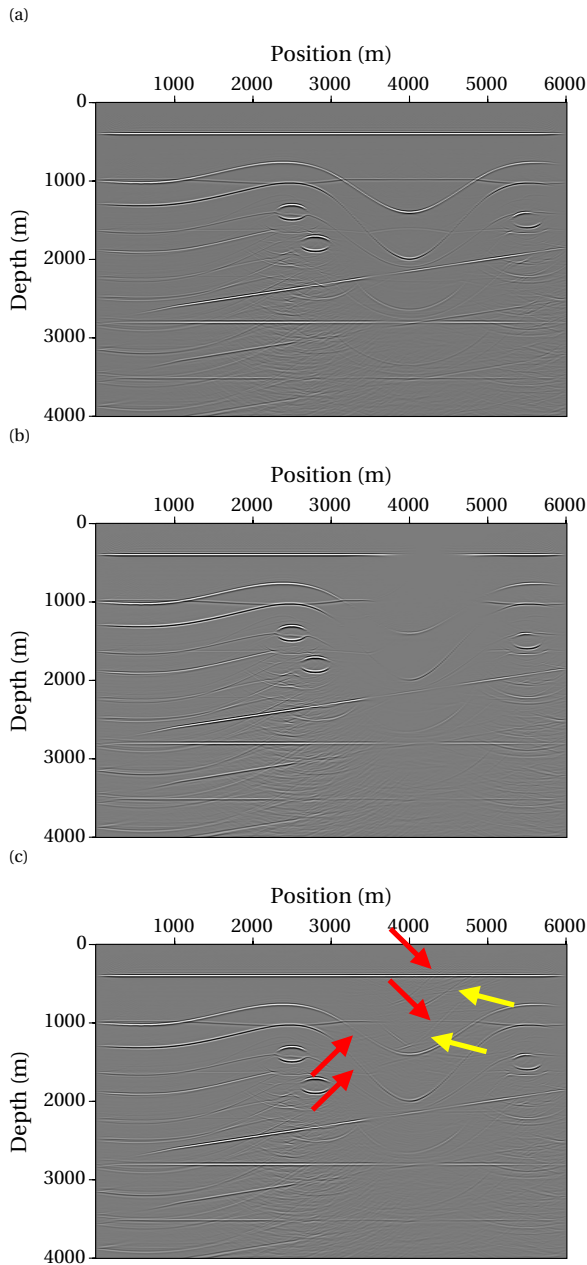


Figure 6.4: (a) Migrated stacked section of the complete dataset. (b) Migrated stacked section of the dataset with the generated source gap. (c) Migrated stacked section of the dataset filled in with the responses retrieved by SI. The red arrows indicate imaged reflector parts that coincide with those in the active-source data. The yellow arrows indicate the imaged non-physical reflectors.

The spurious events and noises are suppressed, for instance, at slower velocities around 1800 m/s (yellow arrows in Figure 6.5c), while pseudo-physical events are preserved (red arrows). Furthermore, the lower-amplitude events between around 1.7 s and 2 s for velocities around 2000 m/s look clearer and sharper.

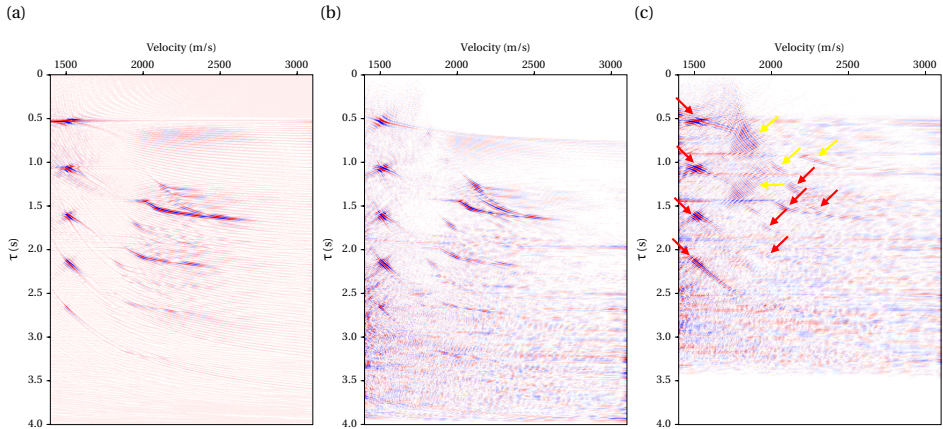


Figure 6.5: (a) HRT of the CMP like in Figure 6.3a but without the source gap. (b) HRT of the CMP in Figure 6.3a with the generated source gap - we can see that the presence of the gap results in artefacts and noises in the transformed data. (c) HRT of the CMP in Figure 6.3b retrieved by SI. The red arrows indicate the pseudo-physical arrivals in the responses retrieved by SI that coincide with the events present in the active-source data. The yellow arrows indicate spurious events retrieved by SI that are removed after masking.

6

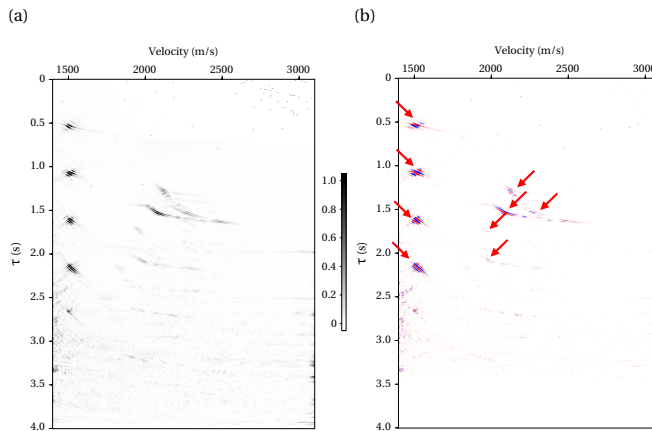


Figure 6.6: (a) Designed filter utilising the HRT of the CMP in Figure 6.5b. (b) Result after masking the HRT of the CMP in Figure 6.5c retrieved by SI utilising (a). The red arrows indicate the pseudo-physical arrivals in the responses retrieved by SI that coincide with the events present in the active-source data, and that still remain after masking.

Subsequently, we transform the masked SI responses back to the time-offset domain. We then use this result to supply the missing traces in the source gap of the active-source

data. [Figure 6.7a](#) shows this result for the CMP gather shown in [Figure 6.3a](#). We can see that the hyperbolic reflection events are well preserved and continuous throughout the gather, whilst noises and spurious events are suppressed.

For comparison, [Figure 6.7b](#) shows the results after applying the conventional HRT interpolation (i.e., transforming the data from the hyperbolic Radon domain to the time-offset domain for the complete geometry). We can observe that the interpolation fails to properly recover some events, while others present some smearing of the wavelet. Better results are obtained when the gap is located at the slopes of the hyperbolic events, where these are nearly linear. However, we can see that it performs poorly to reconstruct the apexes of the hyperbolas or interpolate traces towards the centre of the gap.

Additionally, in order to test the ability of the method to retrieve real information and honour the data, [Figure 6.7c](#) shows the result after applying the masking in the Radon domain to a gather that contains only random noise instead of the SI responses. For this latter case, we can see that energy is retrieved where we expect to have the reflection arrivals, but it does not retrieve a wavelet shape or a continuous event. Consequently, the reflections appear smeared and distorted.

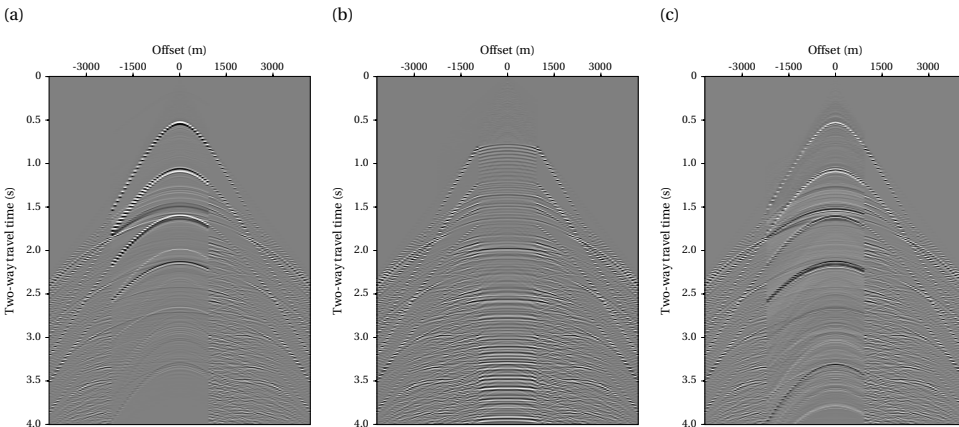


Figure 6.7: (a) CMP gather from [Figure 6.3a](#) with the generated source gap filled in with the SI responses masked in the Radon domain. (b) CMP gather from [Figure 6.3a](#) with the generated source gap after conventional HRT interpolation. (c) CMP gather from [Figure 6.3a](#) with the generated source gap filled in by random noise masked in the Radon domain.

We then apply pre-stack depth migration to the data filled in with the SI responses masked in the Radon domain ([Figure 6.8a](#)), the data after Radon interpolation ([Figure 6.8b](#)), and the data filling in the gap with random noise masked in the Radon domain ([Figure 6.8b](#)), using the velocity model in [Figure 6.2a](#). We can see that the result after using the proposed methodology shows properly reconstructed physical reflectors from the primaries and properly reconstructed reflectors from the multiples (red arrows) whilst removing the spurious reflectors, especially for earlier times. Furthermore, the HRT appears to have brought forward an event that was too weak to be readily interpretable in the retrieved SI responses in the SI responses before masking (green arrow). Looking at [Figure 6.8b](#), we can see that the HRT interpolation performs poorly to recon-

struct the reflectors. We observe that there is some continuity on the sides of the gap, where the interpolation gives a better result. However, it fails towards its centre, where the gap is located at the near offsets in the CMP gathers and the missing traces coincide with the apexes of the hyperbolas from the reflection events. In [Figure 6.8c](#), we can see that noises are present at the positions where we would expect to have imaged reflectors (yellow arrows). This helps illustrate how the methodology honours the responses retrieved by SI, making this a data-driven methodology instead of only mathematical. Additionally, we can see that using the SI responses helps obtain a superior final result.

6.4. FIELD DATA EXAMPLE

In this section, we apply the proposed methodology to a near-surface field dataset acquired in the western part of the Netherlands [\[37\]](#). The area comprises mostly of horizontal soil layers. From borehole measurements, the geology of the area is known to be composed of interchanging clayey and sandy layers from the Holocene, until a depth of 22-25 m. This set of layers is followed by a relatively homogeneous stiff sand of Pleistocene age [\[37\]](#). At the moment of the acquisition, the site was grass-covered with the water table at around 1 m depth [\[37\]](#). An S-wave reflection profile was acquired with roll-along geometry, using 10-Hz horizontal geophones and a sledgehammer as the S-wave source. Both the geophones and the sledgehammer were oriented in the crossline direction, meaning that horizontal S-waves (SH-waves) were recorded (if we assume no 3D scattering). The shot interval was 1 m, and the receiver interval was 0.5 m, with a minimum source-receiver distance at 0.5 m, and a total profile length of 180 m. The data sampling was at 0.5 ms with a record length of 0.5 s. [Table 6.1](#) shows a summary of the acquisition parameters. [Figure 6.9](#) shows three common-shot gathers examples as acquired in the field. We can see strong surface waves that completely obscure any overlapped reflections, also the ones arriving at later times.

| 2D shear-wave seismic reflection profile | |
|--|---|
| S-wave source | Sledgehammer |
| Receivers | 10-Hz horizontal geophones 48 channels |
| Shot interval | 1 m |
| Receiver interval | 0.5 m |
| Minimum source-receiver distance | 0.5 m |
| Data sampling | 0.5 ms |
| Record length | 0.5 s |
| Total profile length | 180 m |

Table 6.1: Summary of the acquisition parameters.

The data are pre-processed following simple conventional seismic processing steps, summarised in [Table 6.2](#). After trace editing, we apply band-pass filtering and spherical divergence compensation. Subsequently, we perform f-k filtering in order to suppress the surface waves. Care is taken while removing as much surface-wave energy as possi-

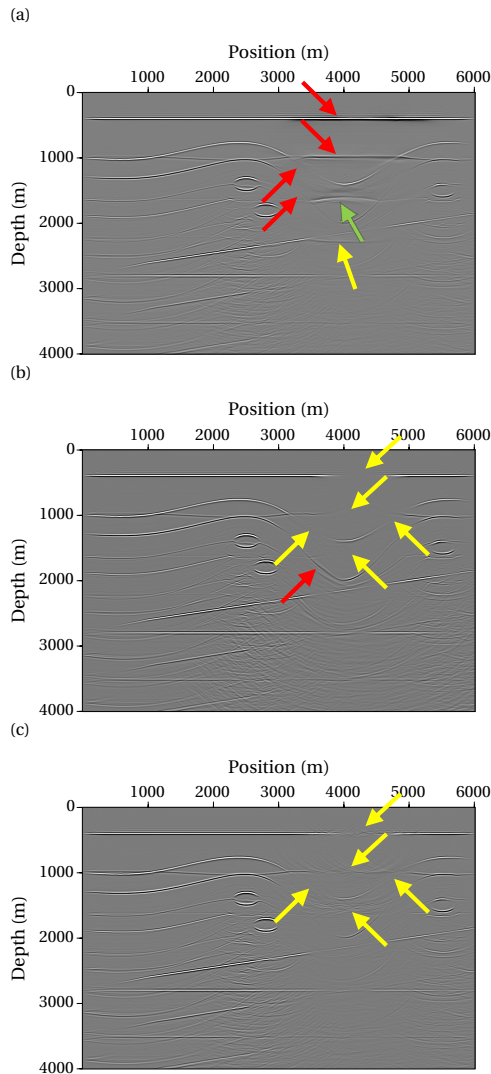


Figure 6.8: (a) Migrated stacked section with the generated source gap filled in with the SI responses masked in the Radon domain. (b) Migrated stacked section after conventional HRT interpolation. (c) Migrated stacked section with the generated source gap filled in with random noise masked in the Radon domain. The red arrows indicate successfully reconstructed physical reflectors and reflectors from multiples that coincide with those in the complete active-source data. The yellow arrows indicate noises and artefacts. The green arrow indicates a weaker event reconstructed by the HRT that was not clearly identifiable in the SI responses.

ble, but without disrupting the amplitudes of the reflection arrivals and trying to minimise undesired artefacts that can arise from the utilisation of such filters. [Figure 6.10](#) exhibits the results after these steps. We can see that surface waves are sufficiently well suppressed, revealing several reflection events represented by hyperbolic arrivals with

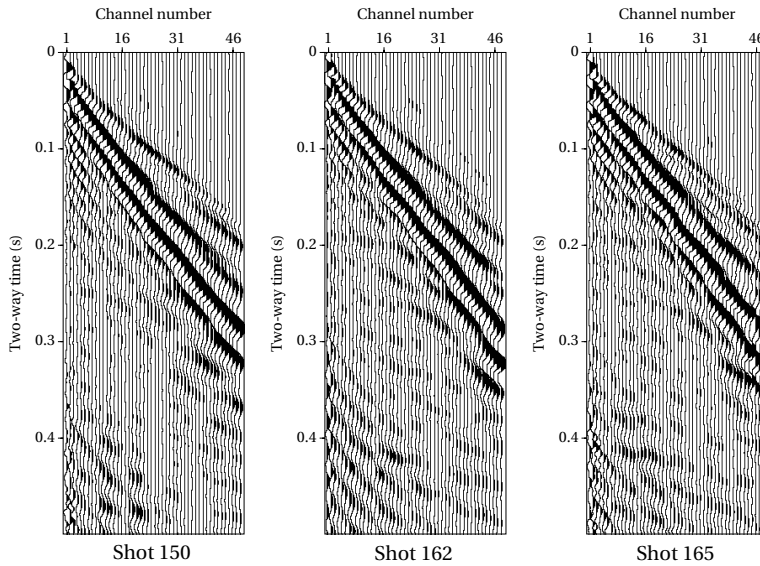


Figure 6.9: Examples of three common-shot gathers as acquired in the field. Strong surface waves can be observed that completely obscure any overlapping reflections, including reflections arriving at later times.

different curvatures at earlier and later times. Nevertheless, linear events can still be observed at the earliest times from surface-wave energy that remains in the data, as well as some high-frequency linear artefacts at later times. The latter could correspond to surface-wave reverberations that can also be observed with lower amplitudes in Figure 6.9 at around 0.3 s or 0.35 s. As shown in Chapters 2 and 3, these linear artefacts could be reduced or avoided by the utilisation of SI surface-wave suppression. However, for the processing of these data, we utilise the SeisSpace ProMAX seismic processing software [38]. Such commercial processing software do not offer yet the possibility of implementing an innovative methodology like SI surface-wave suppression. Thus, for ease of the processing, we utilise f - k filtering since, as also shown in Chapters 2 and 3, it provides sufficiently good results for the purpose of this specific investigation.

In order to test the proposed methodology with these data, we create a large receiver gap between receivers 15 and 30 for each shot, which represents around 30% of the data (Figure 6.11). With the data with the receiver gaps, we perform SI by cross-correlation. Figure 6.12 shows the retrieved SI responses for the common-shot gathers in Figure 6.11 after applying top-mute and AGC for plotting. The red arrows indicate various pseudo-physical reflections that coincide with events present in the active-source data. These can potentially help to supply the missing traces in the data with the receiver gaps, enhancing the final result. Nevertheless, artefacts are also present, which are more prominent for this SI result than the ones obtained for the numerically modelled example. This is in part due to the fact that the land field data also contain noises, and direct- and surface-wave arrivals that are not completely suppressed. These events are then also retrieved in the SI results. In the preceding example, these events are not consid-

| Step | Instruction |
|----------------------|-----------------------------------|
| Pre-stack processing | |
| 1 | Set and apply geometry |
| 2 | Trace editing |
| 3 | Band-pass filtering |
| 4 | Spherical-divergence compensation |
| 5 | Trace balancing |
| 6 | F-k filtering |
| 7 | Spiking deconvolution |
| 8 | Sort to CMP domain |
| 9 | Velocity analysis |
| 10 | NMO correction |
| 11 | AGC |
| 12 | Top- and bottom-mute |
| 13 | CMP/ensemble stack |

Table 6.2: Summary of steps applied to process the near-surface seismic reflection data in order to obtain the final stacked sections.

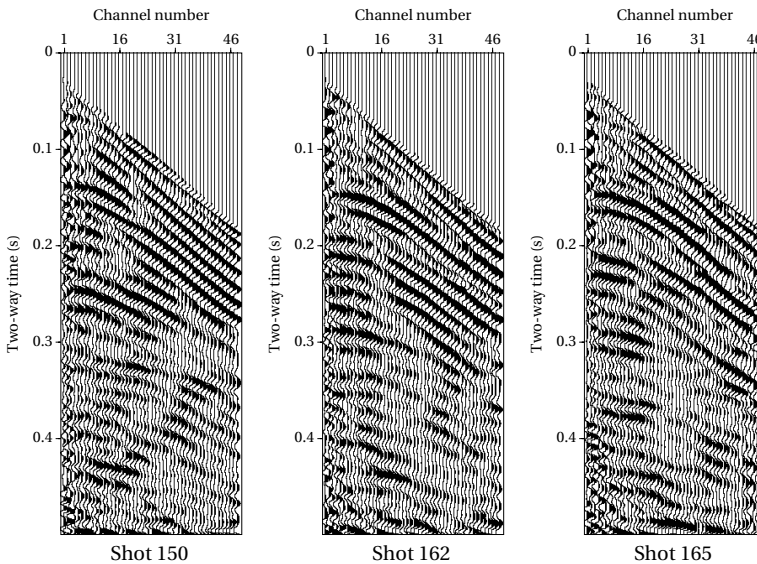


Figure 6.10: Common-shot gathers from Figure 6.9 after applying f-k filtering in order to suppress the surface-wave energy. We can see that the surface waves are sufficiently well suppressed after this step, and different reflection events are now unveiled at earlier and later times.

ered. Thus, as we can see in Figure 6.12, this poses an extra challenge for the retrieval of pseudo-reflection events in the SI responses, but also for the suppression of the spu-

rious events. Nevertheless, we expect that the SI result will still present improvements after filtering the data in the HRT domain.

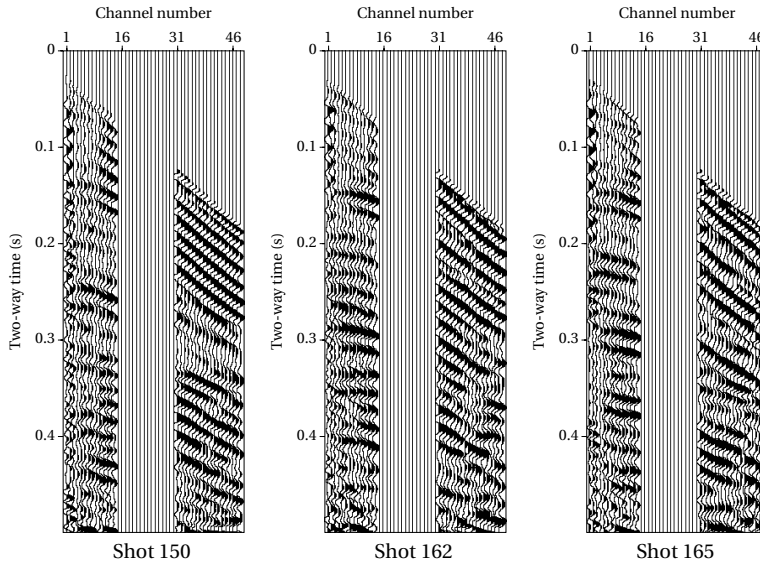


Figure 6.11: Common-shot gathers from Figure 6.10 with the generated receiver gap between receivers 15 and 30 for each shot.

Next, we apply spiking deconvolution to both the field data and the responses retrieved by SI in order to compress the source wavelet and gain temporal resolution. Finally, the last pre-processing steps consist of applying AGC followed by top- and bottom-mute. Figure 6.13, Figure 6.14, and Figure 6.15 show the three common-shot gathers after applying these processing steps to the complete dataset, the dataset with the receiver gap, and the responses retrieved by SI, respectively. In Figure 6.13 and Figure 6.14 we can see that now the reflections look sharper and more continuous. The previously mentioned linear artefacts that are present at the later times can be observed as well. In Figure 6.15, we can see that the spiking-deconvolution step not only helps with the sharpness and continuity of the events, but also compensates for the different wavelets and removes the ringing present in the SI responses. Thus, the pseudo-physical reflections that are successfully retrieved (red arrows) can now be better appreciated. We can see that the flatter arrivals present in the active-source data at later times (from around 0.3 s in Figure 6.13) appear to be retrieved as well. However, they exhibit much less continuity and lower amplitudes. As mentioned in the previous section, superior results for later times could be achieved with the availability of longer recordings in time, since the presence of multiple events (that arrive at later times) are necessary for the SI retrieval of pseudo-physical reflections at later times.

Following our proposed methodology, we sort the data in CMP gathers and then transform the CMP gathers to the Radon domain using HRT. The CMP spacing is 0.25 m, with a maximum fold of 12 traces. For this dataset, 100 iterations are enough to ob-

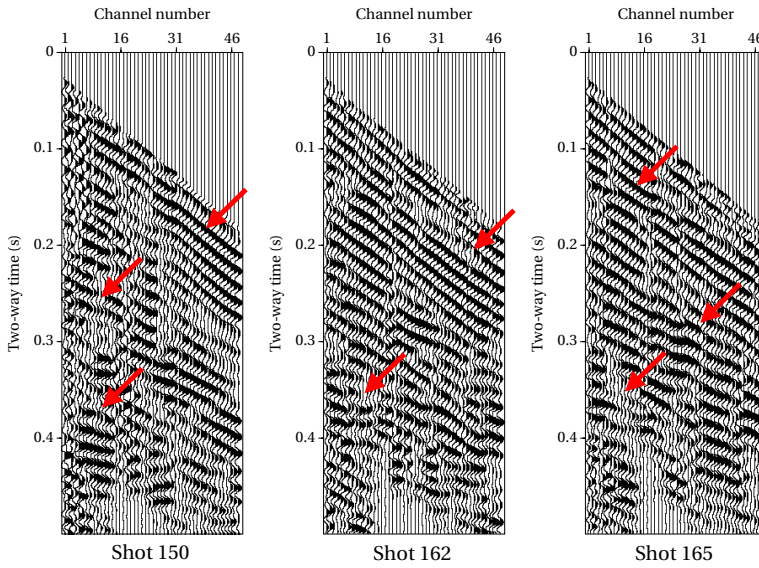


Figure 6.12: Virtual common-shot gathers retrieved by SI for the common-shot gathers in Figure 6.11. The red arrows indicate various pseudo-physical reflections, equivalents to which are also present in the field common-shot gathers. Artefacts and ringing are also present.

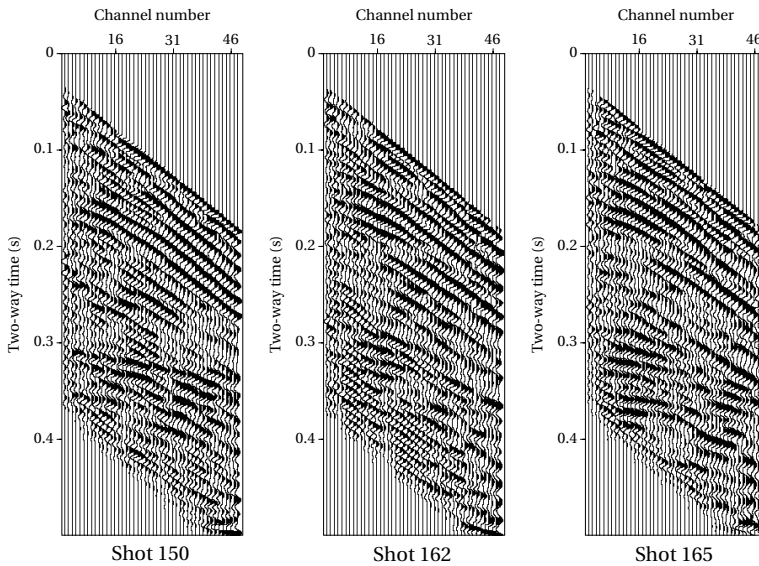


Figure 6.13: Common-shot gathers from Figure 6.10 after applying spiking deconvolution and top- and bottom-mute.

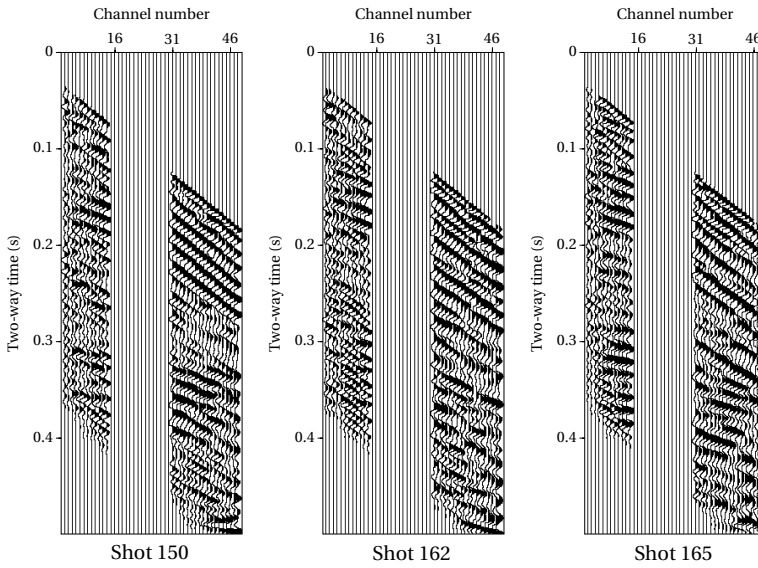


Figure 6.14: Common-shot gathers from Figure 6.11 after applying spiking deconvolution and top- and bottom-mute.

6

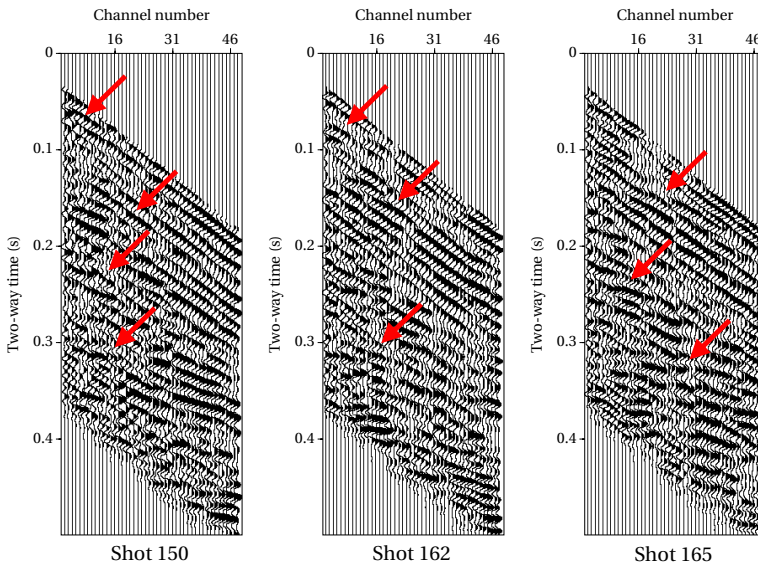


Figure 6.15: Virtual common-shot gathers retrieved by SI from Figure 6.12 after applying spiking deconvolution and top- and bottom-mute.

tain an appropriate transform that reproduces the data with accuracy. Figure 6.16a and Figure 6.16b show an example of the HRT for CMP gather number 670 for the complete

dataset and the dataset with the receiver gap, respectively. As expected for the field data, it is harder to separate and properly focus the seismic events. Additionally, in spite of having several sets of events that present the same τ (zero-offset two-way travel time) and velocity in both panels, comparing these two results we can observe that the presence of the gap generates artefacts and noises in the transformed data. Some events have clearly different shapes and curvatures, and others appear to not be mapped (e.g., around $\tau = 0.2$ s). [Figure 6.16c](#) shows the HRT for the SI responses retrieved for the same CMP gather. Comparing it with [Figure 6.16a](#), we can see some events retrieved by SI that coincide in shape, τ , and velocity with the events present in the active-source data (red arrows). Still, spurious events (non-physical reflections) can also be observed, as well as artefacts, which are present in particular towards lower velocities. [Figure 6.16d](#) shows the result after masking the SI responses in [Figure 6.16c](#), utilising the HRT in [Figure 6.16b](#) to create the filter. Now, we can observe more similarity between this result and the complete active-source data panel ([Figure 6.16a](#)). Several artefacts are removed, whilst the pseudo-physical reflections that correspond to physical reflections in the active-source data are preserved (red arrows).

Finally, we transform the masked SI responses back to the time-offset domain. We then use this enhanced result to fill in the missing traces in the generated receiver gaps. [Figure 6.17](#) shows this result for the same three common-shot gathers as in [Figure 6.14](#). Indicated with red arrows, we can see several events that are well recovered and continuous after this processing. Once more, we can see that events at later times are difficult to reconstruct since they are hard to retrieve by SI.

For comparison, we interpolate the active-source data with the gap ([Figure 6.14](#)) utilising the conventional HRT interpolation (i.e., by transforming the data with the source gap back to the time-offset domain for the complete offset). This result is shown in [Figure 6.18](#). Here, we can observe that the results appear to exhibit continuity for some events, indicated with red arrows. However, some of these correspond to the previously mentioned linear artefacts. Overall, the result appears to have high noise content and, for most events, the method fails to successfully reconstruct the missing reflection information.

After this process, we perform velocity analysis of the data. We then create a 2D velocity model, and use it to apply NMO corrections and stack the data. [Figure 6.19a](#) and [Figure 6.19b](#) show the stacked sections for the complete dataset and the dataset with the generated receiver gaps, respectively, for CMP numbers 570 to 712. Because the CMP interval is 0.25 m, the total extent of the shown stacked sections is 35.25 m. Several nearly horizontal reflectors are visible, and some are almost continuously imaged throughout the entire length of the seismic sections. The shallower strongest set of reflectors at around 0.15 s are interpreted to correspond to the Holocene sand-clay boundaries, whilst the lower set of reflectors at around 0.3 s correspond to the Holocene-Pleistocene boundary [37].

Comparing the results in [Figure 6.19a](#) and [Figure 6.19b](#), we can observe in the final image the impact of having relatively large receiver gaps in our data. Overall, the same reflectors are imaged in both results. However, the reflectors in [Figure 6.19b](#) suffer from loss of amplitude, sharpness, and continuity due to the receiver gaps. The yellow arrows in [Figure 6.19b](#) indicate particular areas where these reflectors have lost continuity. We

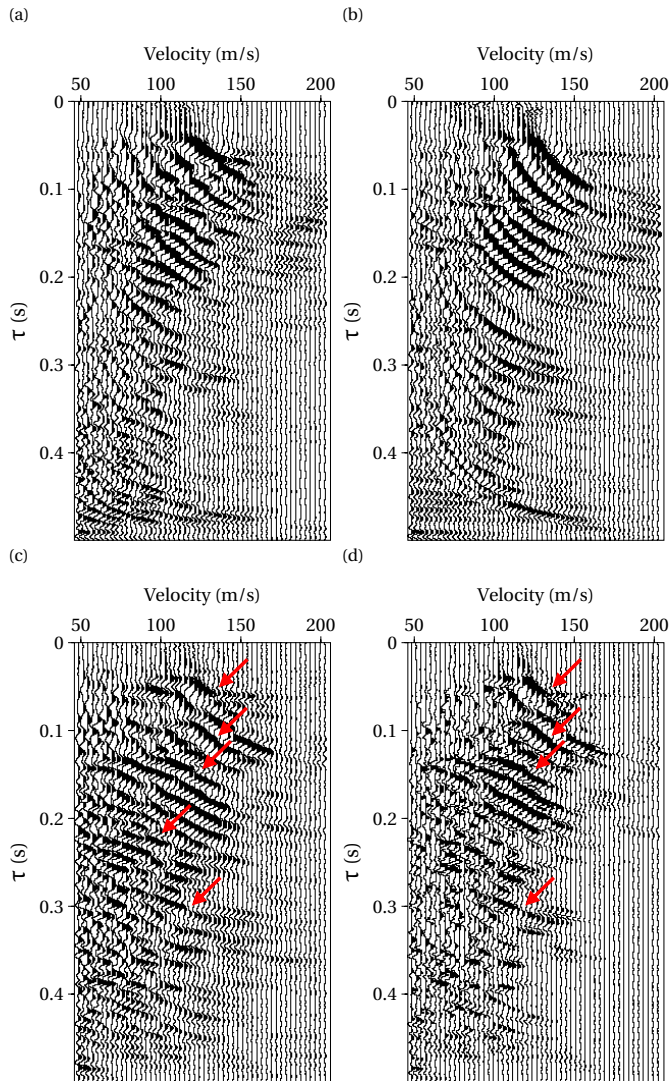


Figure 6.16: (a) HRT for CMP number 670. (b) HRT for CMP number 670 with the generated source gap - we can see that the presence of the gap results in artefacts and noises in the transformed data. (c) HRT of CMP number 670 retrieved by SI. (d) Result after masking (c) utilising (b) to create the filter. The red arrows indicate the pseudo-physical reflections in the responses retrieved by SI that coincide with the events present in the active-source data and still remain after masking.

can see that linear artefacts dipping towards the right side of the section are present in both results (red arrows). Still, they appear more frequently and stronger in the presence of the receiver gaps. Additionally, the area with less reflectivity between approximately 0.19 s and 0.3 s is harder to image due to the increased noise content and lower amplitudes.

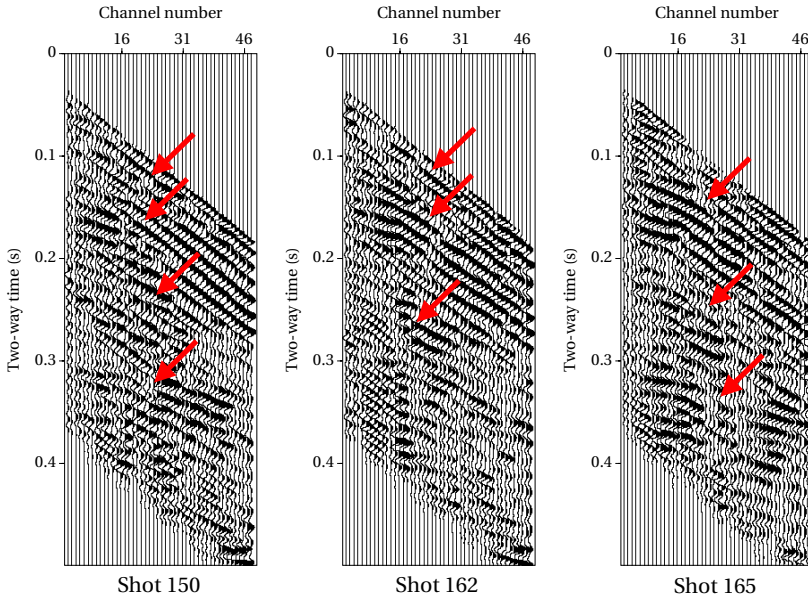


Figure 6.17: Common-shot gathers from Figure 6.14 after filling in the gap with the masked SI responses.

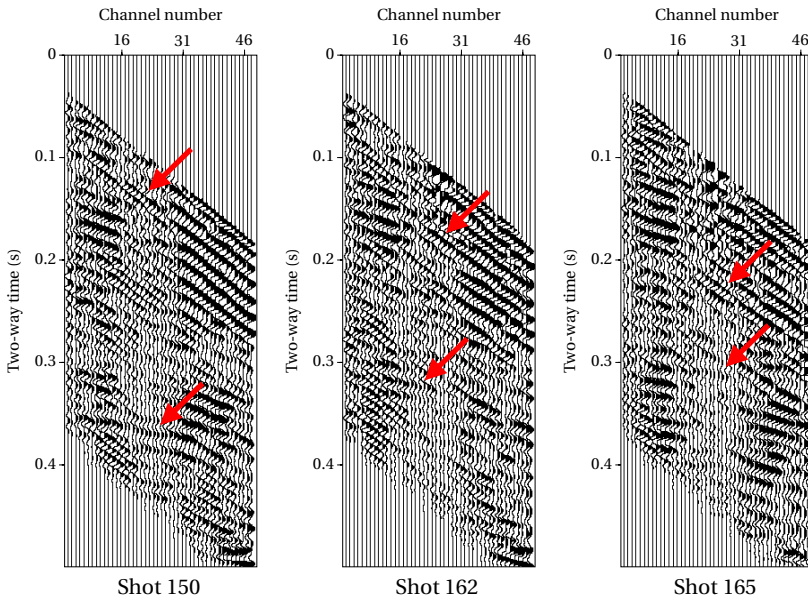


Figure 6.18: Common-shot gathers from Figure 6.14 after HRT interpolation.

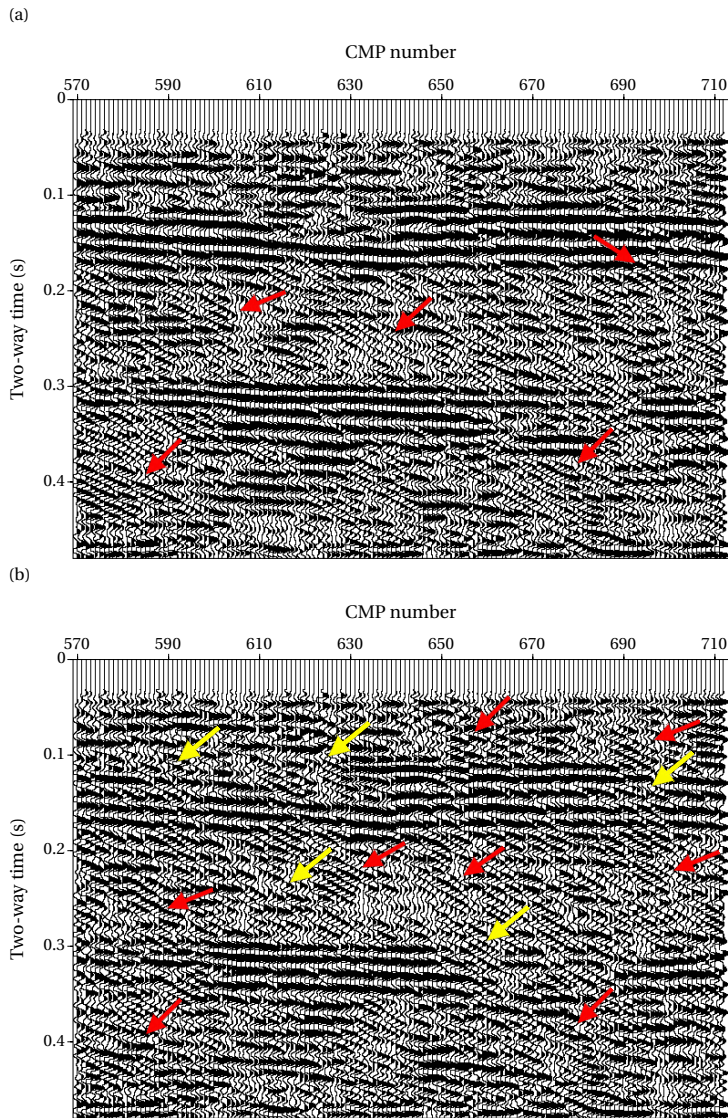


Figure 6.19: (a) Stacked section of the complete dataset. (b) Stacked section of the dataset with the generated receiver gap. The red arrows point out linear artefacts that are stronger for the result with the receiver gap. The yellow arrows indicate some areas where there is a lack of continuity in the reflectors due to the presence of the receiver gap.

Figure 6.20a shows the stacked section for the dataset with the receiver gap filled in with the SI responses masked in the Radon domain. The red and yellow arrows indicate some of the strong linear artefacts that remain in the data and areas where the reflectors still show discontinuity, respectively. Nevertheless, after this process, the reflectors

appear overall more continuous, especially for earlier times. The green arrows indicate events that were successfully recovered. Additionally, we can observe that several reflectors are retrieved in the low-reflectivity area between approximately 0.19 s and 0.3 s. However, as expected, events at later times are hard to recover.

Figure 6.20b shows the stacked section for the dataset with the generated receiver gap after HRT interpolation. Once more, the yellow arrows point out areas where the reflectors are still discontinuous, whilst the red arrows indicate the linear artefacts present in the stacked section. We can see that this method is mostly unsuccessful in recovering new information that could help improve the final result. Overall, it is hard to recognise enhancements in this stacked section. Similar to the results for the previous section, the HRT fails to reconstruct events for relatively large gaps, even though for this geometry the gap is chosen always for the same channel numbers. These channel numbers are located in the middle of the receiver array, thus maintaining the apexes of the hyperbolas of the active-source data. Comparing the results in Figure 6.20, we can see that by utilising SI we can provide a superior result for interpolation of relatively large gaps. As previously mentioned, in spite of not being a replacement for well-sampled field data, SI contributes with additional information that allows a superior reconstruction of the events.

6.5. CONCLUSIONS

Current methods for seismic interpolation work well when interpolating data with uniformly or randomly missing traces, but they perform poorly for the case of large gaps. To address this problem, we introduced a new approach for data reconstruction utilising SI. We showed that SI can provide new seismic responses to supply missing traces inside large gaps in the data. Due to reciprocity, both virtual receivers and virtual sources could be retrieved. These estimates can provide additional information when such data are not available. Additionally, the new SI responses are retrieved in a purely data-driven manner and no knowledge of the subsurface characteristics is required.

In order to suppress artefacts and spurious events retrieved by SI, we filtered these responses in the Radon domain using HRT, taking advantage of the ability of this transform to focus and separate seismic events. These filtered responses provided a more suitable result to supply the missing traces in the data. This filter was designed utilising the HRT of the active-source data with missing traces. Its accuracy depends, thus, on the ability of the HRT to focus and separate the seismic events. Nevertheless, this methodology resulted in a very simple and practical procedure.

We applied the developed methodology to numerically modelled data and to a near-surface field dataset. For the latter case, as expected, the responses retrieved with SI contained more noises and artefacts. Additionally, the seismic events were less clear and focused in the Radon domain than for the numerically modelled data example. Nevertheless, pseudo-physical reflections were successfully retrieved and some noises and artefacts were well suppressed after filtering. The result utilising the conventional HRT interpolation showed that this method fails to reconstruct the events when the data present a relatively large gap. This result helped validate the effectiveness of our methodology for data reconstruction inside large gaps in land data. We showed that, in spite of not being a substitute for well-sample field data, our methodology allowed us to obtain a

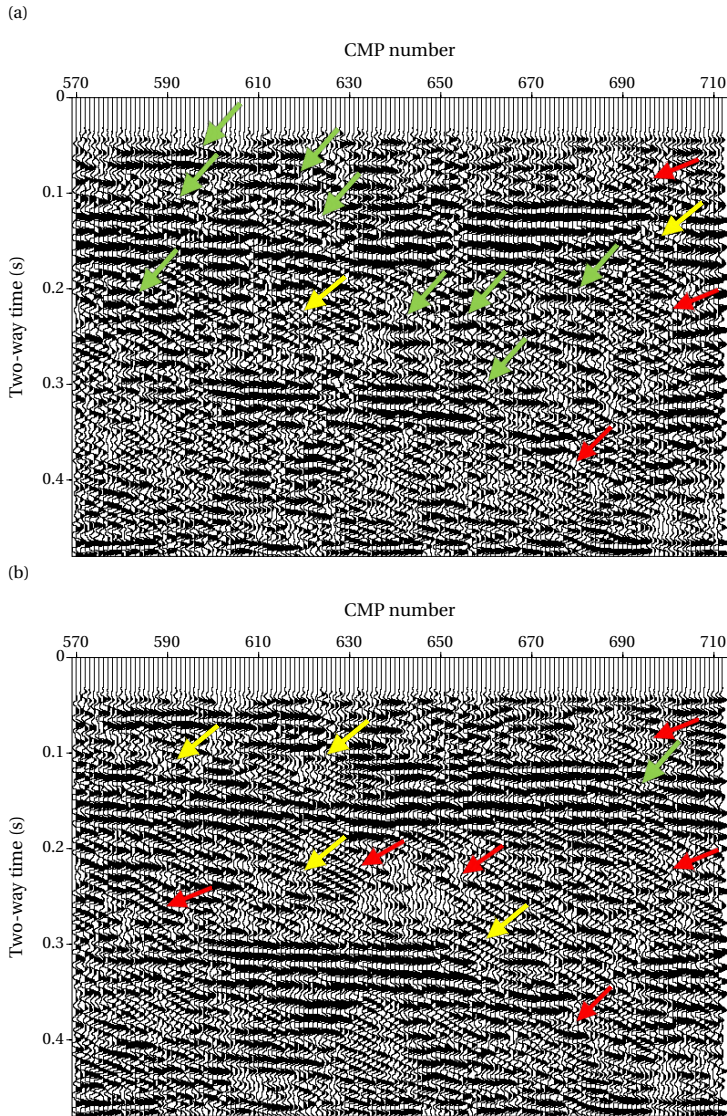


Figure 6.20: (a) Stacked section of the dataset with the generated receiver gap filled in with the masked SI responses in the Radon domain. (b) Stacked section of the dataset with the generated receiver gap after RT interpolation. The red arrows point out linear artefacts that remain strong for both images. The yellow arrows indicate areas in the reflectors where there is still lack of continuity.

better image of the subsurface, thus helping improve the data processing and final result.

REFERENCES

- [1] S. Spitz, *Seismic trace interpolation in the F-X domain*, *Geophysics* **56**, 785 (1991).

- [2] M. Naghizadeh and M. D. Sacchi, *Multistep autoregressive reconstruction of seismic records*, *Geophysics* **72**, V111 (2007).
- [3] M. Naghizadeh and M. Sacchi, *Seismic data reconstruction using multidimensional prediction filters*, *Geophysical Prospecting* **58**, 157 (2010).
- [4] J. Claerbout and S. Fomel, *Image Estimation by Example: Geophysical soundings image construction: Multidimensional autoregression* (<http://sepwww.stanford.edu/sep/prof/gee8.08.pdf>, 2006).
- [5] S. Fomel, *Seismic reflection data interpolation with differential offset and shot continuation*, *Geophysics* **68**, 733 (2003).
- [6] S. T. Kaplan, M. Naghizadeh, and M. D. Sacchi, *Data reconstruction with shot-profile least-squares migration*, *Geophysics* **75**, WB121 (2010).
- [7] S. Xu, Y. Zhang, D. Pham, and G. Lambaré, *Antileakage Fourier transform for seismic data regularization*, *Geophysics* **70**, V87 (2005).
- [8] R. Abma and N. Kabir, *3D interpolation of irregular data with a POCS algorithm*, *Geophysics* **71**, E91 (2006).
- [9] F. J. Herrmann and G. Hennenfent, *Non-parametric seismic data recovery with curvelet frames*, *Geophysical Journal International* **173**, 233 (2008).
- [10] G. Hennenfent, L. Fenelon, and F. J. Herrmann, *Nonequispaced curvelet transform for seismic data reconstruction: A sparsity-promoting approach*, *Geophysics* **75**, WB203 (2010).
- [11] M. Naghizadeh and M. D. Sacchi, *Beyond alias hierarchical scale curvelet interpolation of regularly and irregularly sampled seismic data*, *Geophysics* **75**, WB189 (2010).
- [12] D. O. Trad, T. J. Ulrych, and M. D. Sacchi, *Accurate interpolation with high-resolution time-variant Radon transforms*, *Geophysics* **67**, 644 (2002).
- [13] A. Ibrahim, P. Terenghi, and M. D. Sacchi, *Simultaneous reconstruction of seismic reflections and diffractions using a global hyperbolic Radon dictionary*, *Geophysics* **83**, V315 (2018).
- [14] J. R. Thorson and J. F. Claerbout, *Velocity-stack and slant-stack stochastic inversion*, *Geophysics* **50**, 2727 (1985).
- [15] D. J. Verschuur and A. J. Berkhout, *Transforming multiples into primaries: experience with field data*, in *SEG Technical Program Expanded Abstracts 2005* (Society of Exploration Geophysicists, 2005).
- [16] A. J. Berkhout and D. J. Verschuur, *Imaging of multiple reflections*, *Geophysics* **71**, SI209 (2006).
- [17] W. Curry and G. Shan, *Interpolation of near offsets using multiples and prediction-error filters*, *Geophysics* **75**, WB153 (2010).

- [18] G. Schuster, *Seismic interferometry* (Cambridge University Press, Cambridge, 2009).
- [19] Y. Wang, Y. Luo, and G. T. Schuster, *Interferometric interpolation of missing seismic data*, *Geophysics* **74**, SI37 (2009).
- [20] Y. Wang, S. Dong, and Y. Luo, *Model-based interferometric interpolation method*, *Geophysics* **75**, WB211 (2010).
- [21] S. M. Hanafy and G. T. Schuster, *Interferometric interpolation of sparse marine data*, *Geophysical Prospecting* **62**, 1 (2013).
- [22] K. Wapenaar, D. Draganov, R. Snieder, X. Campman, and A. Verdel, *Tutorial on seismic interferometry: Part 1 — Basic principles and applications*, *Geophysics* **75**, 75A195 (2010).
- [23] D. F. Halliday, A. Curtis, P. Vermeer, C. Strobbia, A. Glushchenko, D.-J. van Manen, and J. O. Robertsson, *Interferometric ground-roll removal: Attenuation of scattered surface waves in single-sensor data*, *Geophysics* **75**, SA15 (2010).
- [24] D. Trad, M. Sacchi, and T. Ulrych, *A hybrid linear-hyperbolic radon transform*, *Journal of Seismic Exploration* **9**, 303 (2001).
- [25] D. Trad, T. Ulrych, and M. Sacchi, *Latest views of the sparse Radon transform*, *Geophysics* **68**, 386 (2003).
- [26] M. Hestenes and E. Stiefel, *Methods of conjugate gradients for solving linear systems*, *Journal of Research of the National Bureau of Standards* **49**, 409 (1952).
- [27] M. D. Sacchi and M. Porsani, *Fast high resolution parabolic radon transform*, in *SEG Technical Program Expanded Abstracts 1999* (Society of Exploration Geophysicists, 1999).
- [28] A. Ibrahim and M. D. Sacchi, *Simultaneous source separation using a robust radon transform*, *Geophysics* **79**, V1 (2014).
- [29] D. Mikesell, K. van Wijk, A. Calvert, and M. Haney, *The virtual refraction: Useful spurious energy in seismic interferometry*, *GEOPHYSICS* **74**, A13 (2009).
- [30] D. Draganov, R. Ghose, E. Ruigrok, J. Thorbecke, and K. Wapenaar, *Seismic interferometry, intrinsic losses and Q-estimation*, *Geophysical Prospecting* **58**, 361 (2010).
- [31] D. Draganov, R. Ghose, K. Heller, and E. Ruigrok, *Monitoring changes in velocity and q using non-physical arrivals in seismic interferometry*, *Geophysical Journal International* **192**, 699 (2012).
- [32] D. Draganov, K. Heller, and R. Ghose, *Monitoring CO2 storage using ghost reflections retrieved from seismic interferometry*, *International Journal of Greenhouse Gas Control* **11**, S35 (2012).
- [33] S. King and A. Curtis, *Suppressing nonphysical reflections in green's function estimates using source-receiver interferometry*, *Geophysics* **77**, Q15 (2012).

- [34] B. Boullenger and D. Draganov, *Interferometric identification of surface-related multiples*, *Geophysics* **81**, Q41 (2016).
- [35] J. Place and A. Malehmir, *Using supervirtual first arrivals in controlled-source hardrock seismic imaging—well worth the effort*, *Geophysical Journal International* **206**, 716 (2016).
- [36] J. W. Thorbecke and D. Draganov, *Finite-difference modeling experiments for seismic interferometry*, *Geophysics* **76**, H1 (2011).
- [37] R. Ghose and J. Goudswaard, *Integrating s-wave seismic-reflection data and cone penetration test data using a multiangle multiscale approach*, *Geophysics* **69**, 440 (2004).
- [38] H. Landmark, *SeisSpace ProMAX*, <https://www.landmark.solutions/SeisSpace-ProMAX>.

7

CONCLUSIONS AND RECOMMENDATIONS

This chapter will conclude this thesis by summarising the main contributions in relation to the research objectives. It will also present recommendations for future research.

7.1. CONCLUSIONS

The main aim of this thesis was to investigate the applicability of seismic interferometry (SI) for data processing.

In Chapter 2, we presented the processing procedure of interferometric surface-wave suppression. We applied this method for the processing of the seismic dataset acquired for exploration of the iron-oxide mineralisation zone in Blötberget, in the Ludvika mining area, south-central Sweden. After applying SI, we obtained estimates of the surface waves that represent the surface waves in the field data. Subsequently, we adaptively subtracted these estimates from the original shot gathers. This method successfully suppressed the surface waves in the data. We then compared the result after SI surface-wave suppression with the results after utilising band-pass filtering and frequency-wavenumber (f-k) filtering. This comparison validated the effectiveness of our methodology since the SI surface-wave suppression allowed us to obtain a cleaner dataset, avoiding potential artefacts that such filters can produce. Our result provided a stacked section with enhanced resolution of the reflectors from the mineralisation zone, and with higher signal-to-noise ratio after simple processing steps and imaging. Furthermore, this study showed the value of legacy data and how they can be optimally reprocessed using new seismic-processing techniques in order to allow the generation of possible new mineral targets.

In Chapter 3, we processed a second dataset acquired for exploration of the mineralisation in the Siilinjärvi mine, eastern Finland. Once more, we retrieved surface-waves estimates by applying SI and subsequently adaptively subtracted them from the field data. After this processing, surface waves were suppressed, as well as some other coherent noises and energy from the air waves. In addition, we applied f-k filtering to the data in order to compare these results with the proposed methodology. In spite of also providing a suitable surface-wave suppression, low-frequency ringing from the surface waves was still present. After careful processing, we obtained migrated stacked sections

of the data. It could be observed then that the area consists of a very complex reflectivity setting, comprising several sub-horizontal reflectors and sub-vertical contacts. We could see that the result after applying SI surface-wave suppression helped improve the following processing steps, allowing to obtain clearer and more continuous reflectors for shallower and deeper structures. The result after applying this methodology also exhibited a sharper boundary between the mineralisation complex and the surrounding bodies. The result after applying f-k filtering provided a poorer image with higher noise content. Whilst the use of such filters can harshly affect the frequencies, damaging the amplitudes of the data, we showed that the utilisation of SI surface-wave suppression had much less impact on these parameters.

In Chapter 4, we extended the application of the interferometric suppression of a specific wave-type from seismic wavefields to electromagnetic wavefields. Here, we applied electromagnetic interferometry to ground penetrating radar (GPR) field data to obtain a direct-wave estimate to then adaptively subtract it from the field data. We applied this methodology to data acquired in the Jewish Cemetery in Naaldwijk, The Netherlands. After this processing, the direct wave was well suppressed, allowing to unveil the earliest diffraction arrivals in the time sections. Hence, the shallowest events could be better appreciated and defined in the time slices. The results obtained after utilising the classic methodology of background removal also showed a successful direct-wave suppression. However, we observed that this methodology affects the shapes of the hyperbolic events and strongly removes horizontal and sub-horizontal features throughout the entire time sections. Comparison with this result helped validate the effectiveness of the proposed methodology. The survey revealed anomalies where buried (pieces of) tombstones might be present. Root patterns were clearly visible in the time slices, which also served to demonstrate the applicability of the GPR survey to detect shallow features.

In Chapter 5, we proposed a methodology for seismic data reconstruction using SI. This methodology consists of retrieving SI responses to supply missing traces in relatively large source gaps in the data. Following, a projection-onto-convex-sets (POCS) image-restoration algorithm is applied to more suitably merge both datasets. We first applied the proposed methodology to numerically modelled data. We showed that reflections in the active-source data could be retrieved utilising SI. However, noises and spurious events were also present. Nevertheless, we observed clear improvements when utilising SI responses to fill in the source gap prior to utilising the POCS interpolation algorithm compared with the results after utilising the POCS interpolation algorithm on the data with the source gap. Next, we applied the proposed methodology to the field data acquired at the Ludvika mines of Sweden. As expected, it was harder to precisely recover the active-source reflections when we applied SI to these highly-noisy data. This also increased the difficulty for the interpolator to reconstruct the missing events. Nevertheless, comparing with the stacked section obtained after interpolating the data with a large source gap, our results still exhibited improvements and showed more continuity of the reflectors from the mineralisation zone.

In Chapter 6, we introduced a new approach for data reconstruction utilising SI. We showed that both virtual sources and virtual receivers can be retrieved to this end. In order to suppress artefacts and spurious events retrieved in the SI responses, we proposed to filter the SI responses in the Radon domain using the hyperbolic Radon transform

(HRT). After applying HRT to the active- and virtual-source data, we design a filter utilising the HRT of each active-source CMP gather. This filter is then applied to the respective virtual-source CMP gather. The accuracy depends on the ability of the HRT to focus and separate the seismic events, also when the data have a relatively large gap. Nevertheless, this methodology results in a very simple and practical procedure. Firstly, we applied the proposed methodology to numerically modelled data. The results showed that spurious events and noises were well suppressed, while pseudo-physical events were preserved. For comparison, we showed the results for the conventional HRT interpolation (i.e., transforming the data from the hyperbolic Radon domain to the time-offset domain for the complete geometry). We observed that this method fails to properly recover some events, especially when the gap was located at the apexes of the hyperbolic reflections, thus when these exhibited more pronounced curvature. Next, we applied the methodology to a near-surface dataset acquired in the western part of The Netherlands. The retrieved SI responses presented noises and spurious events, which were more pronounced due to noises in the active-source data, the presence of a large receiver gap and surface-wave energy that was not completely suppressed. We could observe then that seismic events were less clear and focused in the Radon domain. Nevertheless, after filtering in the Radon domain, some active-source events were successfully preserved whilst noises and spurious events were suppressed. Once more, we showed that the utilisation of the HRT interpolation fails to reconstruct events when the data present relatively large gaps. After processing and imaging, we showed that our result exhibited improvements when comparing it with the results for the data with gap and the data after HRT interpolation.

Thus, this thesis:

- Illustrated the potential of the application of seismic methods and novel processing methodologies in the exploration of hard-rock mining targets and the near surface.
- Showed that the seismic-interferometric surface-wave suppression method is a simple and successful tool for denoising. This method helped enhance the processing of the different datasets to which it was applied, obtaining improved images of the subsurface and the target area.
- Showed that SI responses can be used to supply additional traces; this could help fulfil the demand for dense and regular sampling when such data are not available, in particular when there are relatively large gaps in the data. Using SI responses to fill in the missing traces, better data preconditioning is achieved, allowing processing techniques to provide a superior result and obtain higher-resolution images of the subsurface.
- Extended the application of the interferometric suppression of surface waves to the suppression of electromagnetic direct waves in GPR recordings; this method also resulted in a successful tool for denoising, showing clearer time sections and time slices where shallower features were better identified.
- Further consolidated the application of interferometric methods for data processing; this contributes to the development of cost-effective and environmentally

friendly tools and methods for geophysical exploration since by applying SI, new responses from virtual sources are retrieved with no extra field acquisition cost or requirements, just by data reprocessing.

7.2. RECOMMENDATIONS

SCATTERED SURFACE WAVES AND SUPER-VIRTUAL INTERFEROMETRY

In Chapters 2 and 3, we showed that direct (interreceiver) surface waves can be estimated using SI by cross-correlation of the data observed at different receiver locations and subsequent summation over the sources. However, near-surface heterogeneities can cause surface waves to be scattered in the crossline direction. These scattered surface waves can be particularly difficult to suppress due to their time-varying directions. Thus, it may be desirable to recover these scattered surface waves using SI in order to subsequently remove them from the field data. By splitting the surface waves into direct and scattered parts, Halliday and Curtis [1] applied a stationary-phase analysis and found that the scattered surface waves can be estimated by correlating or convolving the direct surface waves at the virtual source with the scattered surface waves at the second receiver. Halliday *et al.* [2] developed a workflow for the prediction of the scattered surface waves by applying both correlation-type and convolution-type SI, and subsequently adaptively subtracting them from the source-receiver recordings. These authors first separate the surface waves into two parts, one part approximating the direct surface waves, and another approximating the scattered surface waves. The direct surface waves are isolated using f-k and frequency-space (f-x) filters and time windowing. All data identified as not being scattered surface waves (i.e., the direct surface-wave estimates previously isolated from the data and any arrivals prior to the first arrival time of the direct surface wave) are then removed, isolating the scattered surface waves. Subsequently, SI by cross-correlation or convolution is applied between the direct surface waves at the virtual source and the scattered surface waves at the second receiver, resulting in estimates of the scattered surface waves. Lastly, these scattered surface-wave estimates are adaptively subtracted from the real data. However, it is shown that for the retrieval of scattered surface waves, just a few points are stationary and thus sources are needed in the crossline direction. Further research to investigate the effects of different acquisition geometries and assess the method in regions with different near-surface scattering characteristics could broaden the applicability of the method to hard-rock environments, such as the cases presented in this thesis. Nevertheless, the application of interferometric surface-wave suppression for scattered surface waves has the potential to greatly improve the results for hard-rock environments, where (as shown in Chapter 3) the subsurface structures are very complex with strong lateral heterogeneities.

We also showed in Chapters 2 and 3 that the interferometric surface-wave suppression method requires the active sources to be located at, or nearby, a receiver location, so that the retrieved SI responses accurately estimate the surface-wave energy for each active-source gather. However, this condition is not always satisfied in the field. Super-virtual interferometry was derived from the SI method to retrieve shot-to-receiver signals by convolving the observed field traces with inter-receiver virtual traces (i.e., obtained by the SI) [3, 4]. This method has been applied for the enhancement of refraction

and diffraction arrivals. In addition, another method close to the previously mentioned one, but utilizing only the first step of super-virtual interferometry, was used to estimate the location of scatterers and heterogeneities in the subsurface [5–9]. An and Hu [10] proposed the use of super-virtual interferometry to estimate shot-to-receiver surface waves and subsequently use them for adaptive subtraction. In this way, the requirement that the active sources should collocate with one of the receivers is no longer needed.

OTHER TRANSFORMS AND INTERPOLATION ALGORITHMS

In Chapter 6, we proposed to utilise hyperbolic Radon transforms to filter the SI responses in the Radon domain to provide a more suitable result to supply missing traces in relatively large gaps. As previously mentioned, Radon transforms are not orthogonal transforms. Consequently, the transformed model and the true model are not identical. Therefore, the hyperbolic Radon transform is obtained most commonly by inversion methods and implies the loss of data. In particular, this can be problematic when using Radon transforms to represent highly noisy data, acquired in very complex geological settings. Apart from the high noise content, these data lack continuity and definition of hyperbolic events (e.g., as the data utilised in Chapters 2 and 3). Thus, it becomes difficult for the transform to properly represent the data. The utilisation of the proposed methodology with other transforms that can represent these data, such as curvelet or Ridgelet [11], could provide a suitable result for these cases.

In Chapter 5, we proposed to utilise SI responses to fill in relatively large gaps in order to help an interpolator (in our case, the POCS image restoration algorithm) to provide a better result. Nevertheless, many other interpolation methods are worth exploring that can benefit from the utilisation of SI to give suitable results for data reconstruction in relatively large gaps. Other interpolation methods could provide, for instance, less background noise than generated by the POCS algorithm. For example, Anti-leakage Fourier transform methods [12, 13] also perform well for small gaps or randomly missing traces. However, any Fourier-based interpolation method will fail in the case of a large data gap since some spatial frequency content required for the interpolation is missing. Data retrieved from SI can play a decisive role to solve this problem [14]. Moreover, the methodology proposed in Chapter 6 can be utilised as a step prior to preconditioning the SI responses, obtaining a better estimate of the missing data. This could also help the interpolation algorithm provide a superior result.

REFERENCES

- [1] D. Halliday and A. Curtis, *Seismic interferometry of scattered surface waves in attenuative media*, *Geophysical Journal International* **178**, 419 (2009).
- [2] D. F. Halliday, A. Curtis, P. Vermeer, C. Strobbia, A. Glushchenko, D.-J. van Manen, and J. O. Robertsson, *Interferometric ground-roll removal: Attenuation of scattered surface waves in single-sensor data*, *Geophysics* **75**, SA15 (2010).
- [3] W. Dai, T. Fei, Y. Luo, and G. T. Schuster, *Super-virtual interferometric diffractions as guide stars*, in *SEG Technical Program Expanded Abstracts 2011* (Society of Exploration Geophysicists, 2011).

- [4] I. Mallinson, P. Bharadwaj, G. Schuster, and H. Jakubowicz, *Enhanced refractor imaging by supervirtual interferometry*, *The Leading Edge* **30**, 546 (2011).
- [5] U. Harmankaya, A. Kaslilar, J. Thorbecke, K. Wapenaar, and D. Draganov, *Locating near-surface scatterers using non-physical scattered waves resulting from seismic interferometry*, *Journal of Applied Geophysics* **91**, 66 (2013).
- [6] A. Kaslilar, U. Harmankaya, K. Wapenaar, and D. Draganov, *Estimating the location of a tunnel using correlation and inversion of rayleigh wave scattering*, *Geophysical Research Letters* **40**, 6084 (2013).
- [7] A. Kaslilar, U. Harmankaya, K. van Wijk, K. Wapenaar, and D. Draganov, *Estimating location of scatterers using seismic interferometry of scattered rayleigh waves*, *Near Surface Geophysics* **12**, 721 (2014).
- [8] U. Harmankaya, A. Kaslilar, K. Wapenaar, and D. Draganov, *Locating scatterers while drilling using seismic noise due to tunnel boring machine*, *Journal of Applied Geophysics* **152**, 86 (2018).
- [9] J. Liu, D. Draganov, R. Ghose, and Q. Bourgeois, *Near-surface diffractor detection at archaeological sites based on an interferometric workflow*, *Geophysics* **86**, WA1 (2021).
- [10] S. An and T. Hu, *Suppression of seismic surface waves based on adaptive weighted super-virtual interferometry*, *Science China Earth Sciences* **59**, 2179 (2016).
- [11] R. X. Gao and R. Yan, *Beyond wavelets*, in *Wavelets* (Springer US, 2010) pp. 205–220.
- [12] S. Xu, Y. Zhang, D. Pham, and G. Lambaré, *Antileakage fourier transform for seismic data regularization*, *Geophysics* **70**, V87 (2005).
- [13] S. Xu, Y. Zhang, and G. Lambaré, *Antileakage fourier transform for seismic data regularization in higher dimensions*, *Geophysics* **75**, WB113 (2010).
- [14] B. Boullenger, *Controlled-source seismic reflection interferometry: Virtual-source retrieval, survey infill and identification of surface multiples*, *Ph.D. thesis*, Delft University of Technology (2017).

ACKNOWLEDGEMENTS

When I began this journey five years ago, I had a lot of new things to learn and adapt to. I would like to thank the support and contribution of numerous people that helped me navigate my PhD and overcome its many challenges. I am incredibly grateful to all those who have helped me along the way, and without their assistance, this work would not have been possible.

First, I would like to express my gratitude to my promotors, Dr. Ir. Deyan Draganov and Dr. Ranajit Ghose, for their continuous guidance and encouragement. Deyan, I remember our first meeting in the Havanna of Villa Urquiza. After seeing that how much you like alfajores, it was easy for me to instantly connect with you. I am incredibly grateful for the opportunity you gave me and for your constant support and mentorship. Your guidance has not only helped me to adapt to a new place and culture, but also to the academic world. I look forward to continuing our professional relationship and collaborating on future research endeavours (as well as movie nights). Ranajit, although we have not worked as closely together, I greatly appreciate your continuous feedback and encouragement. Your attention to detail and knowledge of data processing and writing have been inspiring and immensely valuable to me and this thesis.

My PhD was founded by the Smart Exploration project, which received funding from the European Commission Horizon 2020 (grant number 775971). The project provided me with invaluable experience and allowed me to meet a diverse group of researchers. I am grateful for the opportunity to have been part of such an exciting project and the people I met through it. I would like to express my thanks to Alireza, George, Valentina, and Stefan, thank you for your collaboration and for sharing your knowledge and experience. In particular, I want to thank Emilia for her help in the arduous processing of the data for Chapter 4. Her insights were instrumental in the success of this work, and I am grateful for being so welcoming and for her willingness to share her expertise. I also want to express my gratitude to project Young Professionals, Bláthnaid, Lena, Viveka, Emma, George, Paula, Bojan, Katerina, Simo, and Tatiana, for their contribution and the fun meetings. Finally, I would like to thank cabin 5, Myrto, Brij, Magdalena, and Federico, for making fieldwork so pleasant and musical, despite the challenges posed by the rain, the mud, and the cold.

I would not have taken the decision to pursue a PhD in TU Delft if it was not for the support and encouragement of Prof. Maria Laura Rosa (UNLP) and Prof. Gabriela Badi (UNLP). Lau, I am grateful for you trusting me and allowing me to do my Master thesis with you, and for introducing me to the research world. Gabi, thanks for kindly recommending me as a PhD candidate and for encouraging me to follow the decision of doing it. I would also like to express my gratitude to Prof. Mauricio Sacci (University of Alberta) and Prof. Danilo Velis (UNLP) for their collaboration and guidance, which helped shape and develop the ideas for the last chapter of this research.

During the last year of my PhD, I also had the opportunity to do an internship at Fugro to gain experience and work in the industry. Many thanks to Peter Loojen, Johannes

Singer and Myrna Staring for the opportunity and great times that particularly brighten the gloomy lockdown days. I am greatly enjoying and looking forward to continuing working with you.

I am grateful for the companionship and shared moments with colleagues and friends at TU Delft. First and foremost, I want to express my gratitude to Jianhuan. I am eternally grateful for all your help with coding, finding papers, ideas, and endless explanations that greatly helped this work. I also want to thank my desk mate, officemate, bouldering partner and great friend, Johno. Thanks for helping with the Dutch summary of this thesis, for making the PhD days fun, and the Christmas full of pepernoten. Thanks Billy, Maria, David and Hamed for the Latin nights that made me feel more at home. To Martha and Sixue, thanks for making sporting more bearable and fun. And thanks Diego for the wise (although late) advice not to bike down the stairs in the dunes.

I would also like to thank Joeri, Myrna, Karlien and Reuben for inviting me to be part of the DOGS board, it was definitely an enriching and enjoyable experience at TU Delft, that lasted almost throughout my entire PhD, with the later additions of Billy, Johno, and Aukje. Many thanks for the great moments!

I would like to extend my gratitude to the numerous supportive colleagues who I met along the way and have made a positive impact on my journey, including Amin, Andrea, Anne, Aydin, Boris, Camille, Dieter, Eddy, Emilio, Entela, Faezeh, Gil, Jan-Willem, Jingming, Karim, Lele, Lisanne, Matteo, Max, Menno, Milad, Musab, Nicolas, Quinten, Ranjani, Remi, Santosh, Shohei, Shotaro, Stephan, Tim, and the many others who I am probably forgetting. I would also like to express my gratitude to the non-academic staff of the department for their kindness and assistance from day one.

My survival away from home would not have been possible without Chris. Thanks for the countless mates, tortillas and arroz con leche. Thanks for being home away from home. Thanks to Vicky and Bel, who once again were an incredible help during thesis writing process, and made it more bearable. To my closest friends, Maru, Anto and Lara, thank you for your unwavering support in spite of being on the other side of the Atlantic. The late-night phone calls and virtual hugs helped me weather even the toughest moments.

My greatest gratitude goes to my family. Thanks to my grandmas Hildi and Mimi, to my godfather Fernando, to my cousins Emma, Pame, and Pablo, to my kind-hearted aunt Anita, and to my godson Lauti for the unconditional love. Finally, I want to thank my parents, Ruben and Claudia, and my sister Natalia. I owe everything I am and accomplish to you.

CURRICULUM VITÆ

Florencia Ibel BALESTRINI

13-01-1993 Born in Buenos Aires, Argentina.

EDUCATION

2007–2010 High-School
 Instituto Santa Lucia
 Majored in Economics & Bussines Management

2011–2017 Combined Bachelor's and Master's degree in Geophysics
 National University of La Plata (UNLP)

2018–2023 PhD. in Applied Geophysics
 Technological University of Delft (TU Delft)

LIST OF PUBLICATIONS

8. **F. Balestrini**, D. Draganov, M. Staring, J. Singer, J. Heijmans and P. Karamitopoulos, *Seismic Modelling for Monitoring of Historical Quay Walls and Detection of Failure Mechanisms*, in [NSG2021 2nd Conference on Geophysics for Infrastructure Planning, Monitoring and BIM](#) (European Association of Geoscientists & Engineers, 2020).
7. **F. Balestrini**, D. Draganov, D. Ngan-Tillard and F. Hansen, *Electromagnetic-Interferometric Direct-Wave Suppression for Detection of Shallow Buried Targets With GPR*, in [NSG2021 27th European Meeting of Environmental and Engineering Geophysics](#) (European Association of Geoscientists & Engineers, 2020).
6. **F. Balestrini**, D. Draganov, R. Ghose, E. Koivisto, A. Malehmir and M. Savolainen, *Surface-wave suppression through seismic interferometry: A case study at the Siilinjärvi phosphate mine in Finland*, in [SEG Technical Program Expanded Abstracts 2020](#) (Society of Exploration Geophysicists, 2020).
5. **F. Balestrini**, M. Sacchi, A. Malehmir, P. Marsden, R. Ghose and D. Draganov, *Data Reconstruction Using Seismic Interferometry Applied to Active-Source Data from the Ludvika Mines of Sweden*, in [NSG2020 3rd Conference on Geophysics for Mineral Exploration and Mining](#) (European Association of Geoscientists & Engineers, 2020).
4. **F. Balestrini**, D. Draganov, A. Malehmir, P. Marsden, and R. Ghose, *Improved target illumination at Ludvika mines of Sweden through seismic-interferometric surface-wave suppression*, [Geophysical Prospecting](#) **68**, 200 (2019).
3. **F. Balestrini**, D. Draganov, A. Malehmir and R. Ghose, *Seismic Interferometry for Surface-Wave Attenuation - A Case Study from the Ludvika Mines of Sweden*, in [25th European Meeting of Environmental and Engineering Geophysics](#) (European Association of Geoscientists & Engineers, 2019).
2. **F. Balestrini**, M.L. Rosa, *Seismic structure of the Río de La Plata craton from surface wave tomography*, [Seismological Research Letters](#) **89**, Number 2B, 717-966 (2018).
1. **F. Balestrini**, M.L. Rosa, *Surface-wave tomography in the Río de La Plata craton region*, in [XXVIII AAGG and IPSES 2017 Scientific Reunion \(La Plata, Argentina\)](#).

